Mechanical design, control and optimization of a hybrid solar microgrid for rural electrification and heat supply in sub-Saharan Africa

by

Queralt Altés Buch

Submitted to the Department of Aerospace and Mechanical Engineering in partial fulfillment of the requirements for the degree of

Master in Electromechanical Engineering

at the

UNIVERSITY OF LIEGE

August 2016

Pels meus avis.
Santi, l'excel·lència. Pili, la integritat.
August, l'enginy. Angelina, la dedicació.
Sense aquests valors no hagués estat possible.
Gràcies.

Abstract

This thesis aims at developing, optimizing and controling a hybrid solar microgrid for rural electrification and heat supply in sub-Saharan Africa. The considered system includes PV, Parabolic Trough Collectors, Organic Rankine Cycle and LPG generator, as well as chemical battery storage and thermal energy storage. The work focuses on multiple aspects of the ongoing development of solar hybrid microgrids for the rural electrification of remote areas in Lesotho. These aspects range from very specific improvements (the mechanical design of a high expansion ratio expander) to the more global evaluation of their impact once included into a complex micro-grid system. Special attention has also been paid to the links between thermal and electrical demands.

The main contributions of this thesis are:

- The mechanical design of a high expansion ratio scroll expander, involving drawing, machining and assembly of the parts.
- The detailed model of an organic Rankine cycle with the purpose of evaluating the improvement brought by the high expansion ratio scroll expander and mapping the ORC performance.
- A building model developed to predict the thermal loads of a health clinic in rural communities of Lesotho. The developed lumped-parameter model can be used for various building typologies and communities. The model is designed to be as generic and simple as possible, and contrasts with the data-intensive models generally proposed in the literature.
- The gathering of monitoring and weather data relative to a health clinic in Lesotho, and their use for the calibration of the building model.
- A microgrid model built by interconnecting all of its subcomponent models. A rule-based control strategy is developed, accounting for interactions between thermal and electrical loads, and dispatching heat and power flows of each component in order to cover the demand while minimizing the fuel consumption.
- A particle-swarm optimization model used to optimize the microgrid under different cost assumptions and control strategies

The above models prove that the system performs better with the developed high expansion ratio expander. The maximum output power of the ORC is increased by 33%, and the fuel consumption of the microgrid is reduced by 25%.

For the studied community of Ha Nkau in Lesotho, the determined optimal system infrastructure is composed of PV (65 kW) and batteries (259 kWh) only, and the optimum control strategy achieves a levelized cost of electricity of 0.202 USD/kWh. Fuel consumption is mainly due to the burner, which supplies all the thermal load because no other heating system is selected by the optimization.

Acknowledgements

I am very grateful to Pr. Vincent Lemort, who gave me the opportunity of doing my Master's Thesis in such a great engineering school as it is the Massachusetts Institute of Technology (MIT). I wish to thank him for his advises and interesting discussions. I wish to thank Robert Stoner, sub-director of the MIT Energy Initiative, for accepting me.

I cannot thank Dr. Matthew S. Orosz enough, director and founder of STG International, who made this work possible. I wish to thank him for his countless advises and permanent availability, which have been essential for this work. I am also grateful to all STG Team for providing me helpful data for the development of the work.

A special thanks goes to all the members of Parsons Laboratory (MIT), who warmly welcomed me and provided an excellent atmosphere. Thank you to all the people I encountered in Boston, who made me feel at home even from the other side of the pond. The last six months have been priceless at a personal level.

I wish to specially thank August Buch Sarsanach, technical director of Buch Maquinaria, for the interesting discussions about mechanics and machining.

I could not be more grateful to my family, whose unwavering support, even from the distance, made my stay successful. Last but not least, thank you to my partner in crime for his patience and for providing me a sounding board when things were difficult. Your support made me feel unshakable in front of any adversity.

Contents

Chapter 1

Introduction

1.1 Rural electrification

Energy is a key element accompanying the development of a country. According to International Energy Agency (IEA), 70% of the increase in the global primary energy consumption by 2030 is expected to come from developing nations. A large share of this future development is linked to the electricity demand: according to the World Energy Outlook 2015, 1.2 billion people currently lack access to electricity, mainly in rural areas of developing countries [1].

Electricity in rural areas is mostly used for lightning and television (80% of consumption), rarely used for cooking, and infrequently used for fans and irons [1]. Because health and education workers tend to stay in electrified communities, rural electrification (RE) creates a positive impact on service provision. Electricity access also has a positive impact on education (e.g. through lighting) or health (e.g. through refrigeration).

Some countries select communities to be connected to the grid on a *least cost* basis. This favors the communities close to the existing grid (i.e. next to roads or towns). For example, Peru Rural Electrification changed its social criteria to a least cost one [1]. In some other countries such as India, it is common that the grid passes near to a community without connecting it (so called "under grid" communities). Non electrified communities are thus more difficult to identify, since the infrastructure of the grid near to a community does not imply the latter is connected to it. Moreover, the Indian government stipulates that one community is considered as electrified when it has at least one connection to the grid, which does not imply that the electricity is being used by a large part of the community.

In most countries, governments prefer to increase grid coverage through extensive growth (i.e. extending the grid) rather than intensive growth (i.e. connecting the unconnected in already electrified villages) [1]. Most countries in Asia and South-America have already reached the grid extension limit and to increase the coverage, intensive growth is required. On the other hand, most of African countries still require substantial investment in generation, transmission and distribution. However, the high capital costs are difficult to recover due to the low density of population. Extensive growth is expected to be slower, leading to many remote regions which would benefit from distributed off-grid solutions.

Remote communities that may not be connected to the grid for several years can usefully be served by off-grid connections in the meantime. For sparse populations in remote or mountainous areas, distributed generation may be the only viable solution. Dramatic reduction in the price of Photovoltaic (PV) panels has promoted recent growth in off-grid electrification for these undeserved communities. It should however be noted that this market growth does not automatically imply poverty alleviation: the quality an impact of an off-grid or grid connection varies and social and economic factors in turn play an important role. Many small-scale off-grid electrification programs are designed to enable learning by doing, and in the last few years, together with technological advance and general cost reductions, off-grid solutions have become more accessible and cost effective. An important aspect of such decentralized generation lies in the fact that it is predisposed to renewable energy technologies deployment, which have clear environmental benefit (i.e. reduced CO_2 emissions).

In [2], guiding principles of the success conditions of decentralized rural electrification projects are presented, based on literature experience relative to a number of implemented projects. The resulting criteria-to-follow includes the following factors: participation of the beneficiaries, technology adoption, appropriate technology, cost, technology transfer and maintenance, decentralization, environmental impact, needs and demand, technology deployment and subsides. Although market deployment or subsidies schemes are subject to divergent opinions in the literature, there is general agreement about the most appropriate approaches [2].

It is hard to define the adequate business model for rural electrification, since it depends on the nature of each consumer. Institutions such as clinics and schools, who have a fairly stable demand because of their day-to-day similar activities, are well suited for Power Purchase Agreement (PPA) plans. The latter guarantees a certain amount of served load according to a monthly fee. However, household users may have a more variable demand, depending mostly on the other expenses they may have (school fees, pay cycles, holidays, etc.). The model Pay As You Go (PAYG) is generally more suitable in the contest of volatile financial circumstances [3].

Organizations such as STG International have as priority to benefit the entire community and not only the highest income population. Rural electrification and heat supply should therefore meet the following: improve health care through serving the local clinic, improve education through serving the local school, and improve individual's quality of life and income-generating capabilities through households connections. To power a community at affordable costs, it is necessary to understand how much power is needed and when. For a community of interest, the best system to cover these needs must then be determined. Although the latter depends on the former, it also relies on the local climate and weather, the geographic distribution of buildings and the proximity of the community to the national grid. Therefore, an evaluation of different generation technologies, the possible need of energy storage and the distribution system needs to be performed. Engineering cost-benefit analysis such as the one presented in [4] are a first step for systematic decentralized energy planning. The costs of connecting the community to the national grid and the possibility for this to happen should also be evaluated before taking decisions.

1.1.1 STG International

STG International [3] is a non-governmental organization based in Massachusetts whose aim is to provide technical, financial and intellectual support, assistance and training to projects and organizations focused on bringing sustainable energy technologies to communities all over the developing world.

Their vision is that local renewable energy sector is the most environmental-friendly way to cover the growth in energy demand. With it, positive feedback loops are then created because sustainable business, which is supported by energy demand, expands energy access and which in turn improves services at health clinics and schools.

To achieve this goal, STG pursues promising areas for research and development, builds strategic partnerships with other associations (e.g. governments, NGOs, private sector), serves communities in need and grows the technology sector in relevant markets. The mission is to support the entire project chain, from human resources through to implementation details, to ensure improved energy access for the world's citizens who need it the most.

The work presented in this thesis was performed in close collaboration with STG International and focuses on the microgrid technology developed by the organization. The specificities of this technology will be described later in this manuscript.

1.2 Microgrids for rural electrification

Isolated microgrids constitute an intermediate solution between grid extension and individual systems such as solar home systems or small gensets. They also present the capability (although rarely applied) to connect or disconnect from the main grid, which is a significant advantage in case of uncertainties about the future grid extensions.

One of the key challenges when designing microgrids is to determine the local electricity and thermal demands, which constrains the size of the system and its components and influences the control strategy. Demand data from monitoring campaigns in remote areas is generally unavailable. In the literature, various models are proposed to remedy to this lack of data and generate realistic load profiles, however most of them are relatively data-intensive (see for example [5]).

Most microgrid models are optimization models with perfect foresight. They often optimize at the same time both the dispatch of the energy and the sizing of the different components within the microgrid. A very common software for that purpose is HOMER [6]. Other examples of such models from the scientific literature can be found in [7] and [8]. However, in practice the systems are often operated and in a myopic manner (contrary to the perfect foresight): the controller does not have any (or a partial) knowledge about the future demand and generation patterns or expectations of the same may prove inaccurate. In this work, the optimization model is based on a realistic rule-based control, which may be less optimal than the former but accounts for the inefficiencies encountered in real systems. It is also designed in such a way to cover the demand at all times.

Moreover, most of the micro-grid related literature focus on electrical power only. Few models present interaction with thermal demand in terms of heat or cooling loads. These aspects are however key issues in some regions: for example, wood or dung stoves used for space heating and cooking in many remote areas have negative effects such as deforestation or poor air quality leading to health problems. Linking thermal and electrical loads can be beneficial and increase the overall energy efficiency of the system: combined heat and power systems can for example provide both loads simultaneously with a much higher efficiency than in the case of separate generation. Also, heat storage can be performed in a much more cost-effective way than electricity storage, which is particularly beneficial for isolated systems.

1.3 The Organic Rankine Cycle technology

In addition to using commercially available PV, battery and generator technologies, STG International has developed a locally manufacturable combined heat and power technology whose heat source is provided by a concentrating solar power (CSP) plant. The CSP is composed of parabolic troughs and the power block is an Organic Rankine Cycle (ORC) unit.

Historically, ORCs were first developed in solar applications (e.g. for irrigation, desalination, hot and cold generation, etc.). They have been successfully used in other applications such as geothermal, waste heat recovery (WHR) and with biomass [9]. At present, ORC technology has reached economic maturity in these fields, but there are still very few commercial solar ORC systems, the majority being prototypes developed for laboratory testing.

According to [10], the ORC is a suitable technology for power generation from the low to medium power scale (up to some MWe). This is influenced by a diversity of factors, among which are the higher density of organic fluids (which imply smaller components sizes), the lack of super-heaters as a consequence of a dry expansion, a lower evaporating pressure and simpler boiler architecture. The lower boiling point of organic fluids also accommodates lower heat source temperatures. Therefore, because of its ability to recover low-grade heat, the ORC has proved to be suitable for power sources such as medium-temperature micro-concentrating solar power (μ-CSP) [4].

Unlike conventional power cycles, its simplicity and the possibility to manufacture the components locally makes the ORC well adapted to decentralized power generation [10]. The ORC characteristics allow using off-the-shelf components from the HVAC industry. Moreover, the possibility of storage leads to a good dispatchability [9]. These advantages make the ORC better adapted than steam cycles to the conversion of low-capacity solar power [10] that is distributed and economically harvested at relatively lower temperatures, compared to fossil fuels.

The key component of an ORC unit is its expansion machine. Positive displacement machines are preferably used over turbomachinery for small-scale applications [10]. A literature review shows that the most common volumetric machines are the screw expander for up to some hundreds kWe, and the scroll expander or the piston expander for smaller-scale applications. Currently the majority of scroll expanders are obtained by modifying

existing compressors. Although these machines are demonstrated to perform with good efficiencies when working as expanders (e.g. in [11] and [12]), their expansion ratio may remain limited for some applications. This limitation generates significant losses in solar ORC systems whose heat source temperature is relatively high compared with geothermal or low temperature WHR. A large part of this thesis will therefore focus on the scroll expansion machine and on possible improvements.

1.4 Scope of this thesis

This thesis aims at developing, optimizing and controlling a hybrid solar microgrid for rural electrification and heat supply in sub-Saharan Africa. The considered system includes PV, Parabolic Trough Collectors (CSP), ORC and Liquefied Petroleum Gas (LPG) generation, as well as chemical battery storage and thermal energy storage (TES).

The first challenge of this thesis is to improve the efficiency of a small-scale solar ORC unit by increasing the expansion ratio of its scroll expander. A new mechanical design of a scroll expander is developed to accommodate the high expansion ratio scroll geometry developed in [13]. The proposed architecture is manufactured and assembled in the scope of this work. The main goal is to install the new expander to the micro-CSP ORC prototype power plant in Florida, developed by STG International.

A detailed model of an ORC is also developed with the purpose of evaluating the improvement potential of a well-designed high expansion ratio scroll expander compared to a low ratio scroll expander adapted from a scroll compressor.

As previously stated, the load profiles are essential inputs for designing off-grid systems. The second main scope of this thesis is thus to develop a simplified building model to predict thermal loads of a health clinic typical of rural communities in Lesotho. The main idea is to create a single model with very few inputs that can be used for various building typologies and communities. Several monitoring campaigns performed in rural health centers are used as input to calibrate the model.

Starting from the model of the improved ORC and the heating and electricity demand profiles, a microgrid model is built by interconnecting all of its subcomponent models. A rule-based control strategy is then proposed to dispatch the heat and power flows of each component in order to cover the demand while minimizing the fuel consumption. Since not only electricity but also heat are supplied, the interactions between thermal end electrical loads are modeled.

Finally, the microgrid model is wrapped into a non-linear optimization aiming at determining the system infrastructure and the optimum control strategy that achieves the minimum tariff (USD/kWh) for the final consumers.

Chapter 2

Model and performance evaluation of a solar ORC

The micro-grid model presented in Chapter 5 is intended to supply both electrical and thermal loads to a community. Concentrating Solar Power (CSP) technologies are suitable for this purpose: they are a low-cost technology with a low environmental footprint. They also offer the possibility to fulfil both electrical and thermal loads simultaneously. On the contrary, PV or diesel generators are not well suited to meeting thermal demand (e.g. hot water or heating) at a reasonable cost.

Availability and dispatchability of production are also important assets of CSP systems. Load following Diesel or LPG generators meet this requirement but their efficiency drops steeply for partial loads and they have high CO_2 emission and fuel costs. Because CSP systems collect solar energy as heat, they can provide a large capacity of storage (thermal storage can be up to 10 times more cost-effective than traditional batteries), which enables modulation of the generation with respect to the load curve throughout the day.

In order to simulate the dispatch of both the thermal and electrical loads, the micro-grid model requires accurate predictive models of all its sub-components. A detailed model of an ORC has thus been developed to evaluate the performance of the cycle in different operating conditions.

Because a significant part of this thesis has been dedicated to the improvement of the ORC expansion machine (as detailed in Chapter 3), two models have been developed. The first one with the current single-stage expansion performed by a modified scroll compressor of a volumetric ratio of 2.8. The second one with the high expansion ratio scroll expander designed by STG International described in section 2.2.2.

It is finally worthwhile to note that this chapter focuses on the ORC model only, the models of the other sub-components (parabolic troughs, thermal storage, PV) are detailed in Chapter 5.

2.1 Current Solar-ORC from STG International

In 2007, STG set out to develop a small-scale solar distributed CSP co-generation platform that uses medium temperature collectors and an ORC to produce electricity and thermal

energy demands for clinics and schools in a renewable and affordable way [14]. The working principle is shown in Figure 2.1. The generated electric power is used to charge a battery bank (whose voltage is 48V) that supplies the load using a DC-AC inverter.

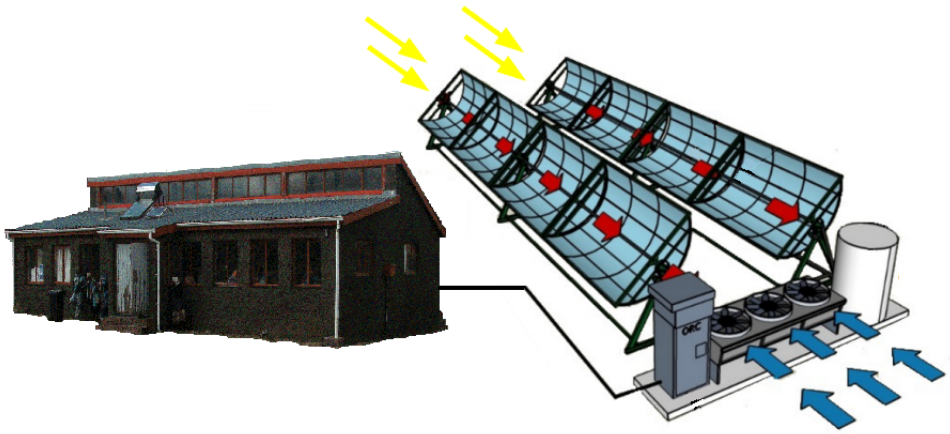

Figure 2.1: Principle of STG's micro-CSP co-generation plant [3]

The goal is a microgenerator design that can be manufactured and assembled almost anywhere, to provide rural areas of developing countries with a system that can be constructed locally (unlike PV cells). The system aims at replacing or at least supplementing Diesel or LPG generators in off-grid areas, by generating clean power at a lower levelized cost [15].

2.1.1 CSP

The collector field (Figure 2.2) is a single-axis parabolic trough with micro-aluminum reflective sheeting and a Heat Collection Element (HCE). The latter has selective coating and air (or optionally vacuum) -filled annulus between absorber pipe and glazing.

The Heat Transfer Fluid (HTF) is Monoethylene glycol (MEG) and has thermal buffering in a thermal storage tank with a 2 m^3 packed bed of 19 mm quartzite [14]. Thermal energy storage dampens the variability of solar irradiation, provides a stable thermal source to the vaporizer, and also extends operation beyond daylight hours for a period of time.

2.1.2 ORC

STG's ORC uses R245fa with a one-stage expansion, commercial HVAC tubes-and-fins air condenser and brazed plate heat exchangers for high pressure heat transfer [14]. The use of widely available industrial components such as steel parts, plumbing supplies and HVAC equipment is due to the fact that commercial CSP technologies are generally only available at MW scale power plants, whereas mini grids may require kW scale capacities.

The ORC system includes the main components of a Rankine cycle i.e. an evaporator, an expander, a condenser and a recirculation pump, but also a heat exchanger that provides recuperation from the superheated exhaust to the subcooled liquid, interposed

Figure 2.2: STG's parabolic trough collectors, installed in Lesotho [3]

between the expander exhaust and the pump outlet.

The system power output is 3-5kWe [14], and currently does not accommodate thermal demand. A conceptual scheme of the current ORC configuration is shown in Figure 2.3.

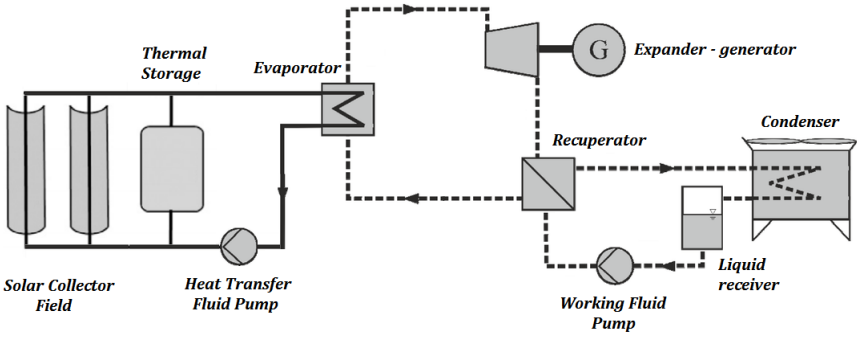

Figure 2.3: Conceptual scheme of current ORC configuration

2.1.3 Expander design

The expansion process is currently performed by a modified HVAC scroll compressor machine adapted to run as an expander, with an internal volume ratio of 2.8. Although these machines are proven to operate efficiently as expanders, they are optimized for the compressor mode, and their performance tends to degrade when used in an ORC. This can be due, e.g. to the higher expansion ratios, or to an oversized electrical generator. Expansion machines are therefore one of the key components presenting a high potential for improvement in small-scale ORC systems.

2.2 Proposed improvements

2.2.1 ORC configuration

In order to produce hot water for both sanitary needs and heating, the possibility of cogeneration is offered by installing a condenser that works with water as a secondary fluid in addition to the current air-flow condenser. Several cycle configurations are possible for

that purpose. The one selected in this work is shown in Figure 2.4.

In this setup, the working fluid flow is regulated by a 3-way valve, leading to two fluid circuits possibilities:

- When there is thermal demand, the working fluid is sent to the water condenser. Hot water exiting the condenser is used to produce hot water. Although the heating capacity of a 3-5kWe ORC may not seem sufficient, it must be noted that the condenser thermal power is about an order of magnitude higher than the electrical, and that thermal loads are limited in such microgrids (e.g. to a clinic and a school).
- If there is no heating demand, the water flow rate is zero and there is no heat exchange. Thus, the working fluid is sent to the tubes-and-fins air condenser.

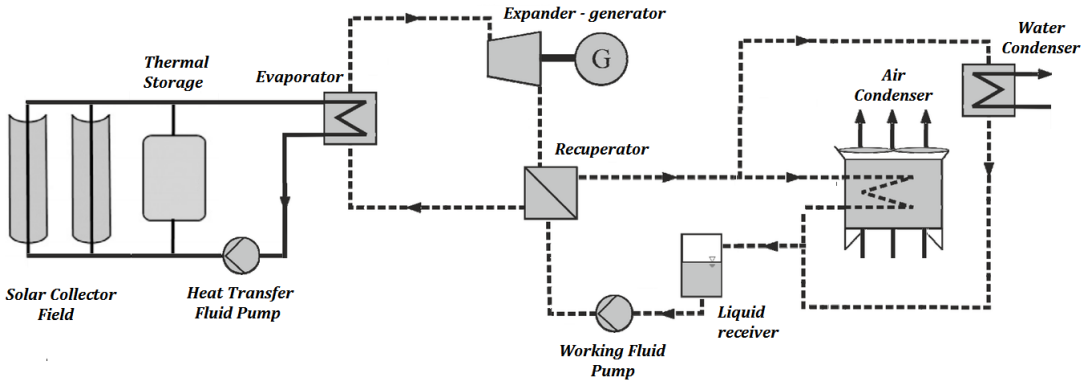

Figure 2.4: Conceptual scheme of the proposed ORC configuration

2.2.2 Expander design

The proposed new design developed by STG, in partnership with MIT and the Indian Institute of Science (IISc) with funding from the SERIIUS CSP-4 research program, consists of a non-constant wall thickness scroll expander [13]. The main goal is to use it in cycles that require a high expansion ratio, e.g. Rankine cycles, where adapted compressors are insufficient. A high expansion ratio expander is thus an alternative to the two-stage expansions proposed in some previous works [14] [16].

In the proposed expander, the chambers do not just increase in volume because of spiral characteristics but also because wall thickness is decreasing at the same time. Expander performances are thus improved. Expander characteristics are a high volumetric ratio of 4.89 and a swept volume of 17.04 cm^3.

The machine also includes a lubrication system to reduce mechanical friction and maximize performances. The latter has been developed in the scope of this thesis and is described in section 3.3.2. The new expander is thus hermetic in order to keep all fluids in a shell.

The new design is a hermetic, axially and radially compliant lubricated scroll expander with Oldham coupling, crank shaft power take off, and rotary mechanical power transferred

through a magnetic coupling. Intermediate pressure from the back pressure chamber is regulated. A more detailed description of the improvements proposed for the expander is provided in Chapter 3.

2.3 Modeling

The proposed model of the ORC system is developed in the EES environment. The goal is not to model an existing system, but to propose a generic model for different ORC sizes and architectures. The developed model should be usable for two purposes:

- Sizing of the system: since the geometry of the system is not pre-defined, it is important to compute the size of each component to reach pre-defined performance indicators (pinch points, pressure drops, flow rate, etc.). Such a model is referred to as sizing or design model.
- Part-load simulation of a given system. Once sized, it is also useful to evaluate the off-design performance of the system, e.g. if the heat source/sink temperature vary or if the available power decreases. This kind of model is referred to as a simulation model in this thesis. It imposes the geometrical characteristics of the system and computes the performance indicators under variable boundary conditions.

Because of the acausal formulation of the models in EES, they can be used interchangeably as sizing or simulation models. The equations presented in the following section therefore refer to both types of models. The main difference originates from the imposed and recalculated values, which are provided in Table 2.1 at the end of the section.

2.3.1 Evaporator

The evaporator is a plate heat exchanger in which the working fluid is evaporated by the thermal oil from the collectors. It operates at a relatively high pressure (the critical pressure of R245fa is 3651 kPa).

In the case of a sizing model, the evaporator is sized to obtain the desired pinch point and pressure drop. Mass and energy balances are applied according to the following equations:

$$\dot{Q}_{ev} = \dot{M} \cdot (h_{ex,ev} - h_{su,ev}) \tag{2.1}$$

$$\dot{Q}_{ev} = \dot{M}_{sf,ev} \cdot cp_{sf,ev} \cdot (T_{su,sf,ev} - T_{ex,sf,ev}) \tag{2.2}$$

$$pinch_{ev} = min\,(T_{ex,sf,ev} - T_{su,ev} \quad ; \quad T_{ex,tp,sf,ev} - T_{ev} \quad ; \quad T_{su,sf,ev} - T_{ex,ev}) \tag{2.3}$$

As shown in Figure 2.5, a large sub-cooled zone exists at the inlet of the evaporator. A 3-zones HX model is thus needed to accurately compute heat exchange area.

The area of each phase zone (i.e. liquid, two-phase and vapor) is computed from fluid heat transfer coefficients and overall heat transfer coefficients, as shown in equations 2.4 to 2.6. Fluid heat transfer coefficients and pressure drops at each phase are computed by correlations suited for plate heat exchangers. Thonon [17] and Hsieh [18] correlations have been used for single and two-phase heat transfer, respectively.

$$AU_z = \frac{\dot{M} \cdot \Delta h_z}{\Delta T_{log,z}} \tag{2.4}$$

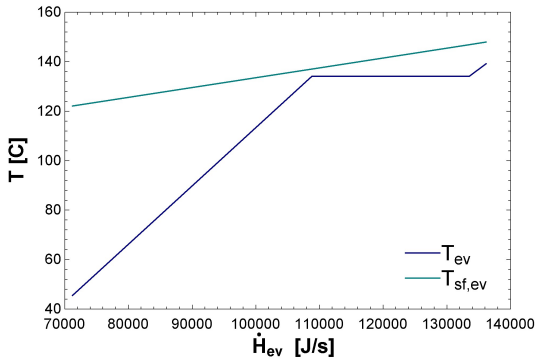

Figure 2.5: Temperature profiles in the evaporator

$$A_z = AU_z \cdot \left(\frac{1}{h_z} + \frac{1}{h_{sf,cd}} \right) \tag{2.5}$$

$$A_{ev} = \sum A_z \tag{2.6}$$

for zones $z = l, v, tp$.

In equation 2.4, the Logarithmic Mean Temperature Difference (LMTD) method is used. However, when simulating for varying working conditions, some temperature profiles can cross each other for a small period of time, which impedes the use of this method.

The method RLMTD (i.e. Robust LMTD), developed in [19] [20], has been used instead. This method (equation 2.7) avoids numerical failures and thus ensures smoothness for both steady-state and dynamic simulation. It rewrites the heat transfer model using only causal equations. The idea is not to leave the iterative process to the solver in order to avoid logarithms of negative numbers. Thus, it allows conditional statement and brings a solution if negative pinch points appear during the iterations. RLMTD value for negative pinches is as small as possible so that the leakage heat flow can be neglected. Parameters ξ and ε play a key role at this point:

- ξ influences how fast LMTD goes to zero. Small values lead to higher LMTD values at $\Delta T = 0$, and thus to higher leakage heat flow. On the other hand, high values entail steep variations of the RLMTD function, which can also lead to simulation failures.

- ε is the threshold (in terms of ΔT value) below which the LMTD function is replaced by a decreasing polynomial function. It should therefore be set to a lower value than the nominal pinch points of the modeled heat exchangers in order to ensure the validity of the LMTD method in usual operating conditions. As for ξ, it should however not be too small to avoid slow and non-robust simulation.

$$\Delta T_{\text{RLMTD}} = \begin{cases} \frac{T_1 - \Delta T_2}{\ln(\Delta T_1) - ln(\Delta T_2)} & if\ \Delta T_1 > \varepsilon, \Delta T_2 > \varepsilon\ and\ \Delta T_1 \neq \Delta T_2 \\ \frac{\Delta T_1 + \Delta T_2}{2} & if\ \Delta T_1 > \varepsilon, \Delta T_2 > \varepsilon\ and\ \Delta T_1 = \Delta T_2 \\ \frac{\Delta T_1 - \varepsilon}{\ln\left(\frac{\Delta T_1}{\varepsilon}\right)(1-\xi(\Delta T_2 - \varepsilon))} & if\ \Delta T_1 > \varepsilon\ and\ \Delta T_2 < \varepsilon \\ \frac{\Delta T_2 - \varepsilon}{\ln\left(\frac{\Delta T_2}{\varepsilon}\right)(1-\xi(\Delta T_1 - \varepsilon))} & if\ \Delta T_1 < \varepsilon\ and\ \Delta T_2 > \varepsilon \\ \frac{\varepsilon}{(1-\xi(\Delta T_1 - \varepsilon))(1-\xi(\Delta T_2 - \varepsilon))} & if\ \Delta T_1 < \varepsilon\ and\ \Delta T_2 < \varepsilon \end{cases} \tag{2.7}$$

Previous works [14] on low capacity ORCs allow the determination of characteristic nominal conditions for the evaporator (Table 2.1). Because a high molecular wight working fluid is used, the super-heating should be maintained as low as possible, according to [21]. Because no collector model has been implemented, the HTF nominal conditions are set to the values proposed in [14].

2.3.2 Air condenser

When there is no thermal demand, the ORC uses an air-flow tube-fin condenser to condense the working fluid. It comprises three fans with variable speed control whose power consumption is non negligible.

The condensed working fluid is contained in a liquid receiver at the outlet of the condenser, from which the fluid is re-pressurized in a piston pump.

As shown in the cross-sectional view in Figure 2.6, the working fluid in the condenser passes through twelve tubes arranged in five rows [22]. The tubes equipped with fins are perpendicular to the air flow. The fluid enters as a vapor and moves back and forward through the tubes in a two-phase state leaving at the end as a liquid.

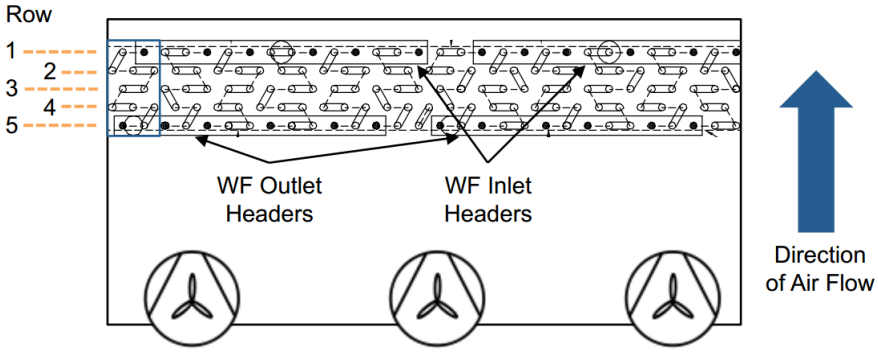

Figure 2.6: Cross-section of the condenser [23]

Cross-flow heat exchangers can be modeled as a counter-flow heat exchanger when more than four layers of tubes exist. The model is thus based on a counter-flow heat exchanger, the cross-flow component being neglected. Mass and energy balances are applied according to the following equations:

$$\dot{Q}_{cd} = \dot{M} \cdot (h_{su,cd} - h_{ex,cd}) \tag{2.8}$$

$$\dot{Q}_{cd} = \dot{M}_{sf,cd} \cdot (h_{ex,sf,cd} - h_{su,sf,cd}) \tag{2.9}$$

$$pinch_{cd} = min\left(T_{ex,cd} - T_{su,sf,cd} \quad ; \quad T_{cd} - T_{ex,tp,sf,cd} \quad ; \quad T_{su,cd} - T_{ex,sf,cd}\right) \tag{2.10}$$

As for the evaporator model and in the case of a sizing model, the condenser is sized to obtain the desired pinch point and pressure drop. The nominal conditions are in Table 2.1.

Similarly to the evaporator model, in order to size the condenser accurately, a 3-zones heat exchanger model is developed. The heat exchange area is function of the heat exchanger fluid nominal conditions, as expressed in equations 2.4 to 2.6. The fluid heat transfer coefficients at each phase (i.e. liquid, two-phase and vapor) are considered constant and taken from the condenser model studied in [23]. The fan consumption is assumed to be constant as soon as the air condenser is active.

2.3.3 Water condenser

The water condenser is only used when there is thermal demand (produced by the condensation of the working fluid). This heat is assumed to cover the need of a clinic and a school also connected to the micro-grid.

This condenser consists of a counter-current plate heat exchanger. Mass and energy balances are the same for the air condenser, and can be found in equations 2.8 to 2.9. Equation 2.10 defines the pinch point.

The condenser has been sized to obtain the desired pinch point. Nominal conditions are presented in Table 2.1.

2.3.4 Recuperator

Recuperation occurs from the superheated exhaust to the subcooled liquid. It is achieved through a plate heat exchanger installed between the expander exhaust and the pump outlet.

The high and low pressure sides are at the evaporation and condensing pressure, respectively. The former contains the subcooled liquid that comes from the condenser recirculated by the pump. The latter contains the superheated fluid that comes out of the expander, or the co-generation heat exchanger if used.

Mass and energy balances are the following:

$$\dot{Q}_{rec} = \dot{M} \cdot (h_{su,sh} - h_{su,cd}) \tag{2.11}$$

$$\dot{Q}_{rec} = \dot{M} \cdot (h_{su,ev} - h_{su,sc}) \tag{2.12}$$

$$\dot{Q}_{rec} = \dot{C}_{min,rec} \cdot (T_{su,sh} - T_{su,sc}) \tag{2.13}$$

where sub-indices su, sh and su, sc refer the superheated and subcooled inlet fluid conditions. $\dot{C}_{min,rec}$ is the minimum heat capacity flow rate, which always corresponds to the vapor side. The nominal conditions are defined in Table 2.1.

2.3.5 Expander

A scroll expander is a positive displacement machine whose losses are mainly linked to the internal volume ratio, the internal leakage, the friction and the pressure drops. The

internal volume ratio is defined by the relation between the volume at the moment the admission chamber is closed and the outlet volume at the opening of the last chamber.

In a scroll expander, the internal work of the expansion can be modeled as an isentropic expansion followed by a discharge. The former is defined by the internal volumetric ratio characteristic of the expander. The discharge, can be modeled by a constant volume expansion, which is the one generating irreversibilities. These irreversibilities are referred to as under and over-expansion losses. The equations to model the discharge are developed in [24], showing that the associated work is equal to the pressure between the last chamber and the outlet times the internal volume.

$$w_{in} = w_{in,s} + w_{in,v} = h_{su,exp} - h_{in,exp} + v_{in,exp} \cdot (P_{in,exp} - P_{ex,exp}) \tag{2.14}$$

In this all other losses (besides the under and over-expansion losses) are lumped into one single electromechanical conversion efficiency. The latter is set to $\varepsilon_{em} = 0.71$ based on the results obtained in [11].

$$w_{el} = h_{su,exp} - h_{ex,exp} = w_{in} \cdot \eta_{em} \tag{2.15}$$

Characteristics of the expander are presented in Table 2.1. The global isentropic efficiency of the scroll is finally computed according to the following:

$$\varepsilon_{s,exp} = \frac{w_{el}}{h_{su,exp} - h_{ex,s,exp}} \tag{2.16}$$

2.3.6 Pumps

Two circulation pumps are accounted for in the model: the working fluid pump and the heat transfer fluid pump. Pump efficiency is set to a constant, realistic value according to [25]. The pump consumption is computed as according to the following equations:

$$\dot{W}_{pp} = \dot{M} \cdot (h_{ex,pp} - h_{su,pp}) \tag{2.17}$$

$$\dot{W}_{htf,pp} = \frac{\dot{M}_{htf} \cdot (\Delta P_{htf,col} + \Delta P_{htf,ev})}{\rho_{su,col} \cdot \varepsilon_{pp}} \tag{2.18}$$

2.3.7 Off-design simulation

Once all components have been sized, the cycle can be simulated out of the nominal point under a wide range of working conditions. The goal is to establish a cycle performance map, which will further be integrated into the micro-grid model. Integrating the ORC model directly inside the micro-grid model and simulating it for each time step of a year would be processor intensive, and the computational efficiency of the micro-grid model would decrease. A cleaner, so-called "model reduction" option is to express the cycle performance with correlations that are a function of the relevant variables.

A first relevant variable affecting the efficiency of the ORC is the temperature of the heat transfer fluid coming from solar collectors. This can also be the temperature from TES, if it is supplying the ORC thermal demand. This temperature directly impacts the working fluid evaporation temperature and thus the working fluid pressure, temperature

Table 2.1: Inputs and parameters values for each sizing and simulation models

	Inputs/Parameters	Sizing	Simulation	
Evaporator	$pinch_{ev}$	4	-	K
	ΔP_{ev}	7500	-	Pa
	$\Delta T_{ex,ev}$	5	5	K
	b	0.002	0.002	m
	L_w	0.21	0.21	m
	L_h	0.50	0.50	m
	ϕ	1.2	1.2	-
	β	45	45	º
	$A_{tot,ev}$	-	2.063	m^2
HTF	$\dot{M}_{htf}$	0.85	0.85	kg/s
	$\Delta P_{htf,col}$	2435	2435	Pa
	cp_{htf}	2948	2435	J/kgK
	$\Delta P_{htf,ev}$	4137	-	Pa
	$T_{htf,su,ev}$	150	150	ºC
Condenser	$pinch_{cd}$	4	-	K
	ΔP_{cd}	4025	-	Pa
	$\Delta T_{ex,cd}$	5	5	K
	h_v	315	315	W/m^2K
	h_l	286.5	286.5	W/m^2K
	h_tp	1668	1668	W/m^2K
	h_cf	914.75	914.75	W/m^2K
	$\dot{W}_{fan}$	335	335	W
	$A_{tot,cd}$	-	5.87	m^2
Ambient air	ΔT_{cf}	12	12	K
	T_{amb}	18	18	ºC
Water from network	ΔT_{cf}	20	-	K
	$\dot{M}_{cf}$	-	0.744	
	$T_{w,return}$	50	50	ºC
	P_{water}	$2{\cdot}10^5$	$2{\cdot}10^5$	Pa
Recuperator	ε_{rec}	80	80	%
	$\Delta P_{vap,rec}$	7500	-	Pa
	$\Delta P_{liq,rec}$	5200	-	Pa
Expander	N_{rot}	3000	3000	rpm
	$r_{v,in}$	4.89	4.89	-
	V_s	$17.04{\cdot}10^{-6}$	$17.04{\cdot}10^{-6}$	m^3
	ε_{em}	71	71	%
Pumps	ε_{pp}	70	70	%

Table 2.2: Off-design simulation temperature ranges

	Range (ºC)
$T_{hf,su,ev}$	[130,159]
T_{amb}	[-5,30]
$T_{w,return}$	[25,50]

and density.

Another important variable is the one affecting the condensing temperature of the working fluid. That is ambient temperature for the air-flow condenser or return temperature from a hot water network for the water-flow condenser. In order to simulate the cycle, outdoor conditions have been varied through a wide range of realistic operating conditions, as shown in Table 2.2.

The efficiency of the cycle as well as second law efficiency are considered as relevant performance indicators. They are computed according to equations 2.19 and 2.20, respectively. Carnot efficiency used in second law efficiency is computed by equation 2.21, where temperature must be expressed in Kelvin.

$$\eta_{ORC} = \frac{\dot{W}_{net}}{\dot{Q}_{ev}} \tag{2.19}$$

$$\eta_{II} = \frac{\eta_{ORC}}{\eta_{Carnot}} \tag{2.20}$$

$$\eta_{carnot} = 1 - \frac{T_{cf,su,cd}}{T_{hf,su,ev}} \tag{2.21}$$

In equation 2.19, $\dot{Q}_{ev}$ is the heat power input in the evaporator and $\dot{W}_{net}$ is the total net electrical power, computed in equation 2.22. Sub-indices *exp*, *pp*, *pp,htf* and *fan,cd* refer to the expander, working fluid pump, heat transfer fluid recirculating pump and condenser fans.

$$\dot{W}_{net} = \dot{W}_{exp} - \dot{W}_{pp} - \dot{W}_{fan,cd} - \dot{W}_{pp,htf} \tag{2.22}$$

2.4 Results

As previously explained, the ORC performance has been evaluated as a function of two driving variables: hot and cold secondary fluid temperatures at the evaporator and condenser. Although the hot fluid is always the heat transfer fluid, the cold fluid can be either air or water depending on which condenser is being used. Results have thus been evaluated for both cases.

Moreover, the improvement of the performance of the ORC by using a high expansion ratio expander has also been studied. Expansion characteristics used in the model are chosen from the current and the new scroll expander, as described in sections 2.1.3 and 2.2.2.

2.4.1 Comparison of ORC performances using low or high expansion ratio expander

Figure 2.7 illustrates that the selected variables have a great influence on ORC efficiency. As expected, the lower the ambient temperature, the lower the condensing temperature and the higher the cycle efficiency. Similarly, the higher HTF temperature, the higher evaporating temperature. However, the cycle efficiency is not monotonically increasing with this temperature and reaches a maximum for a certain HTF temperature. This phenomenon is explained by the fact that as the HTF temperature approaches the fluid critical temperature both the working fluid pressure and the vapor density increase dramatically, which incrases the mass flow rate in the cycle. With a high pressure and a high mass flow rate, the pinch points in the heat exchangers and the under-expansion losses increase significantly, up to the point where they start decreasing the cycle efficiency. The output power, however, keeps increasing.

The ORC using the new high expansion ratio scroll expander presents a maximum cycle efficiency of 10.55%. However, a much smaller value of 7.96% is obtained for a lower expansion ratio scroll expander. This represents a decrease in cycle efficiency of 24.55%, which is significant.

Lowest efficiencies are encountered during the warmest months, where ambient temperature can reach 30°C. Values of 8.83% and 6.80% are obtained for an ORC working with high and low expansion ratio expanders respectively.

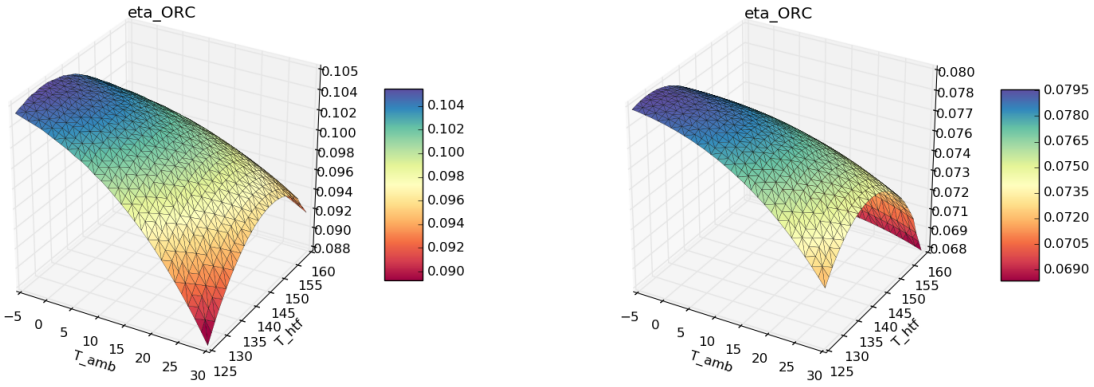

(a) Expander $r_v = 4.9$

(b) Expander $r_v = 2.8$

Figure 2.7: Comparison of ORC efficiency using air-flow condenser and with previous (a) and new (b) scroll expander

The second law efficiency, shown in Figure 2.8, has also been evaluated. Higher values are obtained when a high expansion ratio scroll expander is used. However, above a characteristic point the increase becomes marginal as the heat source temperature increases, which highlights the effects of an increased flow rate and increased under-expansion losses.

The electrical output is plotted in Figure 2.9. Results show that HTF temperature has a higher influence on electrical output than ambient temperature. This is mainly because

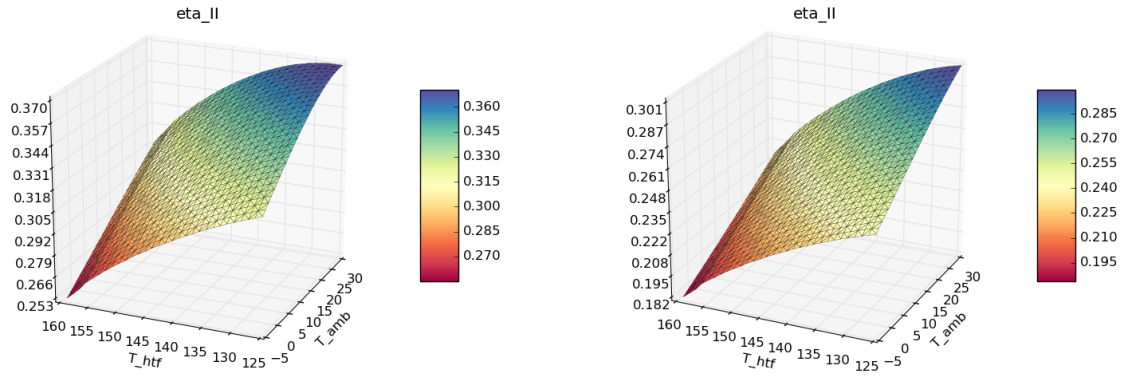

(a) Expander $r_v = 4.9$ (b) Expander $r_v = 2.8$

Figure 2.8: Comparison of Second Law efficiency using air-flow condenser and with previous (a) and new (b) scroll expander

the increased mass flow rate due to increasing HTF temperature influences the electrical output. The decrease in ambient temperature however has the main effect of increasing the cycle efficiency, which positively influences electrical output in a less pronounced way. Under favorable conditions, the projected output power from the high expansion ratio scroll expander is 4.6kW, whereas it is only 3.2kW for the low-ratio one. The latter therefore produces 30% less electrical power.

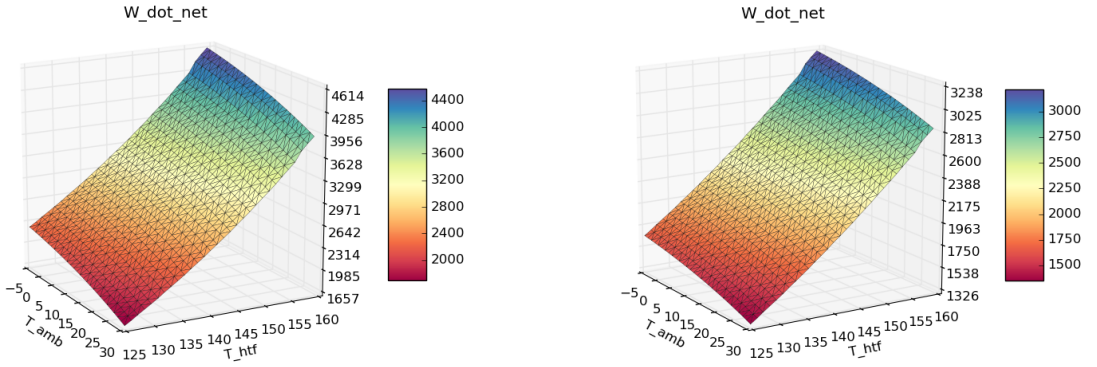

(a) Expander $r_v = 4.9$ (b) Expander $r_v = 2.8$

Figure 2.9: Comparison of ORC net output electrical power using air-flow condenser and with previous (a) and new (b) scroll expander

2.4.2 Comparison of ORC performances using air- or water-flow condenser

Since the ORC uses both air- and water-flow condensers depending on the thermal demand, a performance study for both cases has been performed. When comparing both condensers, the temperature range of use must be taken into account. Ambient air in Lesotho can widely vary from -5^{o}C to 35^{o}C during a year. However, the return temperature of a hot water network is almost constant during the year. Typically it varies between 25^{o}C and 55^{o}C depending on the desired hot water temperature.

The maximum ORC efficiency is 10.55% and is obtained with the air-flow condenser. The ORC with a water-flow condenser has a lower minimum efficiency, since water is used up to 55^{o}C while the air temperature is only occasionally above 30^{o}C. The cycle efficiencies for the nominal operating conditions are compared in Figure 2.10a.

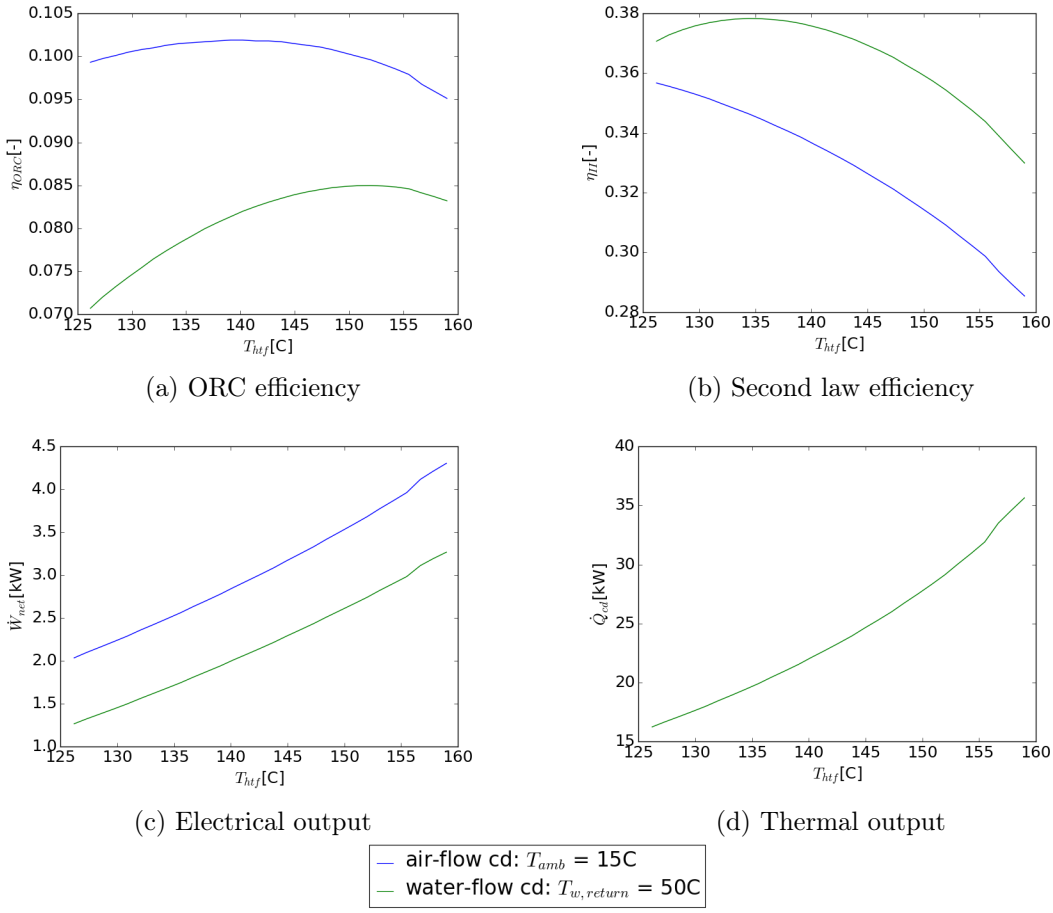

(a) ORC efficiency

(b) Second law efficiency

(c) Electrical output

(d) Thermal output

Figure 2.10: Comparison using air- (blue) and water- (green) flow condenser

However, if both cases are compared for similar temperature values, higher efficiency values are obtained when using the water-flow condenser. Figure 2.11 shows this efficiency comparison for a temperature of 25^{o}C. It is clearly shown that water-flow condenser provides a higher efficiency to the ORC than the air-flow condenser. This is mainly because of the higher heat transfer coefficients of the water, and also because of the fan consump-

tion of the air condenser. Maximum values are 9.95% and 9.84%, although the former is reached for a lower HTF temperature than the latter. It should be noted that for high HTF temperatures, air and water-flow condenser influence on the ORC is much lower: the higher the HTF temperature, the closer the evaporating temperature is to the critical point and thus the less the condensing temperature influences the cycle efficiency.

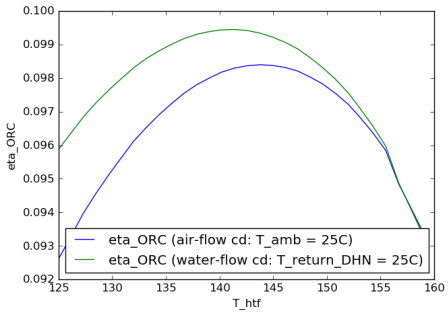

Figure 2.11: ORC efficiency

A comparison of the Second law efficiency for nominal operating conditions is presented in Figure 2.10b. The water-flow condenser now has the highest second law efficiency values. This is explained by the more favourable heat transfer coefficient of water and the higher consumption of the fan (for the air-flow condenser) with respect to the pump (for the water-flow condenser).

Net output electrical power is shown in Figure 2.10c. Under favourable conditions, both cases present an output power about 4kW. However, with return water at 50ºC the cycle output is limited to 3.2kW. Therefore, for typical operating conditions, if there is no thermal demand and the air condenser is used, the output power will be up to 1kW higher.

Thermal power output from the water condenser under nominal operating conditions is shown in Figure 2.10d. As with electrical power, hot secondary fluid has more influence on the output than cold secondary fluid. Under ideal conditions hot water production can be up to 39kW, and in worst-case conditions it can output 16kW.

2.4.3 Linear regression

The second law efficiency expresses the influence of the relevant variables on the cycle efficiency i.e. η_{II} is function of η_{ORC}, as stated in equation 2.20; however, it has a much flatter surface, as shown in Figures 2.8 and 2.7. Cycle performance has thus been extrapolated from the second law efficiency instead of ORC efficiency because its lower variability ensures a lower deviation outside of the considered range. A linear regression has been performed for this variable. Correlations have the following form and coefficient values are provided in Table 2.3:

$$Y = a_1 + b_1 \cdot T_{cf} + b_2 \cdot {T_{cf}}^2 + c_1 \cdot T_{htf} + c_2 \cdot {T_{htf}}^2 \tag{2.23}$$

where T_{cf} corresponds to T_{amb} for the air-flow condenser and to $T_{w,return}$ for the water-flow condenser, which must be expressed in ºC. It should be reminded that for the off-

design simulations, the mass flow rates and the inlet temperature of the secondary fluids are imposed to the model.

To account for the effect of the heat source temperature on the flow rate and on the net electrical power, an additional regression is required. It is expressed as the net output power as a function of the two temperature. Since the results present an relatively flat surface, a first order linear regression has been performed. The obtained correlations' coefficients (of the form of 2.23) are presented in Table 2.3. Although the ORC efficiency can be assumed similar under the same conditions for different ORC sizes, the output power varies with the scale of the ORC. Thus, when used in the micro-grid model, output power correlations have been normalized so it can be used for ORCs with different nominal capacities.

In Table 2.3, sub-indices *acd* and *wcd* refer to air and water condensers, and *HRE* and *LRE* refer to a high and low expansion ratio expander.

Table 2.3: Coefficients

	a_1	b_1	b_2	c_1	c_2
$\eta_{II,acd,HRE}$	$-5.88069776 \cdot 10^{-1}$	$4.28358532 \cdot 10^{-3}$	$-4.76586742 \cdot 10^{-5}$	$1.41450496 \cdot 10^{-2}$	$-5.67157252 \cdot 10^{-5}$
$\eta_{II,wcd,HRE}$	$-1.83049346 \cdot 10^{-1}$	$1.95586114 \cdot 10^{-3}$	$-1.12194277 \cdot 10^{-5}$	$8.90005113 \cdot 10^{-3}$	$-3.84177089 \cdot 10^{-5}$
$\eta_{II,acd,LRE}$	$-3.32125425 \cdot 10^{-1}$	$2.49732451 \cdot 10^{-3}$	$-1.39392467 \cdot 10^{-5}$	$1.00777464 \cdot 10^{-2}$	$-4.36940609 \cdot 10^{-5}$
$\eta_{II,wcd,LRE}$	$-1.60269044 \cdot 10^{-1}$	$1.58822305 \cdot 10^{-3}$	$-3.80968442 \cdot 10^{-7}$	$7.45991376 \cdot 10^{-3}$	$-3.32284206 \cdot 10^{-5}$
$\dot{W}_{net,acd,HRE}$	$-6.37092564 \cdot 10^{3}$	$-1.71805264 \cdot 10^{1}$	0	$6.78053231 \cdot 10^{1}$	0
$\dot{W}_{net,wcd,HRE}$	$-5.17739828 \cdot 10^{3}$	$-2.87192524 \cdot 10^{1}$	0	$6.19595654 \cdot 10^{1}$	0
$\dot{W}_{net,acd,LRE}$	$-4.11139107 \cdot 10^{3}$	-9.74947337	0	$4.55916951 \cdot 10^{1}$	0
$\dot{W}_{net,wcd,LRE}$	$-3.43899493 \cdot 10^{3}$	$-1.60899451 \cdot 10^{1}$	0	$4.22638183 \cdot 10^{1}$	0
$\dot{Q}_{wcd,HRE}$	$-5.49687048 \cdot 10^{4}$	$-9.20619550 \cdot 10^{1}$	0	$5.88049918 \cdot 10^{2}$	0
$\dot{Q}_{wcd,LRE}$	$-5.53284722 \cdot 10^{4}$	$-9.39397867 \cdot 10^{1}$	0	$5.91908673 \cdot 10^{2}$	0

Chapter 3

Design of a high expansion ratio scroll expander

The scroll expander developed in this thesis is based on the geometry proposed by Remi Dickes (ULg) in [13]. In this work, the geometry of the scroll itself was not modified, but all the other components (mechanical parts, generator, lubrication) were redesigned. The main goal is to create a more compact expander design with magnetic coupling power transfer. The new design is a semi hermetic, axially and radially compliant lubricated scroll expander with Oldham coupling, crank shaft power take off, and rotary mechanical power transferred through a magnetic coupling. The proposed expander's architecture has thus been mostly designed from scratch in the scope of this work.

This chapter introduces the new expander design detailing mechanical aspects of the parts as well as the lubrication system. All the designed parts have been drawn with the 3D mechanical CAD software *Solidworks 2016*. A Pipe and Instrumentation Diagram (P&ID) is also presented for both the expander and the overall ORC.

Since not only the design but also the manufacturing of the expander parts have been pursued in this thesis, a section with the manufacture and assembly process is also included. The expander has finally been assembled and connected to an ORC installation in Florida developed by STG International.

Fore the sake of conciseness, this manuscript only describes the contributions related to this thesis. Previous works related mostly to the design of the scroll geometry are not presented. The interested reader can refer to [13] and [26] for a detailed description of these previous works.

3.1 Overall design

Although scroll expanders are sometimes classified as rotary machines, when the fluid is expanded, the motion of the "orbiting" scroll is not a rotation but, as its name implies, an orbital motion. In order to transmit this mechanical power, it must be transformed into a torque and a shaft rotation, which, in turn, are transmitted to an electrical generator.

The first conversion is achieved through an Old'ham coupling as described later in this chapter. In a preliminary design [13], the connection between the shaft and the generator is direct, with an induction machine that has both coil (stator) and shaft (rotor) integrated

inside the expander casing. This configuration, common in the refrigeration scroll compressors, is usually referred-to as hermetic and implies a larger expander casing.

The main issue with this former design is that it derives from a compressor design where the electrical machine is immersed in the working fluid and is not optimized for the temperatures experienced in an ORC expander mode. Refrigeration scroll compressors have been well studied as ORC expanders in reverse operation, and in addition to the temperature limitation the electrical motor is usually oversized as an expander generator, which might result in low electrical efficiency and low power factor [27].

The proposed new design locates the induction machine outside of the expander where it is driven through a magnetic coupling. Magnetic couplings are designed to transmit torque between drive and driven components without mechanical contact. The shaft transfers the torque to the magnetic coupling internal half, which due to the magnets, spins the external coupling half. The latter is fit to a second shaft that transfers the torque to the generator. The main advantage of this kind of coupling is the absence of seal since the torque is transmitted through the casing. The system is therefore completely tight and leak-proof. A secondary advantage is the relative ease of torque measurement in comparison to hermetic, immersed generator.

Because the pressure between the scrolls is an important parameter to be optimized (to avoid radial leakages, but also excessive friction), a system has been designed that allows regulating the pressure in the backpressure chamber. This is achieved by the addition of a small refrigerant circuit comprising valves controlled manually.

Finally, because of the very different casing geometry, the lubrication system has also been completely redesigned and an horizontal configuration has been selected.

Figures 3.1a and 3.1b show respectively, the previous design developed in [13] and the new design developed in this thesis.

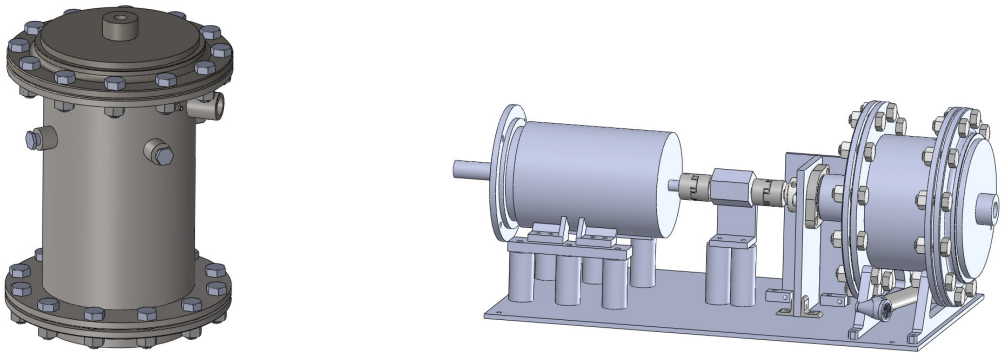

(a) (b)

Figure 3.1: Comparison of previous (a) and new (b) scroll expander prototypes

From a global point of view, the main innovations are:

– The generator is no longer contained inside the casing since the mechanical power is transferred through magnetic coupling to an external generator.

- The casing and all inner components of the expander have been redesigned.
- The expander axis is now horizontal and the whole assembly is mounted on to an aluminium plate.
- The axial force between the two scrolls can be actively controlled.
- An innovative lubrication system is proposed.

3.2 Mechanical design

The expander prototype is composed of 32 pieces assembled as shown in the section view provided by Figure 3.2. The parts, named after their function and ordered as they appear in the design, are the following:

1. Casing top plate
2. Gasket (2x)
3. Counter pressure top
4. Teflon seal
5. Counter pressure bottom
6. Scroll stator
7. Scroll rotor
8. Oldham coupling
9. Thrust bearing
10. Linear guide (4x)
11. Bearing sleeve
12. Shaft adapter
13. Counterweight
14. Lower stator
15. Main journal bearing
16. Stator support cylinders (4x)
17. Main case
18. Crank shaft
19. Bottom journal bearing
20. Bottom journal bearing support
21. Magnet coupler
22. Casing bottom plate
23. Magnet coupler cover
24. Case support (2x)

Reference to these parts in this document will use the convention P/N 1,2,3..etc. An exploded view of the expander is also provided in Figure 3.3, describing how the prototype is assembled. The parts have been labeled so that they can be easily distinguished.

3.2.1 Magnetic coupling

Magnetic couplings are designed to transmit torque between drive and driven parts without mechanical contact. In the scope of this work a synchronous permanent magnetic coupling has been used. As it name indicates, it is composed of Rare Earth (RE) permanent magnets. The magnets are arranged concentrically on the rotor in order to avoid slipping and thus maximize the transmittable torque.

This model, shown in Figure 3.4a, incorporates a containment shroud (P/N 23) between internal (P/N 21) and external rotors that encapsulates the internal rotor while positioned

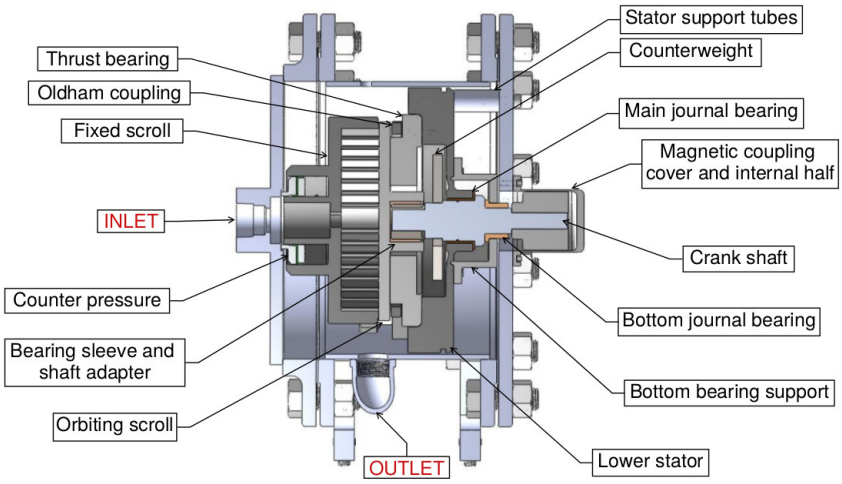

Figure 3.2: Section view of the scroll expander prototype

within the bore of the external rotor. The containment shroud is installed in the drive-side unit: it is bolted to the case bottom and covers the internal half, as shown in Figure 3.2.

The rotors transmit torque via magnetic fields that pass through the containment shroud. Thus, the material selection of the latter is a key element since it defines the torque capacity and heat generation. The mechanical properties of the shroud may add heat to the process due to the friction of the magnetic field passing through it. The resistance of the magnetic field can result in magnetic strength or eddy current losses. In order to minimize these effects, the shroud and internal rotor are generally made from stainless steel or Hastelloy because it provides a good balance between containment pressure and eddy current losses. In the case when eddy current losses must be excluded, alternative materials such as ceramics should be used.

As shown in Figure 3.4b, the external rotor, which is mounted in the driven side, contains alternating poles of permanent magnets concentrically mounted over the inner rotor. The latter contains opposing magnets and is encapsulated within a cover impermeable to fluids. The air gap is ensured to be minimal.

In stationary state the north and south poles of the rotors are opposite to each other leading to a completely symmetrical magnetic field. The magnetic field lines are moved once the rotors start spinning, implying a torque transmission through the air gap. The flux lines are represented in Figure 3.4b. If the maximum coupling torque is exceeded, the maximum torsion angle will also be exceeded bringing with it the interruption of torque transmission.

3.2.2 Crank shaft

The crank shaft (P/N 18) transfers the torque received from the scroll to the electrical generator. The proposed new design (Figure 3.5a) no longer consists of an induction machine placed inside the expander, but of an external generator coupled to the expander through a magnetic coupling. The shaft is thus used to transfer the torque to the magnetic coupling

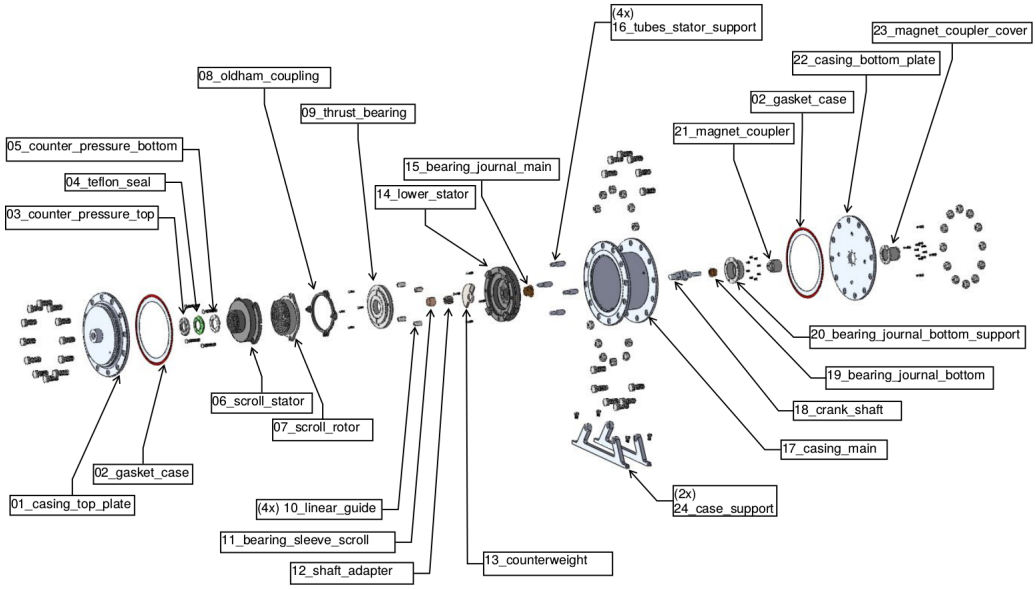

Figure 3.3: Exploded view of the scroll expander prototype

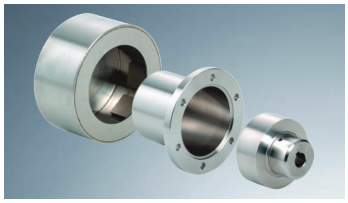

(a) From left to right: external rotor, containment shroud and internal rotor

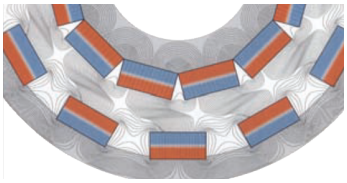

(b) Run of flux lines between the internal (up) and external (down) rotors

Figure 3.4: Magnetic coupling design (a) and magnetic field (b)

internal half. To meet these new requirements, the crank shaft has been substantially redesigned.

As shown in Figure 3.5b, from one extreme to another, the crank shaft is connected to the orbiting scroll (top bearing), the counterweight, the lower stator (main bearing), the bottom journal bearing and the internal coupling half.

Mechanical axial and radial compliance of the scrolls (P/N 6 and 7) to take up wear and minimize leakage, is maintained by the three journal bearings and one thrust bearing (P/N 9). Radial forces produced by the shaft are supported by the journal bearings whereas the axial load is supported by the thrust bearing, which resides on the lower stator.

The orbiting scroll motion is translated into a shaft rotation by an offset crank with an intermediary piece, the shaft adapter (P/N 12), to provide the required degree of freedom to make the conversion. Two pieces play an important role in between the orbiting scroll neck and the crank shaft: the sleeve bearing and the shaft adapter. The sleeve bearing (P/N 11) i.e. top bearing is made from oil impregnated bronze and maintains a locational

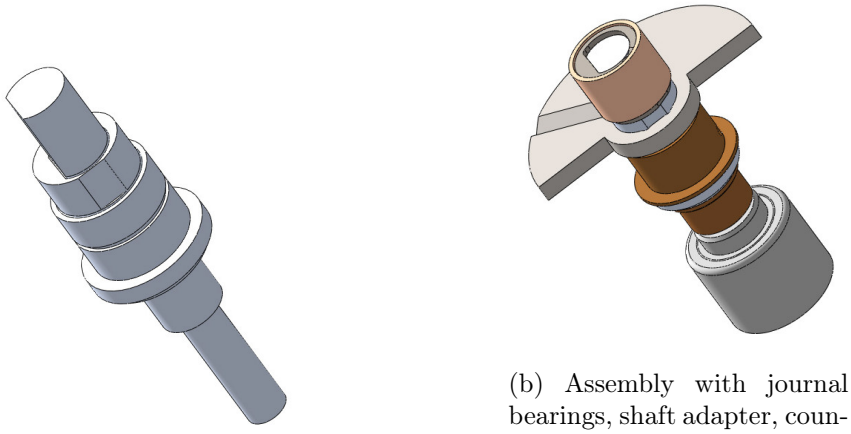

(a) Proposed design

(b) Assembly with journal bearings, shaft adapter, counterweight and magnetic coupling

Figure 3.5: Crank shaft

interference fit with the scroll neck and a free running fit (i.e. clearance fit) with the shaft adapter. The latter, made from mild steel, maintains a free running fit with the crank shaft.

The counterweight, required to avoid mechanical vibrations produced by the eccentric motion of the orbiting scroll, is aligned in a well-defined position with the crank shaft. A flat surface on the shaft is thus again needed.

The center of the lower stator contains the main journal bearing (P/N 15), also made of oil impregnated bronze, which has an interference fit with the lower stator and a free running fit with the shaft.

The bottom journal bearing (P/N 19) is not mounted in any main part of the expander but on a specifically-designed piece that supports it, as described in section 3.2.4. This piece allows to center the bearing with the shaft so that the former can support the radial forces produced by the latter. Again, there is a clearance fit between this bearing and the shaft to ensure contact-free spinning.

Finally, at its extreme, the crank shaft is placed into the internal magnetic coupling half, with which it remains fixed and aligned via a shaft key.

The length of the shaft is determined by the casing, which has been made as short as possible within the constraints imposed by the new oil lubrication system. Several holes in the journal bearings or open sections in the shaft adapter ensure the lubrication of the shaft.

3.2.3 Counterweight

As already mentioned, a counterweight is required to avoid mechanical vibrations produced by the eccentric motion of the orbiting scroll. Its main role is to cancel the centrifugal force caused by the orbiting parts i.e. the orbiting scroll, the sleeve bearing and the shaft adapter, which is given by equation 3.1:

$$F_c = m \cdot w \cdot R^2 = F_{os} + F_{sb} + F_{sa} \tag{3.1}$$

where F_c, F_{os}, F_{sb} and F_{sa} refer to the counterweight, orbiting scroll, sleeve bearing and shaft adapter, respectively.

Figure 3.6 shows the optimized design for the counterweight (P/N 13).

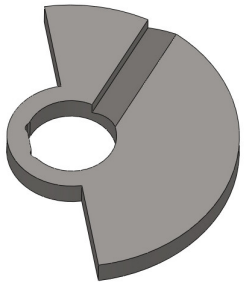

Figure 3.6: Counterweight

The tool *Mass Properties* from SolidWorks has been used to determine properties such as the center of mass or axes and moments of inertia for the moving parts.

3.2.4 Bottom journal bearing support

This piece (P/N 20) has been designed to hold the bottom journal bearing aligned with the shaft. The support is mounted on the lower stator and bolted together via eight M5 threaded fasteners. These eight holes may not be sufficient to ensure the alignment between the shaft and the bearing, even if they are made with a CNC machine. In order to achieve a proper alignment, a male profile left at the bottom of the support (Figure 3.7b) is placed into a circular groove on the lower stator surface. The fitting is displayed in Figure 3.8, where a section view of the support, the lower stator, the bearing and the shaft is provided.

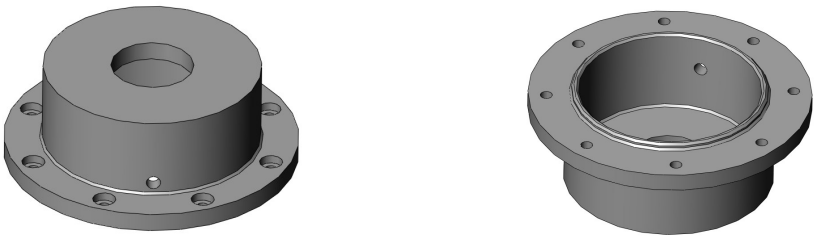

(a) Top trimetric view

(b) Bottom trimetric view

Figure 3.7: Bottom journal bearing support

A journal bearing requires rigidity and accurate alignment, but without heavy pressing forces. For this reason, a locational interference fit is preferred between the bottom bearing and its support.

In order to ensure the shaft lubrication, a hole is drilled in the lateral surface of the bottom bearing support to let the oil in, as shown in Figure 3.7.

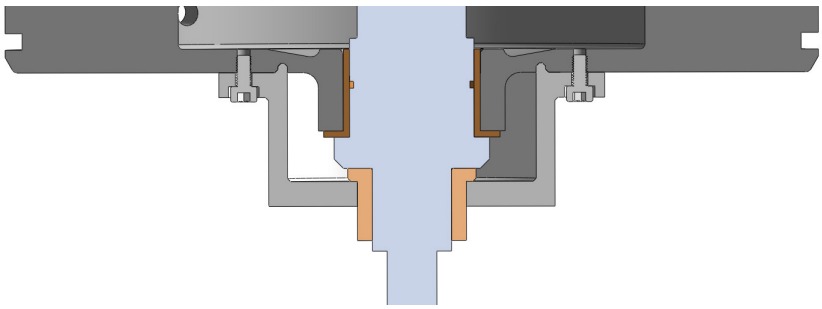

Figure 3.8: Section view of bottom journal bearing support assembly

3.2.5 Lower stator

The lower stator (P/N 14) supports the thrust bearing, and thus the whole axial load created by the two scrolls. It contains the main journal bearing in its center. The counterweight also rides above the lower stator, below the thrust bearing.

As explained in section 3.2.4 and shown in Figures 3.8 and 3.9, a groove has been drilled on the bottom surface of the stator in order to place the bottom journal bearing support. To bolt the latter, eight holes have been drilled and tapped on the same surface next to the groove.

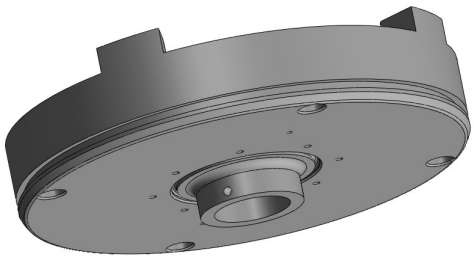

Figure 3.9: Lower stator

The lower stator position in the case is defined in respect of the case bottom by the four cylinders that support it, later detailed in section 3.2.6. These cylinders are designed to fit in the four large clearance holes close to the outer diameter shown in Figure 3.9.

The lower stator plays an important role in the new lubrication system: it ensures the tightness between the upper and lower parts. To that end, the space between the outer diameter of the stator and the inner diameter of the casing must be filled up. This is achieved through an O-ring that impedes the pressurized oil to flow around the low stator and instead forces it through oil channels leading to the bearings. A groove on the cylindrical surface of the stator is drilled to hold the O-ring, as shown in Figure 3.9 and in both left and right extremes of the section showed in Figure 3.8.

3.2.6 Stator support cylinders

These pieces (P/N 16) are designed to support the lower stator and all parts above it (i.e. thrust bearing, Oldham coupling and both scrolls). The supporting structure should be compatible with the lower stator (as developed in [13]), whose connection is ensured by four holes.

The most straightforward solution would be a flange welded to the internal surface of the case and that would support the lower stator. Four holes (of the same diameter than those from the lower stator) drilled on that flange would allow to align the lower stator with all the assembly. However, this approach presents some difficulties in fabrication, which could eventually lead to a poor alignment and a twisted assembly.

The selected design consists of four cylinders that go from the lower stator to the bottom plate of the case, whose length determines the space between these two parts. It is shown in Figure 3.10.

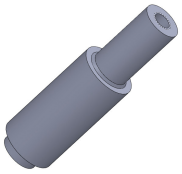

Figure 3.10: Stator support cylinder

One extremity (left in Figure 3.11) of the cylinder is inserted into the holes of the lower stator and is bolted from the other side. The other extremity (right in Figure 3.11) is inserted into similar holes on the case bottom plate and bolted from the outside of the casing. This configuration is shown in Figure 3.11, in which the cylinder is coloured in red. With this design, the lower stator is fixed to the casing bottom plate and also aligned with the main axis.

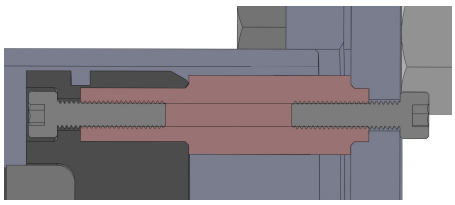

Figure 3.11: Cross section of one cylinder (in red) in the assembly

3.2.7 Main casing

The expander casing (P/N 17), shown in Figure 3.12, is the largest piece in the assembly and could have a complex design from a manufacturing point of view. To ease the machining process, the proposed design is based on standard pipe dimensions so that it can be built by welding two standard flanges onto a standard pipe. This also allows reducing the costs, which would have been much higher with non-standardized components.

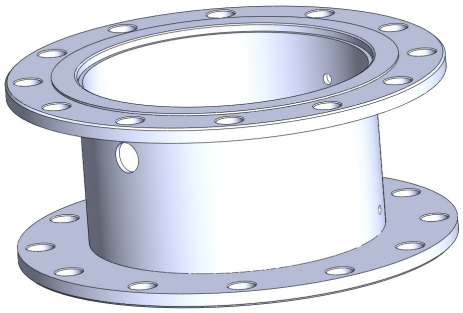

Figure 3.12: Expander casing

The main port in the case is the expander outlet, which corresponds to a 1" NPT hole drilled on the casing surface as close as possible to the scroll outlet position without interfering with access to the flange bolts. Since the axis of the expander is now horizontal, the outlet is located at the bottom and pointing downwards. An elbow is welded to the case in the desired angular position to connect the outlet fitting. This elbow is made from forged steel, allowing a good welding quality that resists the required pressure.

The second main port is the oil inlet, which is part of the lubrication circuit. This port is a tapped 1/8" NPT hole placed between the lower stator and the bottom plate of the casing, i.e. where all the oil resides.

The case contains a third port for the pressure sensor and a thermocouple. Both sensors are used in the scroll to take measures of the temperature and pressure in the last expansion chamber. The wire of the thermocouple is more flexible than the one of the pressure sensor, so the port has been placed as close as possible to the location of the latter. A wire gland M12x1.5 screwed into the port allows the wires to cross the casing.

3.2.8 Case top and bottom plate

The design of the top (P/N 1) and bottom (P/N 22) plates is similar to that proposed in [13] with a few modifications. A port has been added to the flat surface of the top plate, shown in Figure 3.13a. Its main goal is to regulate the Back Pressure Chamber (BPC) as described in section 3.3.1.

To support the stator, four holes have also been added to the bottom plate, as displayed in Figure 3.13b. They consist of a cylindrical flat-bottomed hole that guides the cylinders at the desired location and of a clearance hole that allows bolting them (Figure 3.11). The flat-bottomed hole has a transition fit in order to ensure accurate location by compromising between interference and clearance.

3.2.9 Case support

Since the expander axis is horizontal, a support (P/N 24) is needed to hold it up to the right place and height. To avoid welding, the proposed architecture consists of two feet that are bolted to the casing's flanges as shown in Figure 3.1b. The feet have two clearance holes for a 7/8" bolt (i.e. the same size than those of the flanges), and two clearance holes for an M12 that allow bolting the scroll onto a plate (Figure 3.14).

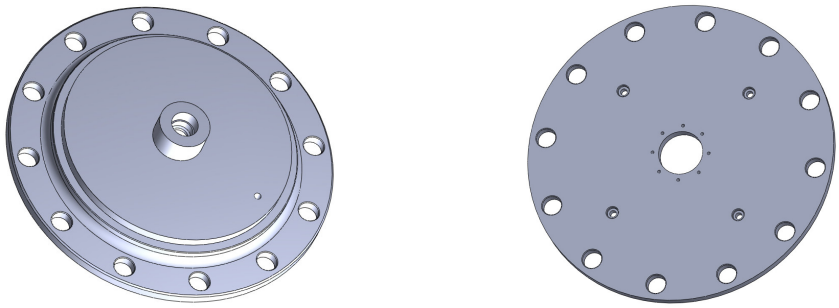

(a) Top (b) Bottom

Figure 3.13: Casing plates

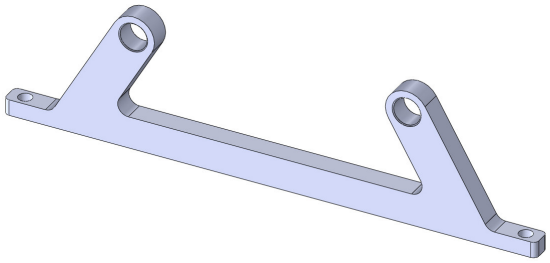

Figure 3.14: Expander foot

3.2.10 Driven shaft, magnetic coupling external rotor and mount bearings

The driven side is mainly composed of the external part of the magnetic coupling, the torque transducer, and the motor. As shown in Figure 3.1b, two mount bearings serve as support to align the external rotor with the rest of the magnetic coupling installed on the drive side. Both bearings are bolted to an aluminium plate that adjusts them at the desired height.

The first bearing supports the external rotor and is placed at the end of the external rotor to minimize interferences with the magnetic field. Its ID fits thus the neck of the rotor, i.e. 50 mm. The bearing mount has been designed to fit the bearing OD, i.e. 90 mm, and to be bolted to the aluminium plate. The resulting design is shown in 3.15c. The holes have been drilled and counterbored so that the bolt heads do not interfere with the magnetic coupling.

The second bearing serves as an additional support to the shaft. Again, the bearing ID fits the shaft OD and the mount bolts it to the aluminium plate. The latter consists on a 15mm-thick plate that has four clearance holes for the purpose of bolting two mount bearings (Figure 3.15b). To increase the stability and the stiffness of the support, a second plate is bolted on the side of the first one with an angle of 90 degrees (Figure 3.15a). In order to fix them in the right position, both plates are bolted to the assembly base plate.

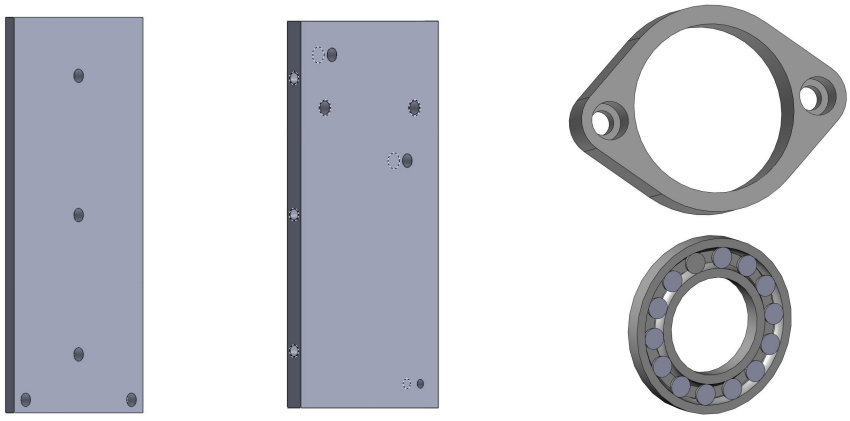

(a) (b) (c)

Figure 3.15: Aluminum plate (b) for mount bearings (c) and stabilizing plate (a)

3.2.11 Motor and torque transducer

The driven shaft torque is recorded by the torque transducer. The latter adds to the rotating shaft conditioning electronics and an A/D converter. The digital signals are then read by stator electronics and are converted to a high-level analog output signal, e.g. $\pm 10V(DC)$.

Shafts must all be aligned with the driven shaft that comes from the external magnetic rotor. The motor and torque transducer must thus be positioned in line with the expander. For this purpose, an ensemble of six tubes and two bridges has been installed under the motor base. Also an L-profile piece and two tubes raise the torque transducer to its correct position. The resulting design is shown in Figure 3.1b. Two sets of spider couplings are used to connect the shafts.

The position of the motor is defined by the assembly base plate. Six threaded rods bolted to the latter go through the tubes and the motor feet bridge, at the top of which a nut fixes them. The bridge is at the same time bolted to the motor feet. Similarly, the torque transducer is positioned by two threaded rods connected to the L-profile piece. Straightness of rods is difficult to ensure because of the low thickness of the base plate. However, shafts' extremes are ensured not to collide one to another by virtue of the adjustment of spider couplings.

3.2.12 Oil pump and motor

The lubrication system, detailed in section 3.3.2, is composed by a dispensing pump and an external motor. Because the heights of the pump and the motor shaft do not coincide, a bridge has been designed to raise the pump to the motor shaft level (Figure 3.16). A spider coupling is used to connect both shafts. As with the expander, an aluminum plate is used as a base for the assembly.

An oil reservoir has also been connected to the inlet of the pump. It is made of a $2^1/_2$" diameter and 6" length straight nipple. Its threaded ends are covered by two caps, as shown in Figure 3.24. The required ports mentioned in section 3.3.2 are drilled and tapped onto these caps.

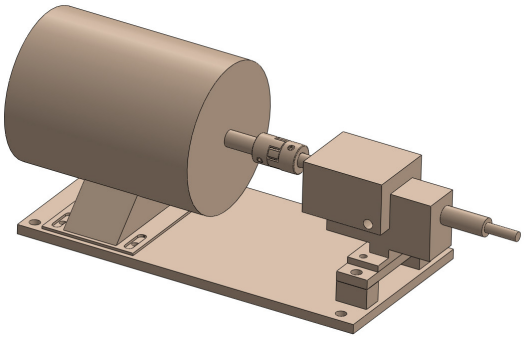

Figure 3.16: Oil pump and motor assembly

3.3 Fluid flows and instrumentation

3.3.1 Back-pressure chamber

The cavity between the floating seal and the upper scroll is referred to as the Back Pressure Chamber (BPC), in which an intermediate pressure can be maintained. In a compressor, this pressure is imposed by the bleed hole, a small hole between the BPC and the compression chambers, which is optimally located on the fixed scroll.

The pressure in the BPC has two major effects on the scroll machine: it influences the pressure between the two scrolls, and it controls the lifting up of the floating seal. These two effects are explained hereunder.

The scroll machine used here is equipped with an axial compliance system: the (nominally) fixed scroll is not tightly bolted to the casing and has a (small) axial degree of freedom. The force equilibrium applied to the fixed scroll is therefore of primary importance: an insufficient upper pressure can lead to axial scroll unloading (and therefore excessive radial leakage), while a too high pressure can lead to excessive friction and hot spots in the scrolls [28].

The floating seal (P/N 3-5) moves as a piston to actuate a by-pass system between the high pressure inlet and the low pressure chamber. The by-pass is closed when the floating seal is forced into an upper position by pressure in the BPC. Insufficient intermediate pressures can lead to fully by-passed working fluid around the expander from high- to low-pressure manifolds.

The intermediate pressure is thus a key parameter, which can influence the by-pass, the axial unloading and the friction. However, this system was primarily designed for compressors and does not necessarily operate well in an expander. In particular, the use of a bleed hole to control this pressure does not work during start-ups [28], and defining its optimal position is problematic.

To ensure a proper intermediate pressure in the expander, the bleed hole system is augmented by an active valve control: the pressure is controlled by a pipe connected from the BPC to the outside of the casing. A sketch of this regulation is shown in Figure 3.17. Inside, the port is connected to a second port in the fixed scroll neck that leads to the BPC.

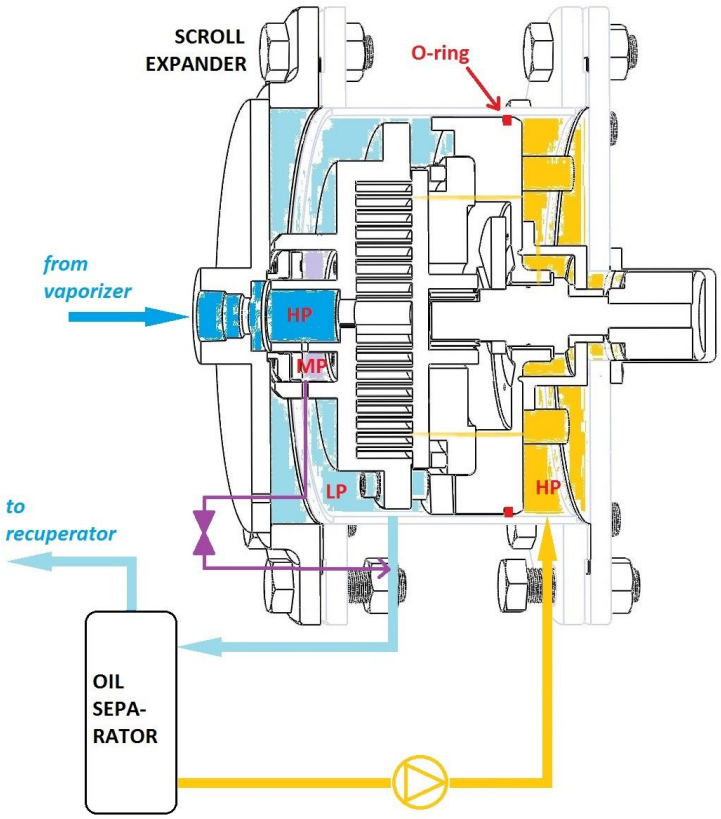

Figure 3.17: Intermediate pressure control (blue: WF, yellow: oil)

Outside, the pipe is connected to the outlet working fluid port through a valve, thereby connecting the medium pressure to the low pressure manifold. A small opening in the inlet scroll neck also connects high pressure zone with the BPC (Figure 3.17).

By regulating the opening of the valve, the intermediate pressure can be varied from the low pressure to the high pressure, taking advantage of the (assumed-to-be) small flow between the high pressure zone and the BPC. It should finally be noted that a spring is also added between the fixed scroll and the floating seal (Figures 3.23g and 3.23h) to complement the effect of the pressure and prevent bypass at start up operation.

3.3.2 Lubrication system

As detailed in section 3.2.5, the lower stator divides the inside of the expander in two hermetic chambers defined as the upper and lower chambers, experiencing (slightly) different pressures. The proposed lubrication system consists in filling up the lower chamber with lubricant. The pressurized lubricant escapes the lower chamber to the upper chamber through perforated paths inside the expander parts that belong to the oil circuit. These paths distribute the lubricant to all the critical locations of the expander.

The oil recuperated in the upper chamber must finally be returned to the lower chamber. It is however mixed with the expansion fluid, and therefore an oil separator is imposed

after the expander outlet. As shown in Figure 3.18, the type of system installed in the cycle uses centrifugal force created in a spiral to separate the oil. About 95-98% of the oil can be separated and accumulated at the bottom of the reservoir, from where it can be extracted and returned to the main oil reservoir. The return is controlled by a valve. The expansion fluid separated from the oil exits the separator at the top and is sent to the recuperator.

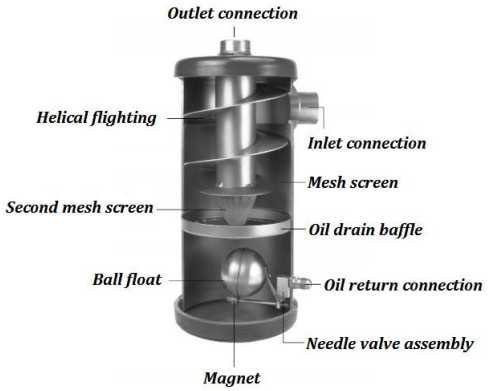

Figure 3.18: Oil separator sketch

As mentioned, there is a main reservoir from where the oil is pumped to the expander and to which the oil arrives from the separator. Besides the main inlet and outlet, the reservoir has a third port regulated by a valve that allows evacuating or loading oil in a quick and direct way. The lubrication circuit also contains a bypass, so that excessive oil pumped to the scroll can return to the inlet of the pump.

The oil circuit flow pathways explained above are illustrated in the pipe and instrumentation diagram in Figure 3.20 from section 3.3.3.

The chosen pump for the circulation of the oil is the smallest dispensing pump without motor for lubricating oils offered by SHURflo. The model, i.e. GPCV2V and shown in Figure 3.19b, offers a cast iron pedestal rotary external gear pump with 3/8" NPT inlet and outlet ports and a relief valve on discharge. Maximum rotational velocity is 1725 RPM, which is enough to circulate the oil in this lubrication system.

The pump is connected to a Variable Frequency Drive (VFD) speed controlled AC motor ideally suited for pumps. The chosen model, shown in Figure 3.19a, is from Leeson with catalog number 102919.00. The VFD unit is a Mitsubishi FR-D710W.

(a) Motor

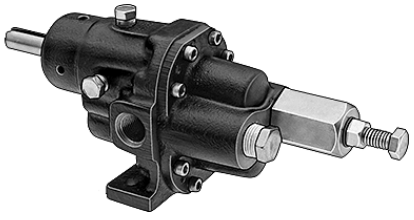

(b) Oil pump

Figure 3.19: Lubrication circuit components

3.3.3 Expander P&ID

The ensemble of the scroll contains several types of instrumentation and manifolds:

- Pressure transducers: measure the pressure at the first and last chamber of the scroll, at the inlet and outlet of the scroll, as well as at the back pressure chamber.
- Pressure indicators: placed at some points of the circuit to display pressure.
- Thermocouples: measure temperature at the first and last chamber of the scroll.

and pipes:

- Copper tube: 1/4" or 3/8" tube used for the lubrication circuit and for regulating the back pressure chamber regulation.
- Connecting hose: 1" NPT used for the working fluid.

A pipe and instrumentation diagram (P&ID) has been designed to establish the interconnections of process equipment and the instrumentation used to control the process. The developed P&ID for the scroll expander studied in this thesis is presented in Figure 3.20.

Since the scroll expander has been implemented in one of STG's ORC test rig, its P&ID has been added to a whole ORC-Solar plant P&ID diagram provided by STG. The system is presented in Figure 3.21. The P&ID has thus been used as a schematic drawing for laying out the installation.

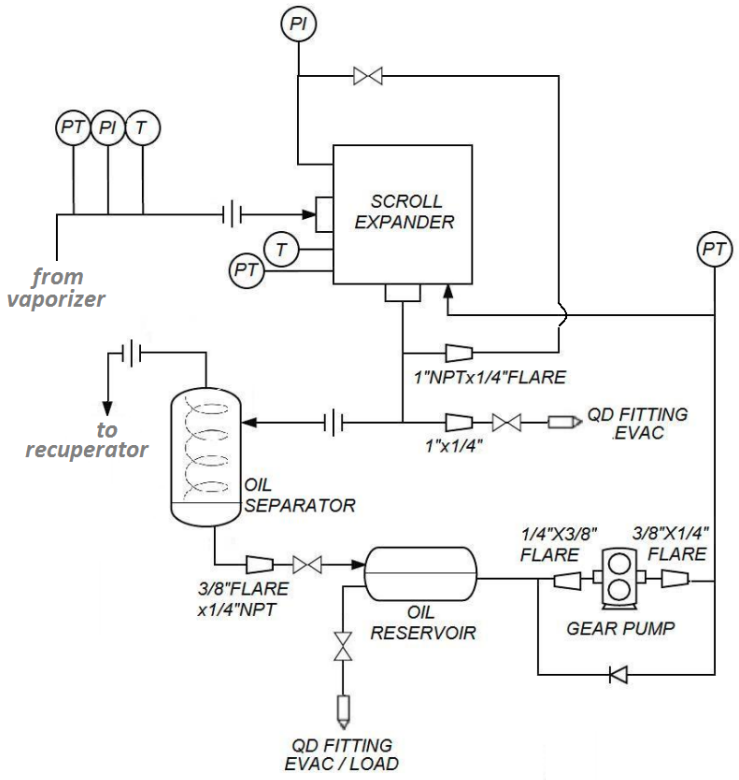

Figure 3.20: P&ID of the expander developed in this thesis

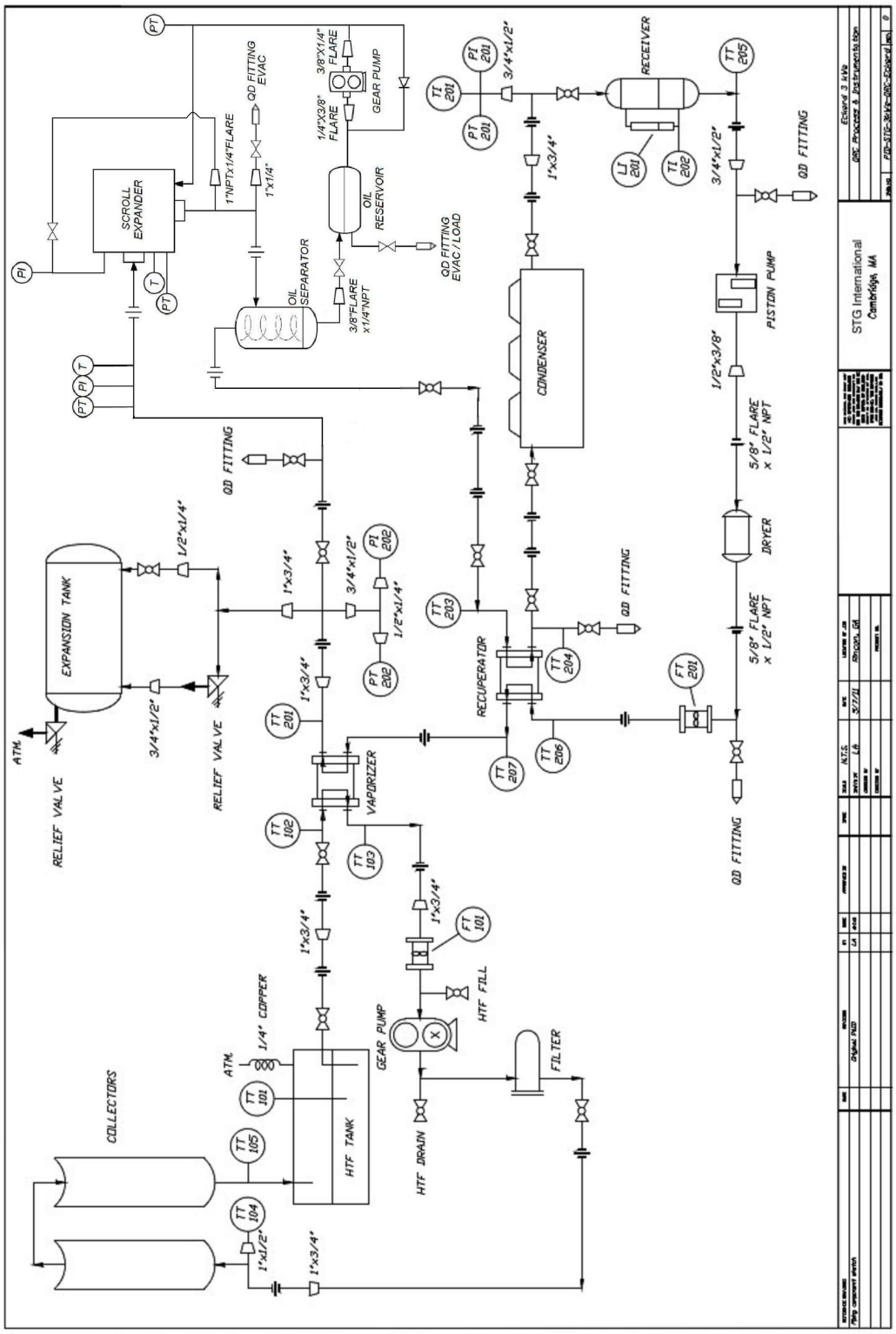

Figure 3.21: New P&ID of the ORC Solar Plant from STG (adapted from [3])

3.4 Manufacturing process

Once the mechanical and piping design has been completed, the expander has been constructed. The expander parts have been manufactured and components such as motors, pumps, pipes, valves, fittings and fasteners have been procured.

3.4.1 Parts sent to machining

Most of the designs presented in section 3.2 that correspond to inner parts from the expander require smooth surfaces and/or small tolerances. These parts have therefore been sent to a professional machining shop in order to ensure accuracy. A drawing of each part can be found in the Annex.

3.4.2 Parts machined at MIT

The rest of the parts have been machined locally at the Area 51 machining shop from MIT Edgerton Center (pictures can be found in Annex). For the interested reader, machining processes used to manufacture the parts are explained and illustrated in Annex.

3.5 Assembly and integration in an ORC

Finally, parts have been assembled and the expander has been integrated in an ORC from STG International. The process is illustrated in Figures 3.23, 3.24 and 3.25. In order to optimize the location of the parts to add in the ORC, a CAD model of the latter has been created (Figure 3.22a). To have a clear vision, relevant components have been coloured and pipes have not been displayed. The resulting installation is shown in Figure 3.22b.

(a) ORC sketch

(b) STG's ORC

Figure 3.22: Expander (violet), evaporator (yellow), recuperator (turquoise), liquid receiver (copper), oil separator (green), oil pump (beige), oil reservoir (blue)

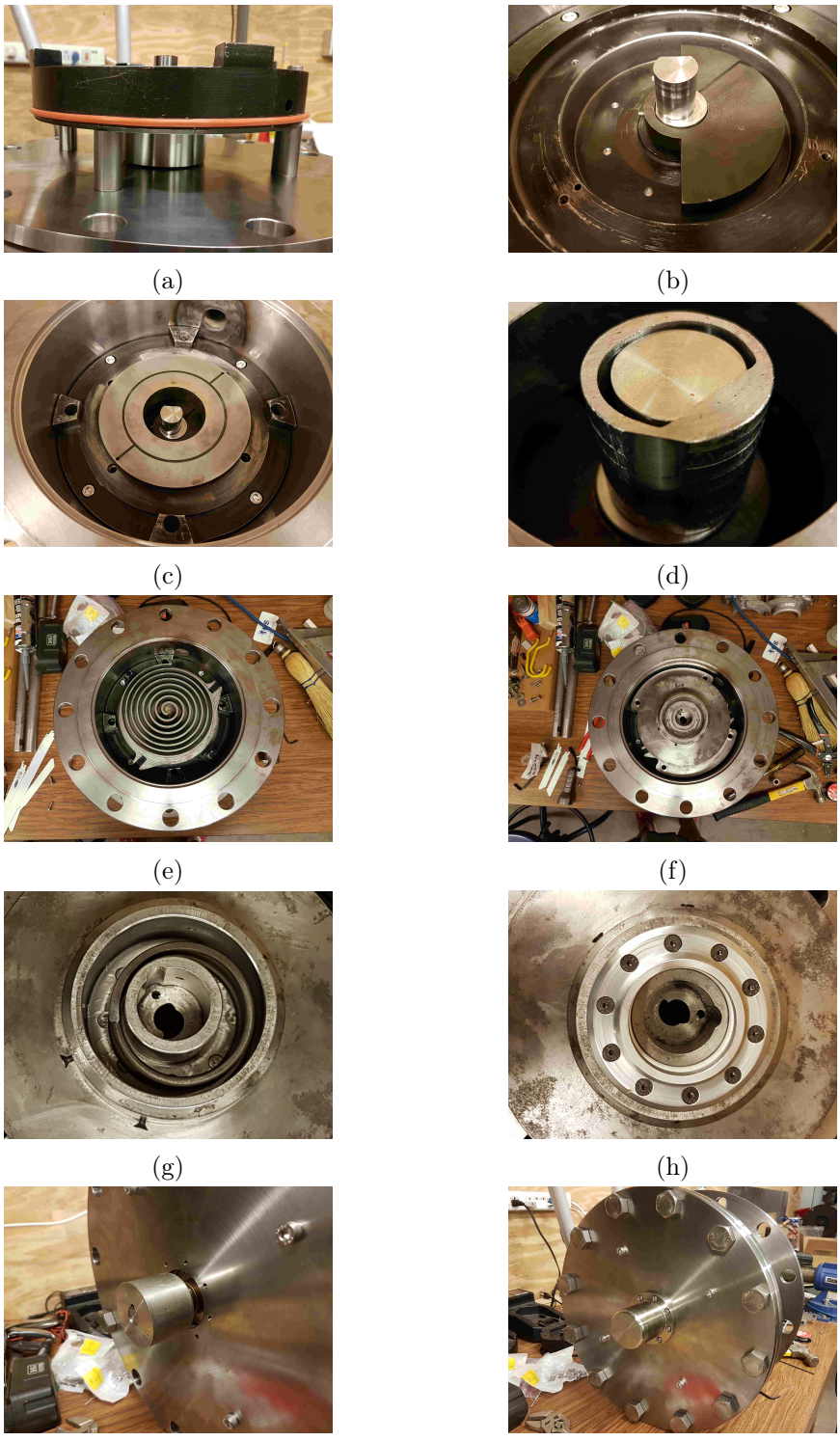

(a) (b) (c) (d) (e) (f) (g) (h) (i) (j)

Figure 3.23: Scroll expander assembly

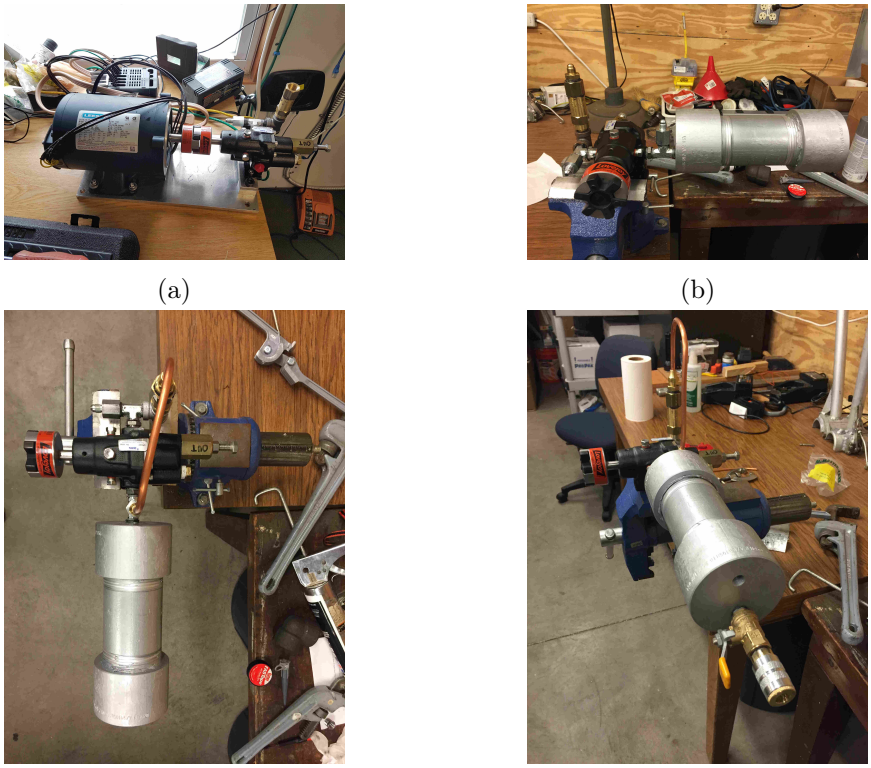

(a) (b)

(c) (d)

Figure 3.24: Oil circuit assembly

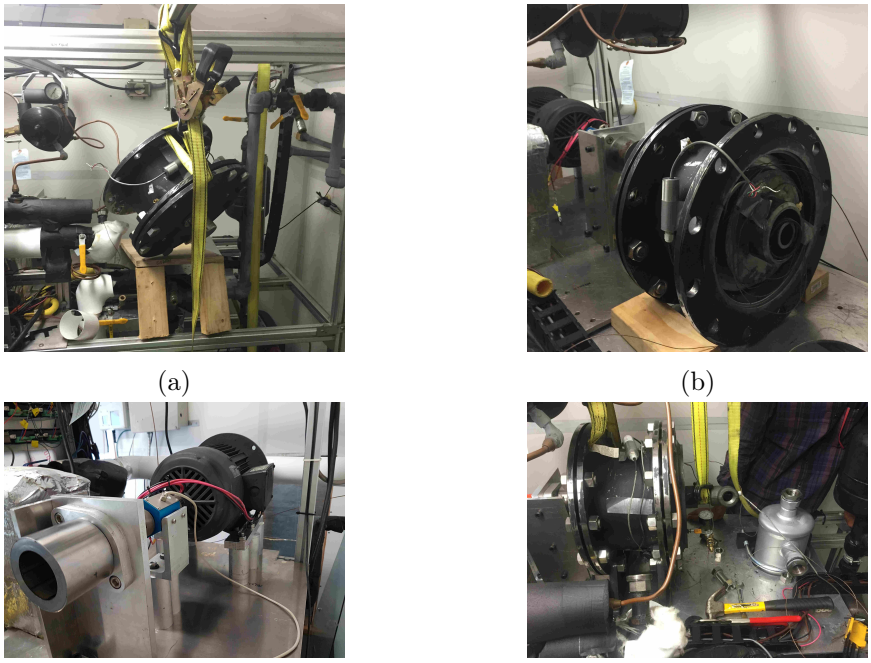

(a) (b)

(c) (d)

Figure 3.25: Integration in ORC

Chapter 4

Building model for health clinics in Lesotho

The work described in this thesis focuses on the region of Lesotho in Africa, which is mountainous country. More than 80 % of its land is above 1800 m, with the lowest altitude being 1400 m. Because of its altitude, throughout the year Lesotho has lower temperatures than other regions at the same latitude. Winters are cold and snow is not uncommon. Buildings such as clinics or schools are thus in the need of heating systems to maintain reasonable comfort.

The micro-grid system intends to provide not only electrical service to the community but also meet thermal demand for institutions such as health clinics and schools. The micro-grid model uses these demands as an exogenous input to dispatch the energy production at each time step. Demand dynamics must therefore be estimated a-priori to run the model.

This chapter presents a building model developed to predict the thermal demand of typical health clinics in Lesotho. The main idea is to create a single model with very few inputs that can be used for various building typologies and communities. Most of the clinics in Lesotho have a similar profile in terms of building architecture, construction materials, occupancy and energy consumption. The model thus considers equivalent buildings characteristics for all communities. However, not all the communities feature equal clinic sizes. Therefore, building floorplan area is left as an input so that the model can rescale building-related parameters. By setting weather conditions and building footprint the developed model should predict a realistic thermal demand.

Because detailed characteristics of the building construction and orientation are difficult to determine with certainty at each site, a lumped parameter approach is selected, in which important parameters are determined from historical data colleced at representative sites. This is achieved through an optimization whose objective is to reduce the discrepancy between model prediction and field measurements. This approach is facilitated by the availability of a part-year dataset collected by STG International, of measurements corresponding to inputs (weather conditions, inside temperature) and outputs (clinic energy consumption).

Although it may not be explicitly refected, the challenge of acquiring and processing

sparse data has been an integral part of the work presented in this chapter. Several data-processing codes have been developed to correct, order and classify the raw data received from Lesotho. Some measurements were only partly available and the gaps had to be filled, some sensors did not provide reliable data and the measurements had to be rejected, etc. This task, although time-consuming, could not be avoided since desynchronized or erroneous data would not have provided acceptable results.

The data processing presented in this chapter has been performed in the Python language, mainly using the Pandas library. The building model itself has been developed in Engineering Equation Solver (EES).

4.1 Boundary conditions

The demand (either heating or cooling) of a building depends on its response to various boundary conditions, the most relevant being the outdoor temperature, the solar irradiation, the heat inputs, the internal gains, etc. In this section, a dataset as comprehensive as possible is built, gathering historical boundary conditions for typical clinics in Lesotho. The data originates from on-site monitoring campaigns by STG beginning in 2015. This data is processed and classified with the purpose of using it for the building model.

4.1.1 Weather data

The weather data was acquired by STG's weather stations, installed in four different clinics in Lesotho (Figure 4.1). Additional sensors were also installed inside and outside the clinic.

Figure 4.1: Weather station being installed on the roof of a typical clinic in Lesotho

4.1.2 Electricity data

Currently, most clinics in Lesotho do not have a dedicated thermal heating system. However, electricity consumption data shows that some of the buildings deploy electric space heaters, as can be seen in Figure 4.2a. Other buildings also burn coal in "Queen Anne" type stoves during cold months (Figure 4.2b).

Electricity consumption is distributed across four data acquisition channels logged and uploaded by a GSM connected smartmeter (IOM-QEC1) installed at each site, as shown in Figure 4.3. Clinic consumption is observable from channel 2, which has five clear peaks during Monday to Friday operating hours. Channel 1, representing staff housing, displays

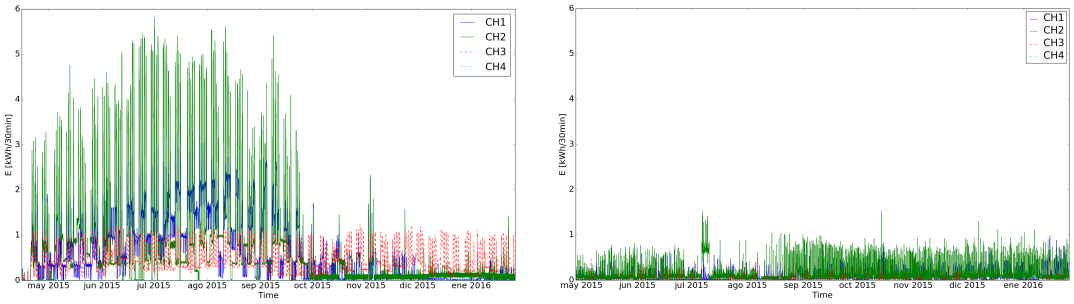

(a) With electrical heaters (LDF)

(b) No electrical heaters (St Davis)

Figure 4.2: Comparison of clinic electrical consumption

much lower peaks and feature consumption during night and weekends, when the clinics are closed. Because the microgrid simulation makes use of an extensive dataset for household consumption dynamics, the staff housing demand is disaggregated from the data used to determine the unique clinic demad dynamic.

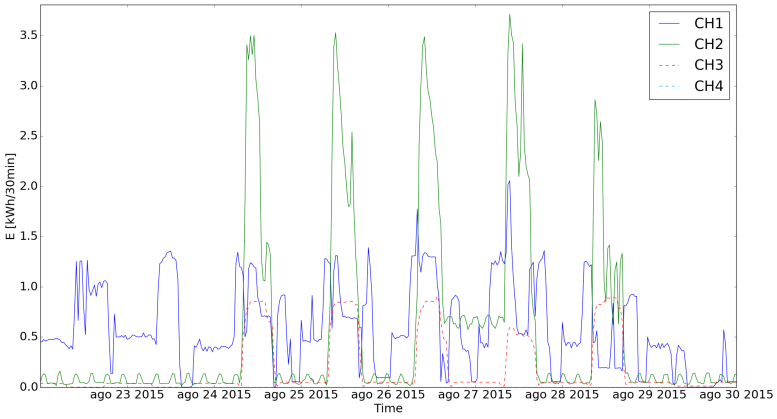

Figure 4.3: Electricity data from 22nd to 30th August 2015 (Khubetsoana)

Electricity data from Figure 4.2a accounts not only for the consumption from lightning and equipment, but also for the load due to electrical heaters. Electrical consumption has a direct effect on the thermal equilibrium, since it is directly or indirectly transformed into heat gain for the building. Moreover, because it is often the only sort of heat input, it is an influential parameter for the indoor temperature of the building. As such, electricity consumption is equivalent to a fictitious heating consumption.

Pure consumption of equipment and lightning (i.e. without electrical heaters) is difficult to define for the whole year. However, because electrical heaters are not used during the warm months (Figure 4.2a), the equipment and lightning signal can be resolved for this period. As shown in Figure 4.2a (from October to February) and 4.2b, equipment and lightning consumption is generally constant over time. In order to obtain a whole-year data of lightning and equipments consumption for the model, consumption data from warm months has been extrapolated for a full year.

Table 4.1: Geometric data from buildings

	Value
"Flat roof" height	3 m
Maximal height	4 m
Roof inclination	22.5 º
Footprint	200 - 300 m^2
Perimeter	60-80 m

Table 4.2: Material properties (values from library from software *PEB* [29])

	Material	λ W/mK	ρ kg/m^3	C_p J/kgK	t m	%
External Wall	Concrete block	1.4	2000	1000	0.20	-
Roof	Corrugated steel	50	7800	450	0.02	-
	Wood beams	0.13	300	1880	0.10	20
	Air	0.026	1.2	1000	0.10	80
Floor	Concrete	1.63	2400	1050	0.20	-

4.2 Modeling

4.2.1 Architectural characteristics

In lieu of detailed building drawings, approximate architectural designs of typical clinics have been provided by STG workers (Table 4.1). All clinics are built with inclined roofs. The so-called "flat roof" height correspond to the lowest height of the external walls. The maximal height correspond to the highest point of the roof. Since perimeter and height of the clinics are known, walls surface are easily computed. The roof inclination being approximately 22.5º, its surface is 110% of the building horizontal area.

Construction materials are basic and no insulation is present. Walls are made of concrete blocks, the floor is made of a concrete layer and the roof is made of a thin layer of corrugated steel supported by wood beams. Material properties of each wall are provided in Table 4.2.

Building windows have a single glazing, implying a high heat transfer coefficient (U) and a high Solar Heat Gain Coefficient (SHGC). The latter accounts for the fraction of admitted incident solar radiation through the window (both directly transmitted and absorbed and subsequently released inward).

$$U_{window} = 5.8\ W/m^2K \qquad SHGC = 0.86 \tag{4.1}$$

The total wall thermal resistance (equation 4.2) is composed of a conductive resistance and constant external and internal surface resistances linked to convection and radiation. The final values are computed using the wall thickness and the material conductivity (equation 4.3). If more than one layer is present, the resistances of each layers are summed. $R_{se,wall}$ and $R_{si,wall}$ values for each type of wall are presented in Table 4.3. The overall heat transfer coefficients are thus obtained as the invert of resistance (equation 4.4). The wall capacity is a function of the material density, thickness and specific heat (equation

4.6). Equations 4.2 to 4.6 are applied for exterior walls, floor and roof.

$$R_{wall} = R_{se,wall} + R_{t,wall} + R_{si,wall} \tag{4.2}$$

$$R_{t,wall} = \frac{e_{cb,wall}}{\lambda_{cb}} \tag{4.3}$$

$$U_{wall,ext} = {R_{wall}}^{-1} \tag{4.4}$$

$$AU_{wall,ext} = (A_{wall,ext} + \theta_{frame} \cdot A_{window}) \cdot U_{wall,ext} \tag{4.5}$$

$$C_{wall,ext,m^2}\,[^J/_{m^2K}] = Cp_{cb} \cdot \rho_{cb} \cdot e_{cb,wall} \tag{4.6}$$

Table 4.3: External and inner wall surface resistance in $^{m^2K}/_W$

	R_{se}	R_{si}
External wall	0.04	0.13
Roof	0.04	0.1
Floor	0.04	0.17

4.2.2 Energy balances

Heat transfer in walls, roof and floor

Heat transfer in the walls is modeled by a two-resistances and one-capacity (2R1C) network, as proposed in [30]. Total resistance of the model is equivalent to the invert of wall heat transfer U coefficient. The adjustment of the wall resistances and capacity is done by means of two non dimensional factors θ and ϕ, as shown in Figure 4.4, accounting for accessibility of the wall thermal mass from both sides.

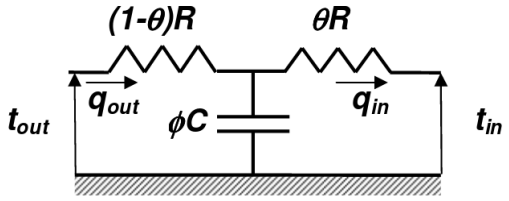

Figure 4.4: Adjusted 2R1C network for isothermal boundary conditions wall [30]

External insulation implies a larger resistance on the external side of the wall (i.e. a smaller θ) and a more accessible wall capacity from the internal node. The θ factor is therefore called accessibility and defines the position of the capacity on the wall resistance. Factor ϕ defines the portion of total wall capacity accessed by a 24 hours solicitation period [30].

For a certain wall, the following energy balances are applied (equations 4.7 to 4.9). A similar energy balance is applied for external walls, roof and floor.

$$\dot{Q}_{wall,out} = \frac{A_{wall}}{R_{wall} \cdot (1-\theta)} \cdot (T_{out} - T_{wall}) \tag{4.7}$$

$$\dot{Q}_{wall,in} = \frac{A_{wall}}{R_{wall} \cdot \theta} \cdot (T_{wall} - T_{in}) \tag{4.8}$$

$$\dot{Q}_{wall,out} - \dot{Q}_{wall,in} = \frac{\partial U}{\partial \tau} = C_{wall} \cdot \phi \cdot \frac{\partial T}{\partial \tau} \tag{4.9}$$

Heat transfer in windows

Heat transfer in windows can refer to the heat transferred because of the temperature difference (through conduction, convection and infra-red radiation), or to the solar gains (the solar irradiation through the glazing). Neglecting solar gains for the moment, the windows network model is assumed to be a single thermal resistance, with one node *out* and one *in*, and no thermal mass.

$$\dot{Q}_{window} = AU_{window} \cdot (T_{out} - T_{in}) \tag{4.10}$$

Although approximate windows surface data is available, there is no information on their orientation. Solar absorption of south-oriented or north-oriented windows can therefore not be distinguished. Moreover, available irradiation data is measured on a horizontal surface or as direct normal irradiation. Models are needed to evaluate the incident diffuse and beam radiation incident on the vertical surface of the window.

The level of insulation generally being low, there is also a significant solar gain through the walls, which depends on their absorbance. For typical opaque thick-insulated roofs in, e.g., Europe, sunlight does not strongly influence heat transfer. Rooftops in African institutions may consist of comparatively thin corrugated metal supported by wood beams. An approach that generalizes the building's irradiation absorbency as a whole is used in lieu of specific detailed information for heat transfer analysis of the envelope. In addition, because the available irradiation data is measured on horizontal surfaces, the approach adopted (equation 4.11) is a function of the building footprint. A non-dimensional overall absorptivity factor α_I is added to take into account the proportion of total horizontal radiation absorbed by the building as solar gains.

$$\dot{Q}_{sun,in} = I_h \cdot A_{floor} \cdot \alpha_I \tag{4.11}$$

Infiltrations

Building infiltration is highly influenced by its construction. Modern buildings are increasingly tight, ensuring lower infiltrations and implying lower heating demand. However, this is rarely the case for buildings in developing countries. Moreover, there is a significant difference during the night (when the building is closed) and the day (when people are going in and out of the building through several doors that connect to the outside). Therefore, two different Air Changes per Hour (ACH) are considered: a higher value during operating hours, and a lower value for night hours. The energy balance is presented in equation 4.12, where the volumetric flow of infiltrated air is computed by equation 4.13.

$$\dot{Q}_{inf} = \dot{V}_{inf} \cdot \rho_a \cdot Cp_a \cdot (T_{out} - T_{in}) \tag{4.12}$$

$$\dot{V}_{inf}\,[m^3/h] = ACH \cdot V_{in} \tag{4.13}$$

Internal gains

Internal gains are mainly caused by occupancy, lightning and equipment. A nominal human being releases 70 W during normal-work body metabolism. Although occupancy during the day is high, clinics are empty during nights and weekends. Some exceptions such as pregnant women at risk of giving birth are allowed to stay in the clinic during closed hours. However, occupancy in that period is considered null, since these represent a minor fraction of overall clinic traffic. The occupancy factor in operation hours (7.30AM to 6.00PM) is

considered constant with a linear increase and decrease during opening and closing (Figure 4.5). First and last hours account for 25% of occupancy, and second and second-to-last hours move from 25% to 100%.

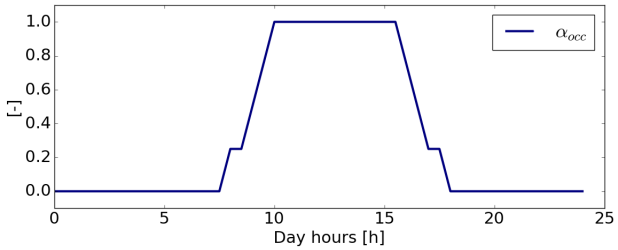

Figure 4.5: Occupancy factor α_{occ}

Although clinics are closed during evenings and weekends, electricity demand is not null. Equipment such as refrigerators impose a constant electrical load of about 0.8kWh (with some small variations, as shown in Figure 4.3). Electricity demand based on lightning and equipment is extrapolated from the available data (section 4.1.2). The total internal gains are finally computed in equation 4.14.

$$\dot{Q}_{gains} = q_{occ} \cdot \dot{n}_{max,occ} \cdot \alpha_{occ} + \dot{Q}_{cons,el} \tag{4.14}$$

Global energy balance

All the above-detailed heat transfers are graphically summarized in Figure 4.6. Through an energy balance (equation 4.15) that accounts for the building internal capacity, the model can compute the indoor building temperature. The required heating loads are computed by setting up a simple regulation that intends to maintain the envelope temperature to a desired value. The selected set points follow the ASHRAE standards [31] [32], with a 20ºC temperature for working hours, and 15ºC for non-working hours, as recommended in [33].

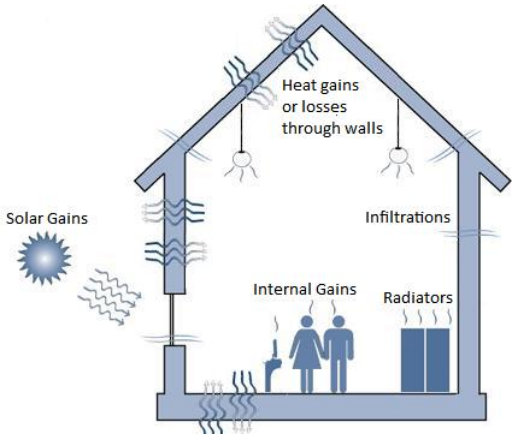

Figure 4.6: Heat transfer in building envelope

$$\dot{Q}_{wall,in} + \dot{Q}_{floor,in} + \dot{Q}_{roof,in} + \dot{Q}_{window} + \dot{Q}_{inf} + \dot{Q}_{sun} + \dot{Q}_{gains} + \dot{Q}_{heating} = \frac{\partial U}{\partial \tau} = C_{in} \cdot \phi \cdot \frac{\partial T}{\partial \tau} \tag{4.15}$$

Table 4.4: Model parameters

	Value
$ACH_{dormant}$	0.4 h^{-1}
$ACH_{operation}$	1.5 h^{-1}
T_{ground}	5.4 ºC
$n_{occ,dormant}$	0 pers

4.2.3 Additional unknown parameters

The additional model parameters are shown in Table 4.4. Although the ground temperature slightly varies through the year, it is set to a constant value to simplify the model. The selected value is based on [34].

Typical rural institutional buildings in Lesotho do not employ mechanical ventilation systems. Although implementing one would improve air quality, the access to this type of technology remains low. With the lack of a ventilation system, the main driver of ACH for the facility is air infiltration. As previously stated, two ACH are defined. In lieu of fan pressurization test data to determine building airtightness, typical ACH values are used, varying from 0.3 to 0.6 h^{-1} for closed windows and doors (non-operating hours), and from 1.3 to 1.6 h^{-1} for open windows and doors on more than one side (operation hours) [35]. Because the optimization already includes 4 variables, adding two parameters to the optimization would singnificantly increase the model search space. Since the range of possible ACH is limited in comparison to other variables (Table 4.5), ACH are set to typical values (Table 4.4) to simplify the optimization.

4.3 Optimization

4.3.1 Objective function

The proposed model is developed to predict the thermal demand of a clinic. Model inputs such as outdoor temperature, solar irradiation and equipment and lightning electrical consumption are available from the monitoring data. Other model parameters such as occupancy or proportion of absorbed irradiation are estimated and validated.

To that end, the proposed methodology consists in computing the indoor temperature by using measured thermal loads (i.e. electricity data), measured outdoor temperature and known building characteristics as inputs. Unknown parameters are subject to an optimization. The goal is to minimize the error between the obtained temperature profile and indoor temperature measured data (equation 4.16). Because T_{in} is a non-linear function of the different boundary conditions, the optimization problem is also non-linear and not necessarily convex.

Once a solution has been found, the obtained optimal set of parameters is considered representative of the building's physics. It is however important to set approximate and/or realistic boundaries to the optimization variables, to avoid some mathematically correct but non-physical solutions. It is also important to keep in mind the uncertainty of the measurement data (due to incompleteness, sensor inaccuracies, etc.), which could lead to biased solutions.

$$min(error) = \sum (T_{in} - T_{in,meas})^2 \tag{4.16}$$

Table 4.5: Optimization variables and imposed ranges

	Range
$\alpha_{Cwall,ext}$	[1,8]
α_{Cin}	[1,10]
α_I	[0.01,0.40]
$n_{max,occ}$	[15,35]

4.3.2 Optimization variables

As defined in section 4.2.1, building walls are made of concrete blocks, which convey a significant thermal inertia to the system. However, the following data-related limitations should be taken into account:

- External walls surface is estimated and could vary from reality
- Thickness is set to the most used typical values from concrete-blocks sold in the market
- Concrete block properties vary in a wide range. The selected type may differ from real one

Given these factors, the computed wall capacity (equation 4.6) may deviate from properties of real walls in practice. To improve the model, a multiplicative factor α_{Cwall} is added to equation 4.6 and submitted to the optimization.

Internal walls of the building are also made of concrete blocks. These heavy walls, along with various pieces of furniture and equipment, represent increments in the internal mass of a building. In view of a general lack of site survey data to characterize a building's interior contents, a multiplicative factor α_{Cin} is added to the internal capacity and adjusted via the optimization.

The final optimization variables and their boundaries are shown in Table 4.5. Because windows tend to be small, it is considered that the building can absorb a maximum of 40% of the total irradiation. Maximal occupation is set as a function of the building surface area. It is considered that a clinic of 230 m^2 has a capacity of approximatively 35 people. However, clinics may be over or undersized and the actual quantity of people may vary. Capacity factors limits are therefore set so that capacity approximates realistic values.

4.3.3 Optimization Results

Exhaustive search is prohibitively expensive computationally, and therefore a Genetic algorithm (GA) is employed to search the map of possible solutions and to ensure reaching a global optimum. The GA is preferred to the Nelder-Mead algorithm for this problem (the latter was used to run several optimizations with different starting guess values and was frequently trapped at local optima). The global optimum obtained with GA leads to the optimized parameters presented in Table 4.6, which represent realistic values.

In order to evaluate the optimization results, a histogram plot is performed (Figure 4.7) over the error distribution. Results show a centered error distribution. Moreover, 90% of the values are comprised between ±2. Root-mean-square error (RMSE) is also calculated to quantify the standard deviation of predicted values in respect of measured

Table 4.6: Optimized model parameters

	Value
$C_{wall,ext}$	$1.170 \cdot 10^8$ J/K
C_{in}	$7.236 \cdot 10^7$ J/K
α_I	25 %
$n_{max,occ}$	34 *people*

ones. Because temperature sensors can easily deviate by more than 1 degree from reality, the obtained value $RMSE = 1.33$ is considered acceptable.

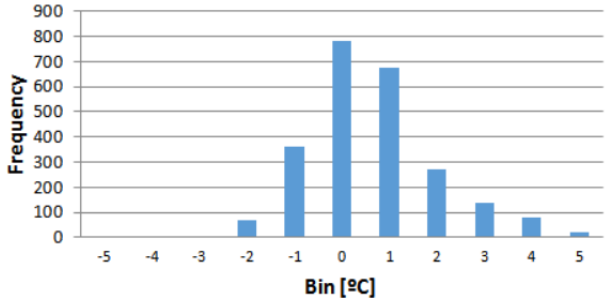

Figure 4.7: Histogram of obtained error values from optimization

Figure 4.8 shows five days of the time-set used for the optimization. The available profile from data and the predicted by the model are compared.

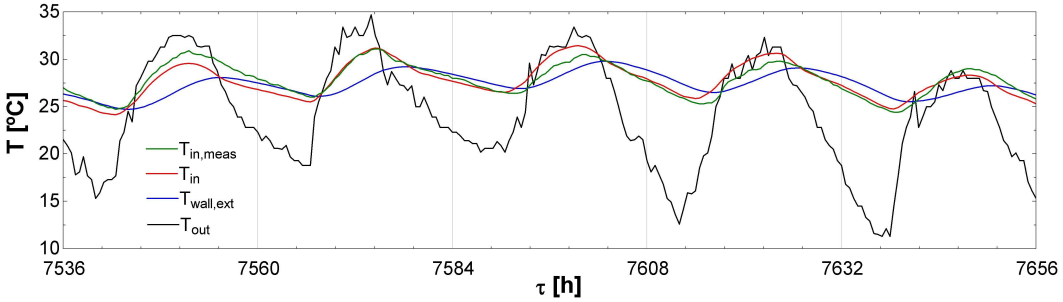

Figure 4.8: Comparison of data (green) and obtained (red) indoor temperature profiles

4.4 Simulation

With all model parameters defined, the building can be simulated for a year. Figure 4.9 shows the final model, with all inputs, parameters and outputs indicated.

After a first simulation that identified the heating load needed to maintain the inside temperature at the set point value, a maximum heat of 70 kW was encountered during the coldest days. In order to deal with the trade-off between comfort level and the investment cost of a heating system, a peak power of 40 kW for the heating system is suficcient. A rule based strategy is applied to control the heat injection. The strategy is designed to have a fast-response without being too aggressive. Figure 4.10 provides the temperature

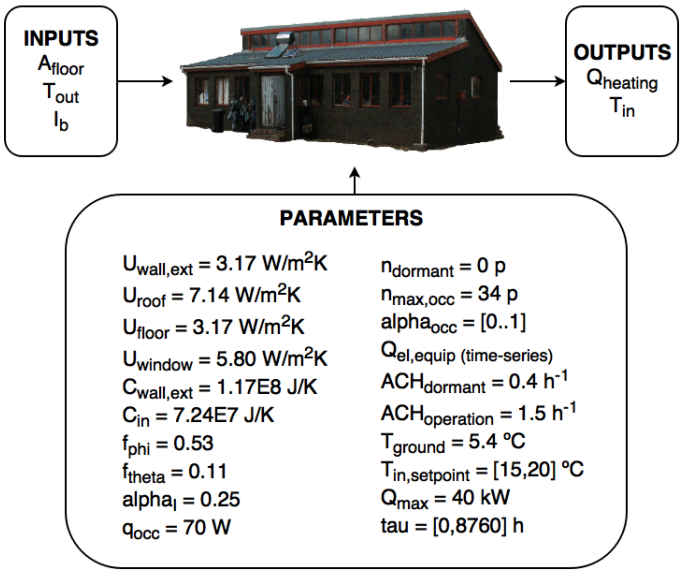

Figure 4.9: Clinic model

profiles and heating demand of the coldest week of the year. Wednesday experiences the worst-case: it takes two hours for inside temperature to get to 18 ^{o}C. Although the result may not seem acceptable, it should be stated that this is the worst possible case, which is rare (occurs only once or twice a year). Moreover, during the coldest weeks, the heating could be turned on an hour before than during the rest of the year, providing more comfort to the people. The selected system capacity is thus considered acceptable.

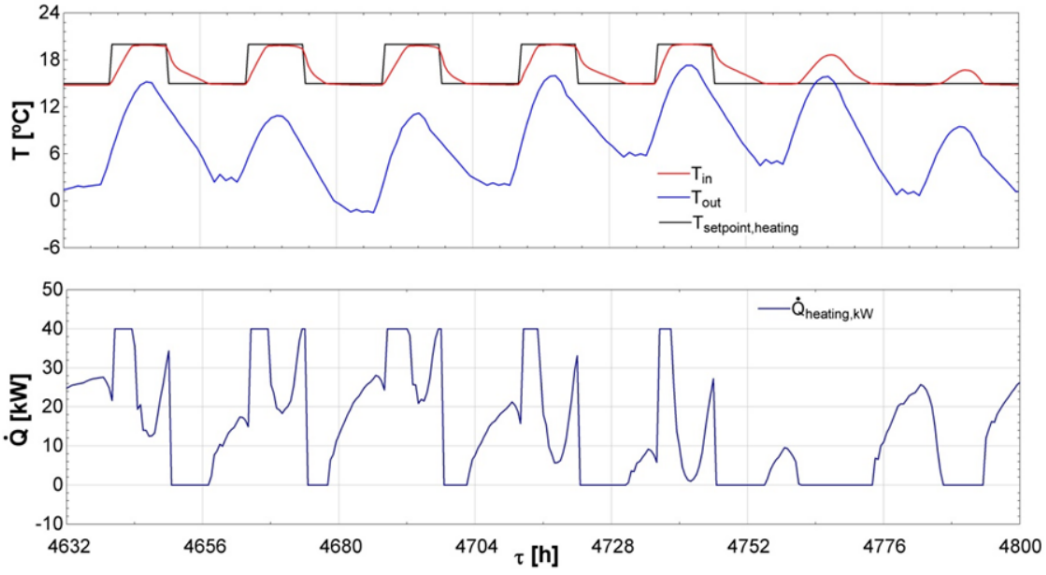

Figure 4.10: Temperature profile and heating from the coldest week of the year

Figure 4.11 provides a general view of the heating requirements throughout the year. It is worthwhile to note that there is no heating demand for almost half a year. As expected, and comparing to Figure 4.2a, June to August are the months with the highest heating demand. Annual consumption of heating (Table 4.7) is reasonable, considering the specified

Table 4.7: Annual consumptions

	Value
E_{th}	21734 $kWh_{th}/year$
$E_{th,spec}$	95 $kWh_{th}/m^2 year$

comfort level zone (15-20ºC) and a building footprint of 230 m^2. It should be noted that the computed consumption only accounts for space heating and not for the sanitary hot water.

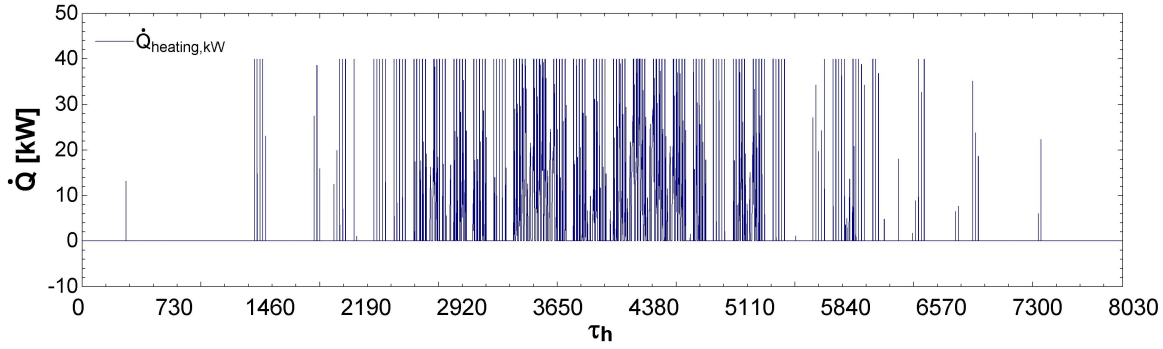

Figure 4.11: Heating consumption through a year

Chapter 5

Modeling and optimization of microgrids

This chapter presents the dynamic simulation of a hybrid microgrid system. The studied configuration considers PV, Parabolic Trough Collectors (CSP), ORC and LPG generation, as well as chemical battery storage and TES.

The model, implemented in Python, iteratively evaluates configurations meeting variable demands (heat and electricity) according to an energy balance, calculates the microgrid cost structure based on cash flows, and seeks to minimize the cost recovery tariff. The energy balance is calculated at each timestep (user selectable with 1 h default) and a rule based control logic directs the flows of energy between generation, storage and demand nodes. The control logic is formulated to reach decisions for the following possibilities:

- Which combination of generators should be used to meet the loads?
- What is the optimum output level of selected generators?
- When should the storage units be charged or discharged?

For each configuration, the model allocates at each timestep the output of an available or combination of available generators to meet the load. A power outage condition due to insufficient generation is not permitted in the system, i.e. the micro-grid is designed to meet 100% of demand, and will do so with backup fossil fuel generation if necessary. The complement of generators therefore always includes an LPG genset sized for the peak load of the microgrid.

To improve computational efficiency, some complex components have been implemented as functions derived from detailed models of those components. For example, the ORC performance is fitted from the model developed in Chapter 2. Similarly, thermal demands of a clinic and a school are represented as a time series derived from the model developed in Chapter 4.

5.1 Overall description

A hybrid micro grid allows designers to leverage the strengths of certain generator types against the weaknesses of others [36]. For example, PV has a high investment cost but

low operating costs and no CO_2 emissions. Fuel-based generators on the contrary can be bought at a fairly low price, but have high operation (fuel) and maintenance costs. Also, unlike fuel-based generators, PV and CSP are bound to solar intermittency and require storage. While CSP is initially more costly than PV, it allows for thermal energy storage, which is more cost-effective than battery storage at scale.

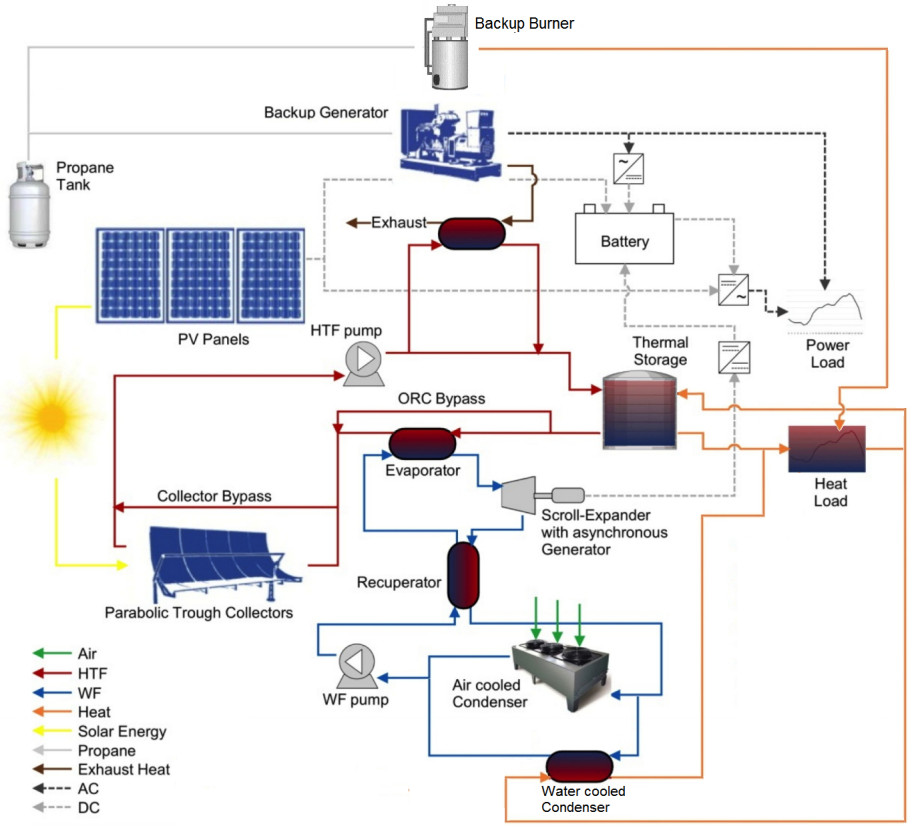

Figure 5.1: Hybrid micro-grid configuration (adapted from [36])

Figure 5.1 describes the studied system. It presents the following features:

- The electrical load can be met by the backup generator (operating with LPG or propane), the PV system, the ORC, the battery (via an inverter), or a combination of those.
- The thermal load can be covered by the high temperature thermal energy storage (TES), the condenser of the ORC (in CHP mode) or by a backup burner.
- The main heat source of the ORC is the CSP system through the thermal storage. The TES enables extended operating hours to times without solar irradiation.
- The TES is charged by the CSP but also through the thermal potential of the exhaust gases of the LPG generator.
- The ORC can also be used with the exhaust gases of the LPG generator as heat source in case no CSP system is installed.

Table 5.1: Micro grid equipment for electrical load

Generator	**Source**	**Storage**
PV	Solar	Battery
CSP	Solar	TES
ORC	TES	Battery
LPG Genset	Fuel	Battery
Inverter	Battery	-

Table 5.2: Micro grid equipment for thermal load

Generator	**Source**	**Storage**
CSP	Solar	TES
TES	CSP	-
ORC	TES	-
LPG Burner	Fuel	-

– The battery bank can be charged variously by the ORC, the PV or the backup generator.

A summary of the micro grid equipment used to meet the electrical and thermal loads is presented in Tables 5.1 and 5.2, respectively.

5.2 Electrical and thermal demands

Determining an accurate load demand profile is a key factor in order to obtain optimized micro-grid designs [37]. The case study considered in this work is based on on-going work in the community of Ha Nkau in the Mohale's Hoek District, Lesotho [36]. The community is currently without access to electricity and comprises:

– 84 households

– 5 small businesses

– a school

– a church

– a health clinic

Electrical loads are obtained from an estimation tool developed in [36], which processes the data available from similar communities in a probabilistic distribution function. The annual load profile for the case study is thereby obtained. The electrical demand of the clinic is estimated from the available data processed in Chapter 4. In the absence of specific data, the school consumption is assumed similar to that of the clinic, with the exception that it is null during the nights and weekends. The clinic is also closed during these periods of time, but its refrigeration systems lead to a non-null (although small) load.

In the considered system, the microgrid only supplies the thermal demand of the clinic and the school. This demand is evaluated using the physical building model developed in

Table 5.3: Lesotho coordinates and orientation of the PV panel

	Value
latitude	-29º
longitude	28º
surface tilt	28º
surface azimuth	0

Chapter 4. Because of the lack of data, no thermal load prediction model has been developed for schools. However, since both buildings are very similar in terms of construction, similar responses can be assumed for both of them. Therefore, schools demand is also computed by means of the building model for clinics.

5.3 Solar Irradiation model

The solar irradiation model is used for both the CSP and the PV system. It should therefore be able to compute the beam radiation incident on a north-south tracking collector and the incident total radiation on a tilted surface. The input data is the typical meteorological year (TMY) data from EnergyPlus, provided as an epw file. The model has been developed in Python and makes use of the following libraries:

- *pyepw* used to read the typical meteorological year data
- *pvlib* to compute the incident irradiation

The coordinates of the studied site and orientation of the solar collectors must be specified to the model. Surface tilt angle is defined as degrees from horizontal (e.g. surface facing up = 0, surface facing horizon = 90). Surface azimuth angle is defined as degrees east of north (e.g. North = 0, South = 180, East = 90 and West = 270). The considered values are provided in Table 5.3.

These coordinates are used to define the characteristics of the location, and in particular to compute the solar time, the solar azimuth, the solar elevation and the angle of incidence of the beam radiation on a tilted surface.

Without tracking

If there is no sun tracking, the model determines total in-plane irradiance given total in-plane beam irradiance and total in-plane diffuse irradiance, in W/m^2:

$$I_{global} = I_{direct} + I_{diffuse} = DNI \cdot \cos(aoi) + (I_{d,g} + I_{d,s}) \tag{5.1}$$

where:

- the *Direct Normal Irradiation (DNI)* is provided by the Typical Metorological Year (TMY) data.
- the *Diffuse irradiance on the tilted surface reflected from the ground ($I_{d,g}$)* is calculated according [38].

  This is a function of the orientation of the PV panel (surface tilt angle - β), global horizontal irradiation (in W/m^2) and albedo (ground reflactance, typically 0.1-0,4

for land surfaces on Earth but may increase over snow, ice, etc.). An option to define surface type (urban, grass, snow, asphalt, concrete, etc.) is left to the user.

$$I_{d,g} = GHI \cdot albedo \cdot (1 - \cos\beta) * 0.5 \tag{5.2}$$

where GHI is the global horizontal radiation, provided in the TMY data.

– The *Diffuse component of solar radiation from the sky on a tilted surface ($I_{d,s}$)* is determined by the Klucher model [39]. It uses the PV panel orientation (surface tilt - β and azimuth - α angle), global and diffuse horizontal irradiation (in W/m^2) and sun position (zenith - θ_z and azimuth - θ_a angle).

$$I_{d,s} = DHI\frac{1+\cos\beta}{2}(1 + F'\sin^3(\beta/2))(1 + F'\cos^2\theta\sin^3\theta_z) \tag{5.3}$$

where:

$$F' = 1 - (I_{d0}/GHI) \tag{5.4}$$

and θ is the dot product of panel normal and solar angle:

$$\theta = \cos\beta \cdot \cos\theta_z + \sin\beta \cdot \sin\theta_z \cdot \cos(\theta_a - \alpha) \tag{5.5}$$

– The *Angle-of-incidence of the solar vector on the panel (aoi)* is function of the PV panel orientation (surface tilt - β and azimuth - α angle) and sun position (zenith - θ_z and azimuth - θ_a angle). It is calculated as the dot product of the solar vector and the surface normal by equation 5.5.

With tracking

If sun tracking is present, for a north-south axis collector global irradiance is computed given total in-plane beam irradiance, in W/m^2:

$$I_{global} = DNI \cdot \cos(aoi_{track}) \tag{5.6}$$

where:

– the *Direct Normal Irradiation (DNI)* is obtained from the TMY data.

– the *Angle-of-incidence of direct irradiance on the rotated panel surface (aoi_{track})* is function of the sun position equation (given by equation 11 in [40]) and of the panel normal vector given by a compass angle from tracker. Both are defined on panel-oriented coordinate system: y-axis is tracking axis at panel tilt; x-axis is orthogonal, clockwise, parallel to earth surface; z-axis is normal to x-y axes and points upward.

5.4 Modeling of generation systems

5.4.1 PV

PV generation depends on the temperature of the cells, which affects their efficiency. It is calculated according to [41] with a modified DNI to account for the latitude tilt. If

the system is equipped with PV panels and if the solar irradiation is higher than the cut-off below which technology is not responsive, the PV power generation is calculated by equation 5.7. Otherwise, there is no power generation.

$$P_{PV} = P_{nom,PV} \cdot \left(100 + (T_{cell} - 25) \cdot \frac{Tco_{Pmax}}{100}\right) \cdot I_b \tag{5.7}$$

where:

- T_{cell} is the cell temperature in relation to Nominal Operating Cell Temperature (NOCT) of the PV panel, beam irradiation I_b and ambient temperature T_{amb}, computed by:

$$T_{cell} = T_{amb} + (NOCT - 20) \cdot \frac{I_b}{800} \tag{5.8}$$

- Tco_{Pmax} is the temperature coefficient of rated power, $\%/C$
- I_b is the beam irradiation computed by a solar model (section 5.3).

5.4.2 ORC

The power output from the ORC mainly depends on the heat source (if there is a CSP installation, heat comes from TES; alternately, the ORC performs waste heat recovery from the backup generator) but also, as described in section 2.4.2, on the type of condenser that is being used (air- or water-flow). The ORC output power is computed in a different manner depending on the current case. These cases, which cover all possible system installations, are represented in a flow diagram in Figure 5.2 and are explained as follows (the boolean variables of the model are indicated in italic).

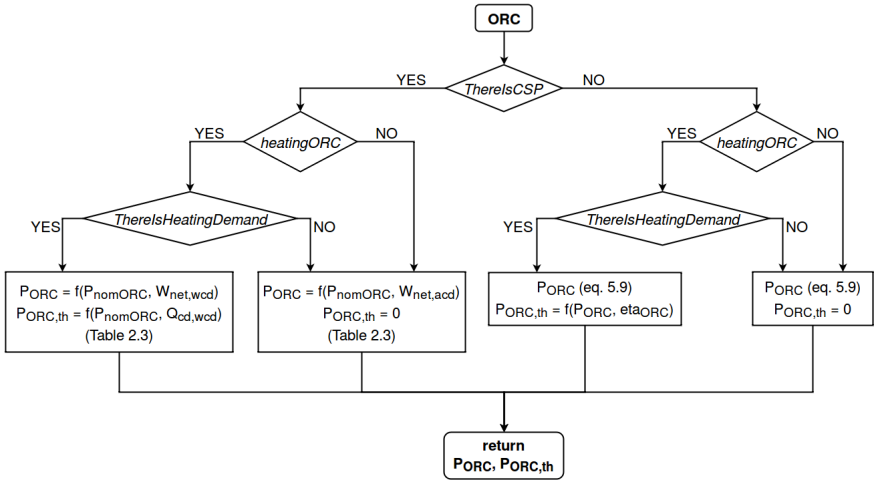

Figure 5.2: Flow diagram for ORC power generation computation

- Architecture 1: *ThereIsCSP* and *heatingORC*
  - Case 1: *ThereIsHeatingDemand*
    Because there is CSP, the TES is the heat source. *heatingORC* indicates that the ORC is the heating system (it acts as CHP), and, since there is heating demand, the water-flow condenser is used to provide the heat load. The ORC performance

(i.e. output power, cycle efficiency) is computed with the correlation developed in the case of a water condenser in section 2.23, Table 2.3.

- Case 2: not *ThereIsHeatingDemand*

  Because there is CSP, the TES is the heat source. The ORC is the heating system but there is no heat demand, therefore the air-flow condenser is used. The ORC performance (i.e. output power, cycle efficiency) is computed with the correlations using the air condenser from section 2.23 Table 2.3.

- Architecture 2: *ThereIsCSP* and not *heatingORC*

  There is CSP and the heating system is the TES (if the community has thermal demand) or there is no heating system (if the demand is zero). The TES is the heat source of the ORC and the air-flow condenser is used, since the heating demand is provided by TES. The ORC performance (i.e. output power, cycle efficiency) is computed with the correlations developed in the case of an air condenser in section 2.23, Table 2.3.

- Architecture 3: not *ThereIsCSP*

  Since there is no CSP installation, the ORC uses the thermal exhaust from the genset as heat source. The output power is based on a regression fitted from a detailed model in EES and is a function of ambient temperature and generator part load.

$$P_{ORC} = P_{genset} \cdot (d_0 + d_1 \cdot T_{amb}^2 + d_2 \cdot T_{amb}^3) \tag{5.9}$$

  The ambient temperature function coefficients are provided in Table 5.4.

5.4.3 LPG Generator: model and operation

The system features LPG-fuel generator as a backup for power generation. Ultimately, if there is insufficient power generation from renewable technologies, the generator must provide the balance of the load. Therefore, its nominal power is set equal to the peak load of the community.

The generator is only on when there is a residual load (RL) (i.e. PV is not supplying the entire load). In this case, the generator load is equal to the balance of demand after accounting for PV supply, taking into account any additional amount produced by the ORC (in the case where it is running). The possible cases are represented in the flow diagram in Figure 5.3, and explained hereafter.

- Case 1: *ThereIsCSP* or not *ThereIsORC*

  If there is CSP in the system, the ORC runs with the TES independently from the generator. Therefore, the generator load is computed by equation 5.10. If there is no ORC or if the ORC is not running, its output power is set to zero and thus the generator load is equal to the residual load.

$$P_{genset,load} = RL - P_{ORC} \tag{5.10}$$

- Case 2: not *ThereIsCSP* and *ThereIsORC*

  The ORC is always operating at the same time as the generator because, since there is no CSP-TES in the system, the ORC uses the thermal output from waste heat

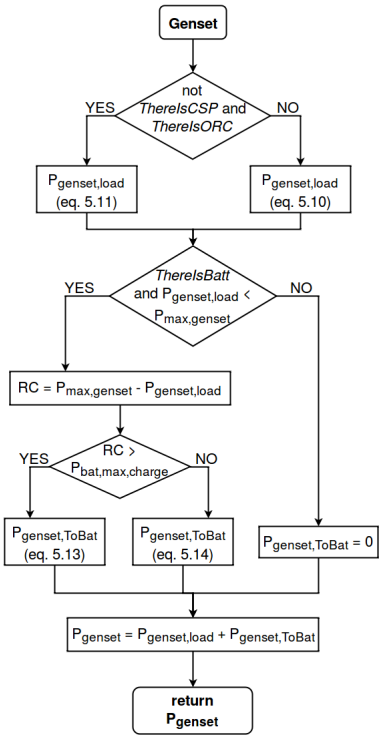

Figure 5.3: Flow diagram for genset power generation computation

recovery (WHR). The generator load is therefore lower than residual load because the ORC is also contributing. The required generator load is computed according to equation 5.11, which originates from the merging of equations 5.9 and 5.10.

$$P_{genset,load} = \frac{RL}{1 + f(T_{amb})} \tag{5.11}$$

Equations 5.10 and 5.11 set the generator output to the value of the unmet load (according to current demand). This load represents the minimum load the generator must supply. However, because the efficiency of LPG generators tend to drop abruptly in part-load operation, the generator load should be set to the highest possible value (i.e. ensuring no load is being dumped) and produce more than the load left. The generator remaining capacity (equation (5.12)) is therefore used to charge the batteries.

$$RC = P_{max,genset} - P_{genset,load} \tag{5.12}$$

As explained in section 5.5.1, the battery has a maximum capacity of charge per timestep, based on its characteristics and its SOC. The extra load that can be produced is limited to this value and depends on the other systems that are charging the batteries too. Thus, it is computed in terms of the following conditions (all possible cases covered):

– Condition 1: $RC > P_{bat,max,charge} - P_{ORC,ToBat}$

  If the residual capacity is higher than the batteries charge rate limit, the generator charges the battery to the limit.

$$P_{genset,ToBat} = P_{bat,max,charge} - P_{ORC,ToBat} \tag{5.13}$$

– Condition 2: $RC \leq P_{bat,max,charge} - P_{ORC,ToBat}$

Since the residual capacity is lower than the batteries charge rate limit, the generator charges the batteries up to its full residual capacity.

$$P_{genset,ToBat} = RC \tag{5.14}$$

Note that this is only applied when there is a bank of batteries. With no batteries in the system, the generator solely meets demand ($P_{genset,ToBat} = 0$).

The total generator load is the sum of the load serving the demand and the extra load charging the batteries (equation 5.15)

$$P_{genset} = P_{genset,load} + P_{genset,ToBat} \tag{5.15}$$

The genset fuel consumption is computed according to an efficiency curve extracted from its datasheet [42]

$$\eta_{genset} = \frac{P_{el}}{\dot{Q}_{LPG}} = \frac{P_{el}}{FR \cdot {}^{P_{max}}/_{\eta_{max}}} \tag{5.16}$$

where P_{el} is the generated power and $\dot{Q}_{LPG}$ is the combustion power of LPG. $\dot{Q}_{LPG}$ is calculated from the nominal combustion power using the fuel ratio, an empirical curve fitted from the manufacturer data:

$$FR = e_0 + e_1 \cdot partload + e_2 \cdot partload^2 \tag{5.17}$$

where $partload = {}^{P_{el}}/_{P_{max}}$. The empirical coefficients are provided in Table 5.4. According to [42], the maximum efficiency η_{max} is 19.87%, which is typical of small scale internal combustion based generator sets.

5.5 Modeling and control of storage units

5.5.1 Electrical energy storage: Batteries

When operating the battery, the key constraint is the maximum power that can be charged or discharged at every timestep. Its value is function of the SOC from the previous timestep $SOC_{bat}[h-1]$ and the charge/discharge power limit, a characteristic value of the batteries (variable $P_{max,bat}$). It is calculated according to:

$$P_{bat,max,charge} = min\left(\frac{E_{bat} \cdot 0.95 \cdot f_{soc} - SOC_{bat}[h-1]}{timestep}, P_{max,bat}\right) \tag{5.18}$$

$$P_{bat,max,discharge} = max\left(\frac{-SOC_{bat}[h-1]}{timestep}, -P_{max,bat}\right) \tag{5.19}$$

where f_{soc} is a factor to account for the effect of temperature on the capacity E_{bat} of the battery bank. It is calculated by:

$$f_{soc} = a_0 + a_1 \cdot T_{amb} + a_2 \cdot {T_{amb}}^2 \tag{5.20}$$

where a_i are empircal coefficients provided in Table 5.4. The value $E_{bat} \cdot 0.95 \cdot f_{soc}$ corresponds to the limit above which the batteries are considered full and cannot be charged anymore (initially 95% of their full capacity, adjusted according to temperature effects).

The lower bound under which the battery cannot be discharged is assumed to be 5% of its full capacity: $SOC_{LB,bat} = 0.05 \cdot E_{bat}$.

The possible charge/discharge mechanisms are accounted for in equation 5.21. A positive amount represents power flowing into the charge batteries (charging) and a negative amount represents power flowing out from the batteries (discharging).

$$P_{bat} = P_{PV,ToBat} + P_{ORC,ToBat} + P_{genset,ToBat} + P_{discharge} \tag{5.21}$$

Batteries cannot be charged/discharged beyond the available capacity (of each timestep) or the maximum charge/discharge power in a timestep (fixed value). The model checks all possible cases and corrects the balance if it is out-of-limits using the following conditions. These conditions have been represented in a flow diagram in Figure 5.4.

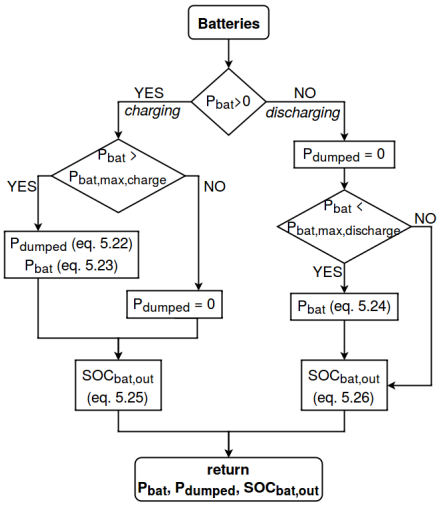

Figure 5.4: Flow diagram for battery energy balance

– Case 1: *charging*

  – Condition 1: $P_{bat} > P_{bat,max,charge}$
    There is more energy to charge batteries than the amount that can be charged. The maximum is charged and the rest is curtailed (here called *dumped*):

$$P_{dumped} = P_{bat} - P_{bat,max,charge} \tag{5.22}$$

$$P_{bat} = P_{bat,max,charge} \tag{5.23}$$

  – Condition 2: $P_{bat} \leq P_{bat,max,charge}$
    All charging powers can be delivered to the batteries. There is no curtailed generation.

– Case 2: *discharging* (note: the powers have negative values)

  – Condition 1: $P_{bat} < P_{bat,max,discharge}$
    The energy available from the batteries is less than the required amount to meet demand. The discharge is set to the maximum possible value and the rest is

provided by another system. This case is checked in the control loop each time the inverter is used in order to ensure that all the load is covered.

$$P_{bat} = P_{bat,max,discharge} \tag{5.24}$$

– Condition 2: $P_{bat} \geq P_{bat,max,discharge}$
All the energy needed can be sourced from the batteries and delivered by the inverter.

The batteries SOC is computed at the end of the timestep considering a 90% efficiency. For the charging:

$$SOC_{bat}[h] = SOC_{bat,in} + P_{bat} \cdot timestep \cdot 0.9 \tag{5.25}$$

and for the discharging:

$$SOC_{bat}[h] = SOC_{bat,in} + \frac{P_{bat} \cdot timestep}{0.9} \tag{5.26}$$

where $SOC_{bat,in}$ is the State-of-Charge of the batteries in the current timestep, having accounted for self-discharge.

5.5.2 Thermal energy storage: TES Tank

The thermal energy storage is a packed bed of quartzite in which the heat transfer fluid circulates - there is no phase change and only sensible storage of heat is considered. In order to simplify the model the TES tank is assumed to be at a uniform temperature. Although this differs from reality, it is considered acceptable since neglecting the stratification is a conservative approach.

The SOC of the TES is defined as a proxy for average tank temperature. It is considered that the maximum and minimum temperatures for which TES should be used as the ORC heat source are 180 and 150 ^{o}C respectively. While the maximum (i.e. upper bound UB) corresponds to 95% of TES full capacity, the minimum (i.e. medium bound MB) corresponds to the energy withdrawn in the TES by running the ORC during a timestep. However, the TES is not only used for the ORC heat source but also for heating. In order not to excessively discharge it, it is considered that it can supply heating until its temperature is 130^{o}C and not lower. It should be noted that producing space heating at this temperature implies a large exergy destruction, but this loss is deemed necessary to maintain the TES at a sufficient temperature to allow the ORC to run in the following time steps. The three temperature values (130, 150, 180) are then converted into a SOC value (in kWh) within the model. It is thus considered that the TES can be used for heating until the following SOC value is reached (i.e. lower bound LB):

$$SOC_{LB,TES} = 2 \cdot SOC_{MB,TES} - SOC_{UB,TES} = 2t \cdot \frac{P_{nom,ORC}}{0.1} - 0.95 \cdot E_{TES} \tag{5.27}$$

The TES SOC at a timestep is computed given the SOC of the previous timestep and accounting for thermal additions and losses (equation 5.28). The calculation is applied at the beginning of the timestep and accounts for the available energy in the TES.

$$SOC_{TES,in} = SOC_{TES}[h-1] + (P_{ToTES} - P_{TESloss}) \cdot timestep \tag{5.28}$$

Thermal additions in the TES can come from:

– *the CSP*: if there is enough irradiation, CSP power charges the TES. CSP generation is based on an efficiency law (fitted from a detailed EES model) function of the installed collectors surface A_{CSP}, the ambient temperature T_{amb}, the heat transfer fluid temperature $T_{htf,su,col}$ and the beam irradiation I_b. The law is provided in equation 5.29, with its coefficients presented in Table 5.4. It should be stated that CSP only generates power if the irradiation is higher than the technology cut-off, set to 100 W/m^2. If the TES temperature is above its operation maximum, collectors are defocused.

$$P_{CSP} = A_{CSP} \cdot I_b \cdot \left(b_0 + \frac{b_1 + b_2 \cdot T_{amb} + b_3 \cdot T_{htf,su,col}}{I_b} \right) \tag{5.29}$$

– *the generator*: if the generator is running, the thermal input from WHR is added to the TES. The WHR generated power is computed based on a power law fitted from a detailed model in EES. The law coefficients, which has the form of equation 5.30, are provided in Table 5.4. The main relevant variables influencing this power are the ambient temperature T_{amb}, the TES SOC SOC_{TES} and the TES full capacity E_{TES}. If the TES temperature is above its upper usable limit, WHR is not activated.

$$P_{WHR} = c_0 + c_1 \cdot T_{amb} + c_2 \cdot \frac{SOC_{TES}}{E_{TES}} + c_3 \cdot {T_{amb}}^2 \tag{5.30}$$

TES thermal losses are quantified as a function of the ambient temperature and the TES SOC (as a proxy for average tank temperature) extracted from a dataset applying the Schuman model (10-node) for a TES of up to 40 MWh [3].

The TES SOC at the end of the timestep (i.e. once the control strategy has dispatched the load) accounts for all possible discharges:

– Case 1: *thereIsORC* and *heatingTES*

Running ORC and/or serving heating demand reduces the SOC. Both can occur at the same time or separately.

$$SOC_{TES}[h] = SOC_{TES,in} - \frac{P_{ORC}}{\eta_{ORC}} \cdot timestep - P_{heating} \cdot timestep \tag{5.31}$$

– Case 2: *thereIsORC* and *heatingORC*

If the component tasked with supplying the thermal demand is the ORC and not the TES, the latter is only discharged by the ORC

$$SOC_{TES}[h] = SOC_{TES,in} - \frac{P_{ORC}}{\eta_{ORC}} \cdot timestep \tag{5.32}$$

5.5.3 Classification of the levels of storage

In order to implement easily understandable rules, a classification of the storage levels for each electrical and thermal storages is defined. The level depends on the SOC and on the upper and lower bounds characteristic of each type of storage (defined and explained in their section here above). The following states are defined for the batteries:

Table 5.4: Coefficient values of functions

	0	**1**	**2**	**3**
a	0.711	0.0139	-9.33 $\cdot 10^{-5}$	
b	0.734	6.94	0.252	-0.321
c	0.932	5.21$\cdot 10^{-3}$	-8.02$\cdot 10^{-2}$	-3.88
d	0.147	-2.25$\cdot 10^{-5}$	2.67$\cdot 10^{-7}$	
e	0.385	0.923	-0.308	

- if $SOC_{bat} \geq SOC_{UB,bat}$: 'full'
- if $SOC_{bat} \leq SOC_{LB,bat}$: 'empty'
- if $SOC_{LB,bat} < SOC_{bat} < SOC_{UB,bat}$: 'part charge'

and for the TES:

- if $SOC_{TES} \geq SOC_{UB,TES}$: 'too high'
- if $SOC_{TES} \leq SOC_{LB,TES}$: 'too low'
- if $SOC_{LB,TES} < SOC_{TES} \leq SOC_{MB,TES}$: 'low'
- if $SOC_{MB,TES} < SOC_{TES} < SOC_{UB,TES}$: 'high'

5.6 Control and regulation strategy

The micro-grid model dispatches the energy at each timestep depending on the installed devices and on the current demand. To define which devices to start-up/shut-down or keep in operation, a Rule Based Control is used. Control conditions (i.e. rules) depend mainly on the given system (which devices are installed), the current state (which devices are in operation), the levels of storage and the sun irradiation.

A flow diagram is presented in Figure 5.5 to illustrate the developed Rule Based Control. To describe the implemented control strategy, a state graph formalism is applied: each state corresponds to a particular combination of ON/OFF status of the different components, and some conditions are established for the transition from one state to the other. A state can vary from a timestep to the next one if the conditional statements differ. In a simplified example, the model can pass from using batteries to starting the generator in the next timestep if the batteries have been completely discharged.

However, it should be remarked that PV, which produces power depending on the sun and not because it is started-up/shut-down, is not explicitly represented among system states. The following explanation clarifies this statement.

The system state graph is presented in Figure 5.6. All possible transitions have been indicated by arrows. Each number on the arrows refers to a particular condition (described below), which must be satisfied for a state transition in that direction (if at least one of the conditions at an arrow is satisfied, the transition occurs). Four states are distinguished in the system:

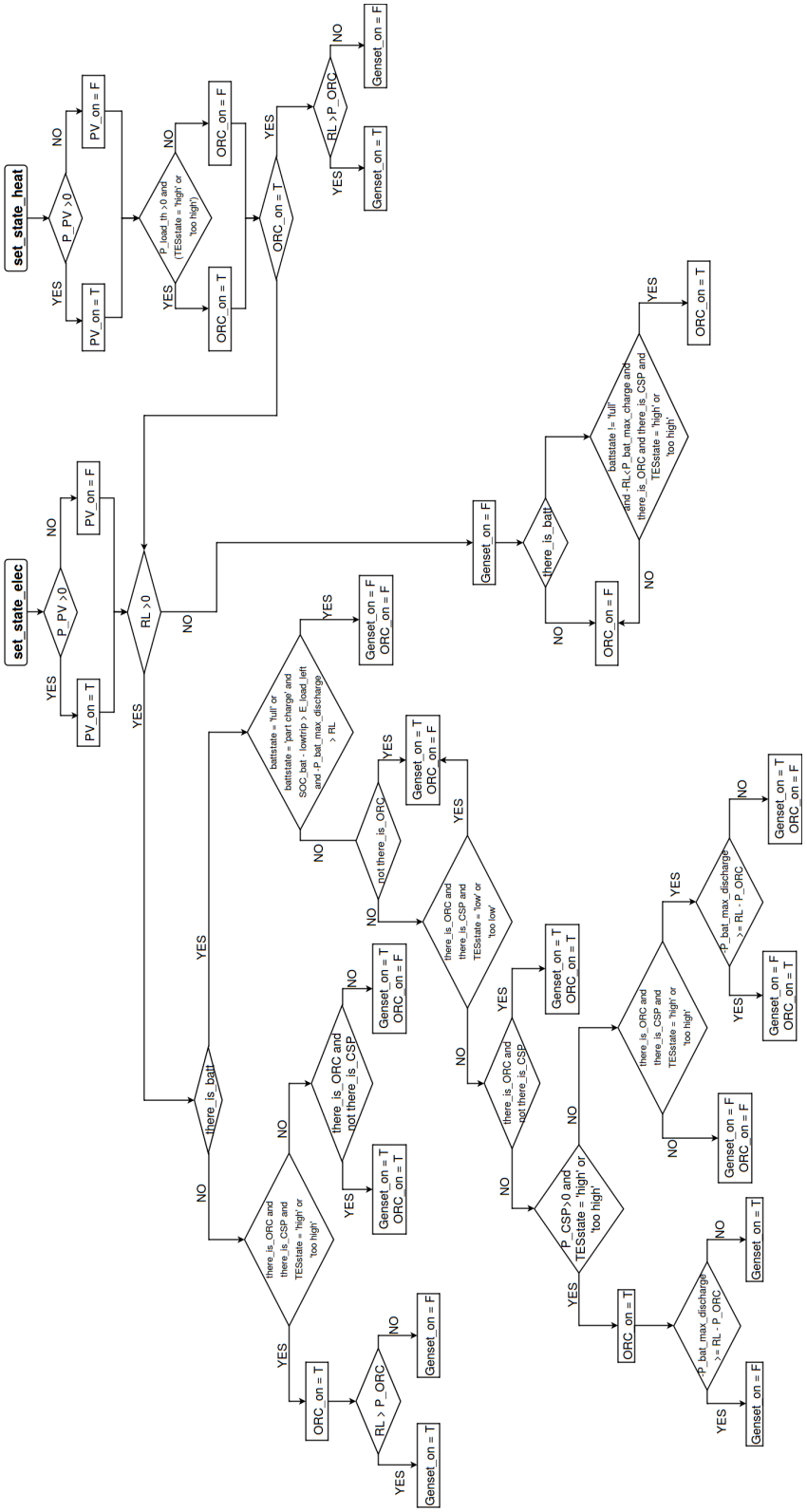

Figure 5.5: Flow diagram of the developed control strategy

– *ORC*: Only the ORC is running. This implies there is CSP-TES in the system.

– *GEN*: Only the generator is in operation. Two configurations are possible: (a) either there is no ORC in the system or (b) there is an ORC and CSP but TES is discharged below the minimum temperature required for ORC operation.

– *ORC + GEN*: Both ORC and generator are running. Two cases are possible: (a) there is no CSP, ORC is running with WHR from generator; (b) there is CSP and adequate charge in TES but ORC power output and battery SOC are insufficient to meet demand, invoking generator operatiion.

– *BAT*: Neither of ORC or backup generator are running. Residual load is supplied by the batteries or else there is no residual load.

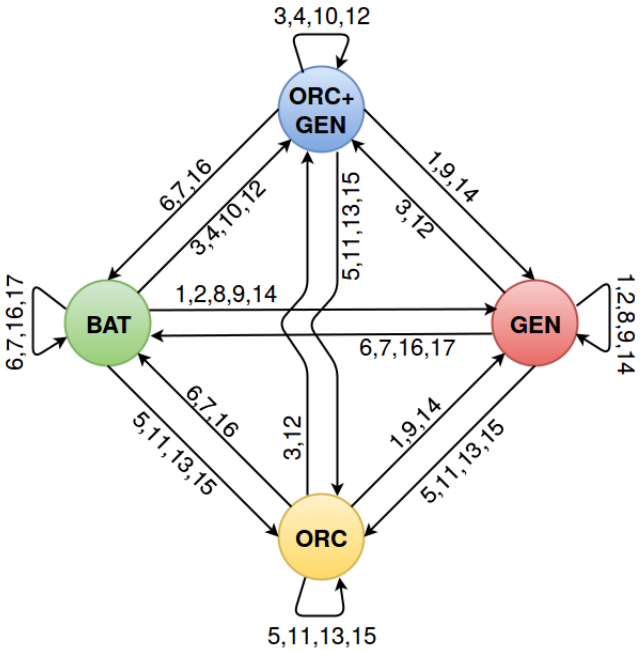

Figure 5.6: State graph of control

The control strategy accounts for all possibilities, i.e. 42 possible paths in the flow diagram (Figure 5.5), which have been synthesised in 17 conditions. These change-of-state conditions to be satisfied are the following:

1. $RL > 0$ and not *thereIsBatt* and *thereIsORC* and *thereIsCSP* and (TES_{state} = 'low' or 'too low')
2. $RL > 0$ and not *thereIsBatt* and not *thereIsORC*
3. $RL > 0$ and not *thereIsBatt* and *thereIsORC* and *thereIsCSP* and (TES_{state} = 'high' or 'too high') and RL > P_{ORC}
4. $RL > 0$ and not *thereIsBatt* and *thereIsORC* and not *thereIsCSP*
5. $RL > 0$ and not *thereIsBatt* and *thereIsORC* and *thereIsCSP* and (TES_{state} = 'high' or 'too high') and RL $\leq P_{ORC}$

6. $RL < 0$ and not *thereIsBatt*

7. $RL > 0$ and *thereIsBatt* and (bat_{state} = 'full' or bat_{state} = 'part charge' and $SOC_{bat} - SOC_{LB,bat} > E_{loadLeft}$) and $RL \leq -P_{bat,max,discharge}$

8. $RL > 0$ and *thereIsBatt* and (bat_{state} = 'empty' or bat_{state} = 'part charge' and $SOC_{bat} - SOC_{LB,bat} \leq E_{loadLeft}$) and not *thereIsORC*

9. $RL > 0$ and *thereIsBatt* and (bat_{state} = 'empty' or bat_{state} = 'part charge' and $SOC_{bat} - SOC_{LB,bat} \leq E_{loadLeft}$) and *thereIsORC* and *thereIsCSP* and (TES_{state} ='low' or TES_{state} = 'too low')

10. $RL > 0$ and *thereIsBatt* and (bat_{state} = 'empty' or bat_{state} = 'part charge' and $SOC_{bat} - SOC_{LB,bat} \leq E_{loadLeft}$) and *thereIsORC* and not *thereIsCSP*

11. $RL > 0$ and *thereIsBatt* and (bat_{state} = 'empty' or bat_{state} = 'part charge' and $SOC_{bat} - SOC_{LB,bat} \leq E_{loadLeft}$) and $P_{CSP} > 0$ and (TES_{state} = 'high' or 'too high') and $-P_{bat,max,discharge} \geq RL - P_{ORC}$

12. $RL > 0$ and *thereIsBatt* and (bat_{state} = 'empty' or bat_{state} = 'part charge' and $SOC_{bat} - SOC_{LB,bat} \leq E_{loadLeft}$) and $P_{CSP} > 0$ and (TES_{state} = 'high' or 'too high') and $-P_{bat,max,discharge} < RL - P_{ORC}$

13. $RL > 0$ and *thereIsBatt* and (bat_{state} = 'empty' or bat_{state} = 'part charge' and $SOC_{bat} - SOC_{LB,bat} \leq E_{loadLeft}$) and *thereIsORC* and *thereIsCSP* and (TES_{state} = 'high' or 'too high') and $-P_{bat,max,discharge} \geq (RL - P_{ORC})$

14. $RL > 0$ and *thereIsBatt* and (bat_{state} = 'empty' or bat_{state} = 'part charge' and $SOC_{bat} - SOC_{LB,bat} \leq E_{loadLeft}$) and thereIsORC and *thereIsCSP* and (TES_{state} ='high' or 'too high') and $-P_{bat,max,discharge} <$ (RL - P_{ORC})

15. $RL < 0$ and *thereIsBatt* and $bat_{state} \neq$ 'full' and $P_{PV,ToBat} < P_{bat,max,charge}$ and *thereIsORC* and *thereIsCSP* and (TES_{state} ='high' or 'too high')

16. $RL < 0$ and *thereIsBatt* and (bat_{state} = 'full' or $bat_{state} \neq$ 'full' and ($P_{PV,ToBat} \geq P_{bat,max,charge}$ or $P_{PV,ToBat} < P_{bat,max,charge}$ and *thereIsORC* and *thereIsCSP* and (TES_{state} = 'low' or 'too low')))

17. $RL < 0$ and not *thereIsORC*

It is worthwhile to note that all of the above conditions depend on the Residual Load (RL) variable. This variable is defined as the load minus the PV generation:

$$RL = P_{load} - P_{PV} \tag{5.33}$$

As shown in Figure 5.6, there is not a specific state for the PV installation. It is assumed that it is always ON, and the decision variable is the residual load: if positive, the model should to start-up some devices or use batteries to supply it. The dispatch is thus solely based on the presence or absence of residual load: as an example, the model takes the same decision for a night with no PV output and a 30kW demand as for a day with 20kW output of PV and a 50kW demand. This explains why the system states can be defined independently from PV.

A *smart* charging strategy is implemented for the batteries when they are charged from the generator at nights. For example, in the case where batteries are providing the nighttime loads, if they become fully discharged at some point the control module turns on the generator to supply demand, and to mitigate its low efficiency at part loads, it is also charging the batteries. In theory the generator could stand down once a nominal level of battery charge is reached, and in practice this SOC level should be high enough to avoid frequent start/stop cycles for the generator. In the extreme the generator could simply run until the SOC is full, but it would be inadvisable to use an expensively fueled generator in this way, because at dawn, if PV begins generating power in excess of demand while the battery SOC is full, PV generation must be curtailed and this has a negative impact on the investment returns. Once an initial PV investment is made, PV energy supplied to the loads or stored in a battery costs little in comparison to fossil fuel energy. Therefore, the control strategy operates the generator to charge the battery bank up to the point where the SOC of the bank is equal to the SOC sufficient to fulfilling the demand until dawn. This minimum state of charge is defined as $E_{loadLeft}$. Although, its values cannot be known a priori, it can be estimated from experimental data records provided by [3].

CHP systems can be electricity-driven (the unit supplies the electrial load and heat is a by-product) or heat driven (the unit supplies the heat demand and the power is a by-product). The same distinction is performed for the control of the ORC unit: it is electricity-driven when the following system configurations are present:

– Configuration 1: *heatingTES*

  In that case, heating is provided directly by the TES tank. The ORC therefore only starts if there is a demand for electricity and if there is sufficient heat source availability. This availability is computed as the remaining energy in the TES, as indicated in equation 5.34.

$$P_{TES,max} = \frac{(SOC_{TES} - E_{LowerLimit})}{timestep} \tag{5.34}$$

  A residual thermal load is also defined as:

$$RL_{th} = P_{load,th} - P_{TES,max} \tag{5.35}$$

  Three cases are possible:

  – Case 1: $P_{load,th} > 0$ and $TES_{state} \neq$ 'too low' and $reisudalLoad_{th} > 0$
    TES charge is adequate to meet some of demand but not sufficient to meet all of demand. The backup burner is used to provide the remaining heat demand (RL_{th}).

$$P_{heating} = P_{TES,max} \tag{5.36}$$

$$P_{backupBurner} = RL_{th} \tag{5.37}$$

  – Case 2: $P_{load,th} > 0$ and $TES_{state} \neq$ 'too low' and $reisudalLoad_{th} \leq 0$
    TES charge is adequate and sufficient.

$$P_{heating} = P_{load,th} \tag{5.38}$$

$$P_{backupBurner} = 0 \tag{5.39}$$

- Case 3: $P_{load,th} > 0$ and TES_{state} = 'too low'
  The charge of the TES is too low. All loads must be provided by the backup system.

$$P_{heating} = 0 \tag{5.40}$$

$$P_{backupBurner} = P_{load,th} \tag{5.41}$$

- Configuration 2: *heatingORC* and not *thereIsCSP*

  In this case, heating is provided by the ORC, which operates with the WHR from the genset exhaust (i.e. there is no CSP-TES in system). The residual thermal load is given by:

$$RL_{th} = P_{load,th} - P_{ORC,th} \tag{5.42}$$

  Again, three cases are possible:

  - Case 1: $P_{load,th} > 0$ and *ORCisON* and $RL_{th} > 0$
    The ORC is running and producing thermal power but not as much as demanded.

$$P_{heating} = P_{ORC,th} \tag{5.43}$$

$$P_{backupBurner} = RL_{th} \tag{5.44}$$

  - Case 2: $P_{load,th} > 0$ and *ORCisON* and $RL_{th} \leq 0$
    The ORC is running and covers the full thermal demand.

$$P_{heating} = P_{load,th} \tag{5.45}$$

$$P_{backupBurner} = RL_{th} \tag{5.46}$$

  - Case 3: $P_{load,th} > 0$ and not *ORCisON*
    Since control is electricity driven, it may occur that the ORC is not running. In that case, all the thermal loads must be provided by the backup system.

$$P_{heating} = 0 \tag{5.47}$$

$$P_{backupBurner} = P_{load,th} \tag{5.48}$$

- Configuration 3: *heatingORC* and *thereIsCSP* and $P_{load,th} = 0$

  Heating is provided by the ORC, which is operated from the TES tank but there is no heating demand at the moment. No heat must be provided.

If heating is provided by the ORC and there is CSP-TES in the system, unless there is no heating demand (Configuration 3 here above), the control should be heat driven. That is, the system must decide to run the ORC if there is thermal demand, so that the latter is supplied by the ORC condenser and not by a more costly backup system.

Given CSP power and TES conditions, ORC potential electrical and thermal output powers must be computed. Given a residual load by equation 5.42, the following cases can occur:

- Case 1: TES_{state} = 'high' or 'too high' and $RL_{th} > 0$

  There is adequate charge in TES to run the ORC but its thermal potential is lower than the demand. Backup burner must be used as well (equations 5.43 and 5.44). The model decides to run the ORC:

$$ORC \Rightarrow ON \tag{5.49}$$

– Case 2: TES_{state} = 'high' or 'too high' and $RL_{th} \leq 0$

There is adequate charge in the TES to run the ORC and its thermal potential is equal or higher to the demand (equations 5.45 and 5.46). Some thermal load is curtailed. The model decides to run the ORC:

$$ORC \Rightarrow ON \tag{5.50}$$

– Case 3: TES_{state} = 'low' or 'too low'

The SOC of the thermal storage is not sufficient to run the ORC. All thermal loads must be produced with a backup burner (equations 5.47 and 5.48).

$$ORC \Rightarrow OFF \Rightarrow elecDrivenControl \tag{5.51}$$

Therefore, the heat-driven control defines the ORC state (ON/OFF). If the model decides to run the ORC, the following control consists of checking whether there is residual electrical load remaining, and if so, use the generator to provide it.

On the contrary, if the heat-driven control decides not to run ORC, the following step is to run an electricity-driven control, as stated in equation 5.51. This means, even if thermal demand production does not indicate ORC operation, it may occur that electrical demand provides the need.

Figures 5.7 and 5.8 provide a dispatch plot for two equal microgrid system configurations. The former uses the ORC as the heating system. The control strategy applied in Figure 5.7 is thus heat driven. It can be seen that the model decides to run the ORC during the day (red surface in Figure 5.7a) in order to provide the heating demand (black line in Figure 5.7b), even if PV (blue surface in Figure 5.7a) is already providing more than the load. On the other hand, Figure 5.8 uses the TES as the heating system and the control is thus electricity driven. Comparing Figure 5.7a to 5.8a, it can be seen that not only the ORC is less used in the latter but it is also preferably used during the night.

The *smart* control strategy for the batteries is also shown in both Figures 5.7a and 5.8a. Unlike during daylight, the generator is being used constantly until the SOC of the battery (values at the right axis of the Figures) reaches the predicted value of charge that is commensurate with expected demand until dawn. Once the batteries SOC reaches the threshold, the generator is stopped and the battery is used to provide the load. As expected, at dawn, the SOC of the batteries is almost 0.

5.7 Fuel consumption

The total fuel consumption is related to the backup generator and the burner. The burner is assumed to work with a 95% of efficiency on the LHV, even for part-load operation. The backup generator performance is computed according to section 5.4.3. Total fuel consumption is thus computed according to the following:

$$m_{propane} = \frac{(\dot{Q}_{fuel,burner} + \dot{Q}_{fuel,genset}) \cdot t}{LHV_{fuel}} \tag{5.52}$$

where t is the timestep expressed in seconds and $LHV_{fuel} = 46 \cdot 10^3$ kJ/kg.

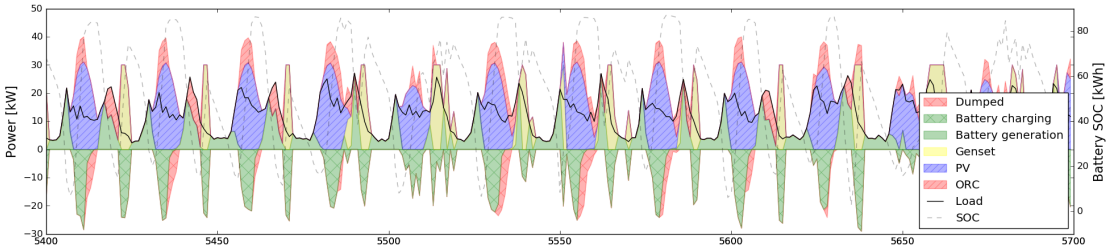

(a) Electrical power dispatch

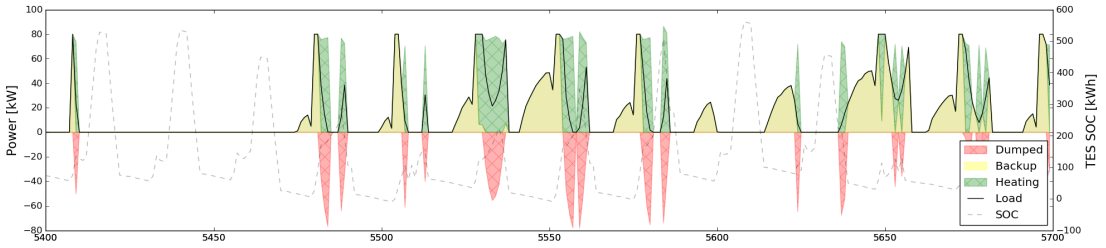

(b) Heating power dispatch, provided by the ORC

Figure 5.7: Dispatch plot of (a) electricity and (b) heat to illustrate the heat driven regulation

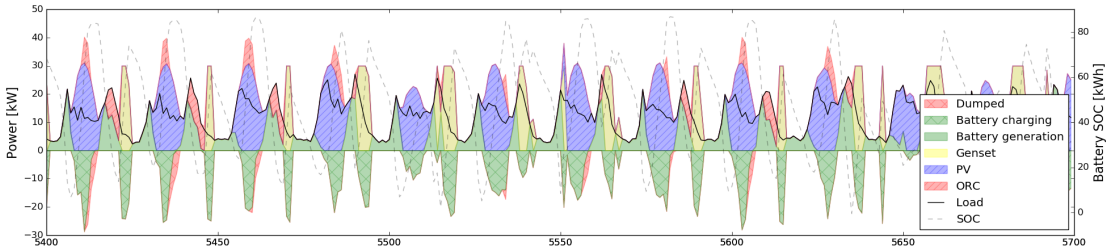

(a) Electrical power dispatch

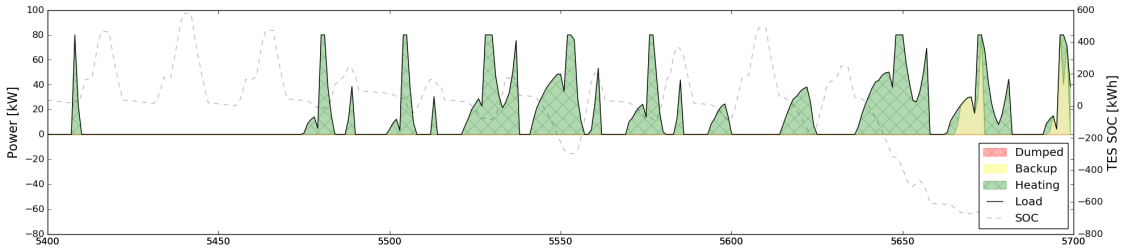

(b) Heating power dispatch, provided by the TES

Figure 5.8: Dispatch plot of (a) electricity and (b) heat to illustrate the electrical driven regulation

5.8 Economic model

The micro-grid is based on a fee for service (i.e. prepaid smart meter) business model with positive cash flow and returns to debt capital for the power producer, which can be either

the government or the private sector [36]. Moreover, the level of service at the household connections must be comparable to similar communities that are being served by the grid.

The economic model accounts for initial capital, maintenance and operation costs, as well as for replacement cost of each component (in particular the batteries). Transmission and distribution lines, smart metering devices and ICT solutions for money transaction are also accounted for in the calculation of the tariff [36].

All economic inputs related to the project, the community of interest and the cost functions components are presented and described in Table 5.5. The cost of each generator and chemical battery storage is computed according to the following:

$$C_{batt}[USD] = c_{batt} \cdot E_{batt} \tag{5.53}$$

$$C_{CSP}[USD] = A_{CSP} \cdot c_{collector} + P_{nom,ORC} \cdot c_{ORC} + E_{TES} \cdot c_{TES} \tag{5.54}$$

$$C_{LPG}[USD] = -10354.1143 + 6192.606 \cdot ln(peakload) \tag{5.55}$$

$$C_{PV}[USD] = c_{panels} \cdot P_{nom,PV} + c_{inv} \cdot P_{peak} + C_{control} + C_{dist} + c_{SM} \cdot n_{nodes} + c_{MPesa} \cdot P_{peak} \tag{5.56}$$

where

$$C_{dist} = c_{d,wire} \cdot d + c_{stepUpTrans} \cdot n_{stepUpTrans} + c_{poleTrans} \cdot n_{poleTrans} + c_{pole} \cdot n_{poles} \tag{5.57}$$

Propane cost per year is computed according to the following:

$$C_{propane/y}[USD] = c_{propane} \cdot m_{propane} \tag{5.58}$$

Maintenance costs for each year of the project are computed according to equation 5.59. Factors for distributing maintenance costs in time as a function of *capex* are provided in Table 5.6.

$$\begin{aligned} M = \sum_{y=1}^{LT+1} [& f_{PV} \cdot a_{PV} \cdot \frac{C_{pv}}{LT} + f_{PV} \cdot (1 - a_{PV}) \cdot \frac{C_{pv}}{LT^2} \cdot (2y - 1) \\ & + f \cdot a \cdot \frac{C_{lpg}}{LT} + f \cdot (1 - a) \cdot \frac{C_{lpg}}{LT^2} \cdot (2y - 1) \\ & + f \cdot a \cdot \frac{C_{csp}}{LT} + f \cdot (1 - a) \cdot \frac{C_{csp}}{LT^2} \cdot (2y - 1)] \end{aligned} \tag{5.59}$$

Operating costs include the fuel consumption from the backup generator (equation 5.58). Initial investments costs aggregate the costs of CSP, LPG and PV (equations 5.54 to 5.56). Battery investment costs (equation 5.53) are accounted for initially and at every bank replacement, which takes place when batteries have reached their maximum number of discharge cycles. With the maintenance, operating and investment costs defined, the Levelized Cost Of Electricity can be computed according to the following:

$$LCOE = \frac{\sum_{y=1}^{LT} \frac{M_y + O_y + I_y}{(1+r)^y}}{\sum_{y=1}^{LT} \frac{E_y}{(1+r)^y}} \tag{5.60}$$

Because thermal demand is also supplied by the micro-grid, a Levelized Cost Of Energy (electrical+thermal) is computed to take into account both electrical and thermal loads. Equation 5.60 is used, with the burner now taken into account in both operating O_y and investment I_y costs, and the thermal load added to the annual load E_y.

Table 5.5: Economic Inputs (provided by [3])

	Parameter	Description	Value	Units
Project	LT	Lifetime	15	years
	r	Interest Rate	0.05	
	n_{bat}	Battery life cycle	1750	times
Community	n_{nodes}	Number of network connections	90	con/m
	d	Distance	5	km
	$n_{stepUpTrans}$	Number of step up transformers	1	transf
	$n_{poleTrans}$	Number of transformers	3	transf
	n_{poles}	Pole-to-pole distance	50	m/pole
Costs	$c_{d,wire}$	Wire cost per distance	0.5	USD/m
	c_{batt}	Batteries cost per capacity	130	USD/kWh
	c_{panels}	Panels cost per nominal power	1000	USD/kW
	$C_{control}$	Control cost	5000	USD
	c_{pole}	Transmission pole price	40	USD/pole
	$c_{poleTrans}$	Transformer price	150	USD/transf
	$c_{stepUpTrans}$	Step up transformer price	1000	USD/transf
	c_{SM}	Iometer (smart meter)	50	USD/(con/m)
	c_{MPesa}	Merchant services per peak load	70	USD/kW
	c_{inv}	Inverter cost per peak load	800	USD/kW
	$c_{propane}$	Propane cost per mass	1.24	USD/kg
	$c_{collector}$	Parabolic trough collectors cost	150	USD/m^2
	c_{ORC}	ORC cost	2000	USD/kW
	c_{TES}	TES cost	25	USD/kWh

Table 5.6: Factors for distributing maintenance costs in time

Factor	Value
f_{PV}	0.25
a_{PV}	0.25
f	1.25
a	0.25

5.9 Simulation of the microgrid model

5.9.1 Evaluation of the microgrid improvement linked to the high expansion ratio scroll expander

In Chapter 2, it is demonstrated that the ORC with a higher expansion ratio scroll expander presents better performance than with a low expansion ratio scroll expander (adapted from a scroll compressor). Using a higher performance ORC can lead the micro-grid model to select a different optimal solution. The purpose of this section is to quantify the impact of this improvement on the micro-grid. To that end, two different simulations are performed:

- *Simulation 1*: micro-grid composed of CSP, TES, ORC (3-15 kW), a backup generator and a burner
- *Simulation 2*: micro-grid composed of CSP, TES, ORC (15-30 kW), batteries and a backup generator and burner

Both micro-grid configurations use the ORC as the main generator (there is no PV), with TES as the heat source. The use of the TES is required to mitigate CSP intermittence. It can accumulate thermal energy originating from the PTC or the WHR from the backup generator. Model inputs of each simulation are adapted to the corresponding ORC nominal power in order to provide adequate CSP power and TES and/or batteries capacity.

Simulation 1

The simulation is performed on a range of nominal powers of the ORC. Because the configuration does not include battery storage, the ORC nominal power must be small enough to avoid energy curtailment. Curtailment happens when the energy provided by a generator is higher than the demand. The higher the ORC nominal power, the more it produces and thus the more curtailed energy if no battery storage is present. Thus, the simulated range of ORC nominal powers is from 3 to 15 kW.

To evaluate the results, the values of the LCOE and the fuel consumption are studied. The ORC using the high and low expansion ratio scroll expander is referred to as *HRE* and *LRE*, respectively. As expected, LCOE (Figure 5.9a) is lower for HRE than for LRE. It should be noticed that the smaller the ORC (e.g. 3kW), the smaller the difference between one configuration or the other. However, for nominal powers around 15kW, LCOE for HRE can be up to 11.4% lower than for LRE. The difference is considerable and could impact the decision of whether or not to install an ORC.

It should be noted that the LCOE values are relatively high. This is due to the low efficiency of the genset, the high fuel costs in mountainous areas, the fact that the sizing of the components is imposed and not optimized, and a non-optimal control strategy.

Fuel consumption is also lower for HRE. This is explained because of the reduced use of the backup generator due to the higher ORC output than for LRE. Because in this simulation heating is provided by TES, the decrease in fuel consumption is also influenced by the higher TES capacity for larger ORCs.

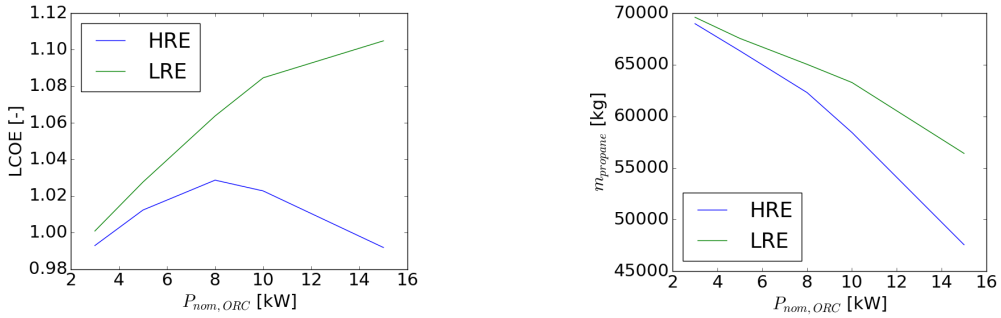

(a) Levelized Cost Of Electricity

(b) Consumed mass of propane

Figure 5.9: Micro-grid outputs comparison when the ORC uses high (HRE) or low (LRE) expansion ratio scroll expanders

Simulation 2

When the ORC output is higher than the demand, some generation must be curtailed. This usually happens at noon, when CSP power is available but electrical demand is considerably low (peaks are encountered in the evenings or early in the mornings). Therefore, a solution consists in using low-capacity ORCs units, as done above. However, ORCs with higher nominal powers can also be used if coupled with battery storage. This simulation studies this particular case.

Batteries are charged with the excess power of the ORC or with the power from the backup generator, which works at the maximal possible load. The selected range of ORC nominal powers is from 15 (where, given the demand, curtailment appear) to 35 kW (peak load of the demand).

As expected, results present a lower LCOE for the HRE case. The LCOE difference between LRE and HRE is similar through the range of nominal powers, with a maximum of 7.32%.

Fuel consumption decreases for higher nominal powers because of the reduced use of the backup generator, as a consequence of a higher ORC output. For the same reason, fuel consumption is lower for HRE than for LRE. Similarly to the above, because in this simulation heating is provided by the TES, the decrease in propane consumption is also influenced by the increase of the TES capacity for larger ORCs.

5.9.2 Comparison of microgrid performance using two different type of heating systems: TES or ORC

The micro-grid configuration (Figure 5.1) presents two type of heating systems: the TES (heating comes directly from the thermal storage) and the ORC (heat is recovered at the condenser level). In Chapter 2, a model of an ORC that offers the possibility of using either an air- or a water-flow condenser is developed. The goal is to use the water type, when there is thermal demand, and the air type when there is no heating demand. TES is the power source of the ORC, but it can also provide heating directly from the tank, as shown in Figure 5.1). The main goal of this simulation is to compare micro-grid feasibility

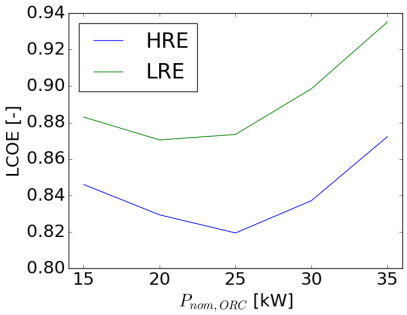

(a) Levelized Cost Of Electricity

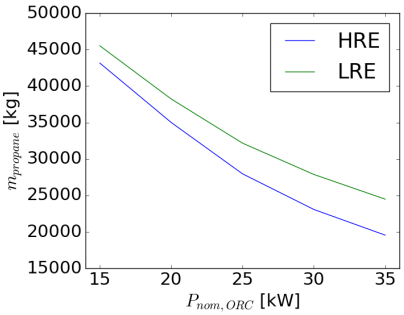

(b) Consumed mass of propane

Figure 5.10: Micro-grid outputs comparison when the ORC uses high (HRE) or low (LRE) expansion ratio scroll expanders

Table 5.7: Model inputs

	Value	Units
timestep	1	h
NOCT	45	ºC
latitude	-29	º
longitude	28	º
$P_{max,load}$	30	kW
E_{bat}	190	kWh
$P_{nom,PV}$	30	kW
A_{CSP}	860	m^2
$P_{nom,ORC}$	10	kW
E_{TES}	1200	kWh

with one configuration or the other. One simulation for each is performed, with the same inputs for both (Table 5.7).

Simulation results for a period of 300h in June are presented in Figures 5.11a and 5.11b. An ORC with a nominal power of 10kW produces approximatively a nominal thermal power of 80kW. However, the demand is only of 80kW during the peak in the morning (refer to Chapter 4), being lower during the rest of the day. This implies a high amount of curtailed thermal power from the ORC, as it can be seen in Figure 5.11b (in red, called *dumped*, equal to the green zone above the load line). Moreover, the ORC can only run when the TES charge is adequate. For example, the TES SOC (dashed grey line, axis at the right) at the timestep 4800h, is close to zero. Thus, the ORC cannot be operated and the load must be provided by the backup burner (yellow).

In contrast, the TES can supply the exact amount of load that is required. As it is shown in Figure 5.11a, there is no curtailed (*dumped*) energy, i.e. the heating power is always exactly equal to the load. Moreover, the TES can be used down to 130ºC to provide heating, whereas a minimum of 150ºC is needed to run the ORC. This can be seen when looking at the axis values of the TES SOC, which as previously stated, is defined as a proxy for average tank temperature (i.e. $1200kWh \Leftrightarrow 180$ºC, $10kWh \Leftrightarrow 150$ºC, $-1200kWh \Leftrightarrow 130$ºC).

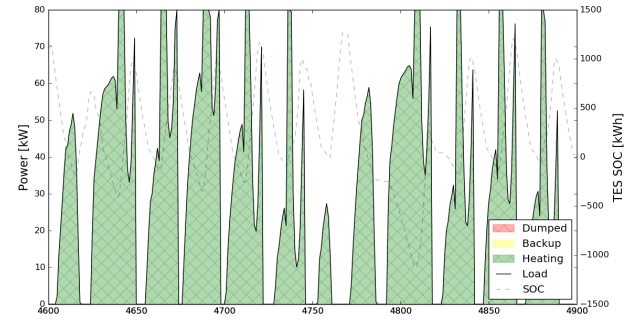

(a) Heating provided by TES

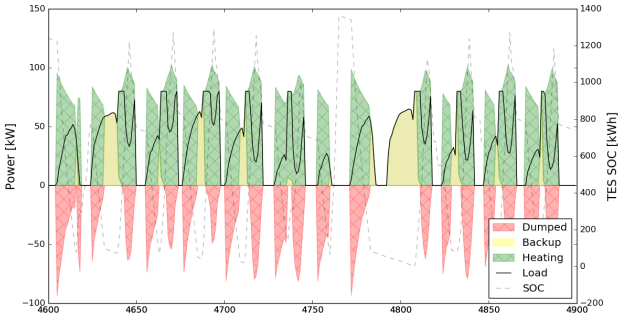

(b) Heating provided by ORC

Figure 5.11: Micro-grid heating dispatching for two different configurations

Because of the large amount of wasted energy in the ORC case, the backup burner is used more frequently and the annual fuel consumption is higher: 8049 kg vs 5882 kg in the case of the TES heating. Therefore, although in theory cogeneration is beneficial for the efficiency of the system, it is not the case in the present simulation. A possible solution would be to install hot water storage tank after the condenser of the ORC, to absorb the large quantities of heat when it is in operation. The main quantities from the simulation results are provided in Table 5.8.

5.10 Sizing optimization

5.10.1 Objective function and parametrization

The first step towards the design of a viable energy system is to technically specify and size a combination of different power sources. However, the system must also be economically feasible. Thus, the optimum configuration of the system should be determined based on a financial analysis (e.g. minimizing Levelized Cost of Energy (LCOE), maximizing Internal Rate of Return (IRR), etc.). Therefore, a cash flow model is coupled to the technical-dispatching model. The main goal of the design optimization is to find the system infrastructure and the optimum power flow control strategy that achieves the minimum tariff (USD/kWh) to consumers. The tariff is based on cost recovery of the capital and operating costs.

Table 5.8: Optimization for a microgrid configuration using two different type of heating systems: TES or ORC

	Config 1	**Config 2**
heating system	TES	ORC
LCOE [USD/kWh]	**0.534**	**0.549**
LCOE$_{ThEl}$ [USD/kWh]	**0.334**	**0.351**
Total propane consumption [kg]	**5655**	**8049**
Total load [kWh]	**97041**	**97041**
Total PV generation [kWh]	57031	57031
Total ORC generation [kWh]	34877	34920
Total Genset generation [kWh]	14640	16543
Total thermal load [kWh]	**58745**	**58745**
Total heating system generation [kWh]	57345	111433
Total burner generation [kWh]	1401	13569

The problem is a non-linear optimization problem without integer variables. At each evaluation, the solver must simulate a full year of operation, compute all the yearly energy flow, and deduce the levelized cost of energy (LCOE), which is the variable to be optimized.

5.10.2 Optimization technique

There are several types of optimization techniques that can be used to determine the optimum solution of a complex (non-necessarily convex) non-linear problem. Because population-based algorithms present the advantage of being simple and relatively easy to implement, they are well suited to solve this type of problems. Amongst this technique, genetic algorithm (GA) and particle swarm optimization (PSO) have already been studied for practical applications in the energy systems field, for example in [43] and [44]. This last study performed a comparison between PSO and GA applied to an off-grid energy system. Results presented better CPU utilization time and lower number of iterations for PSO [44].

An alternative to population-based algorithms is the use of gradient methods or of the well-known Nelder-Mead algorithm. However, this optimization method does not easily handle constraints and variable boundaries. In this particular optimization, this is a decisive issue since the micro-grid model does not provide valid results with negative installed component capacities for example. With the PSO algorithm, it is straightforward to set lower and upper boundaries of the search-space, which is a significant advantage.

Based on the above analysis and on the study performed in [37], PSO is selected as the algorithm to run the micro-grid optimization.

PSO is a population-based optimization technique that invokes natural behavior of particles, inspired by social behavior of bird flocking or fish schooling [45]. The algorithm, first introduced by [46], has been proved to be efficient in solving multidimensional non-linear problems [44]. Every possible solution corresponds to a particle position in an n-dimensional search space. The algorithm first starts with a random population within the possible search space. The initial populations are updated in each iteration with the purpose of finding the optimal solution. The update is influenced by the particle previous

Table 5.9: Optimization parameters

Parameters	**Description**	**Value**
swarmsize	Number of individuals	20
maxiter	Maximum number of generations	50
omega	Momentum	0.95
minfunc	Acceptable change on tariff to stop	$1{\cdot}10^{-5}$

positions and the neighbors previous positions (personal and global experience, respectively) [37].

The PSO optimization has been implemented in Python, with the use of the library *Pyswarm*. Parameters selection is done according to the evaluation and selection study performed in [37]. Values are presented in Table 5.9.

5.11 Optimization results

The optimization results that sizes the described microgrid system are evaluated in 5.11.1. However, two other simulations are also performed to evaluate the size of the system if other costs were presented or more restrictive possible configurations were offered to the model.

5.11.1 Simulation 1: Optimal sizing

The obtained sizing results are presented in Table 5.10. Interestingly, the model only chooses to install PV and batteries, because of their lower costs compared to thermal technologies (costs in Table 5.5). Moreover, although the heating system is set to be the TES, the optimization shows that it is preferable not to install CSP and TES and produce all the thermal load with the backup burner.

Figure 5.12 shows part of the power dispatch in May. The electrical peak load usually occurs in the mornings and the evenings, with the lowest values during the night. The model selected the optimum size of PV panels that not only provides the load during daylight but also charges the batteries at its maximum (batteries SOC is indicated at the right axis). Therefore, it is almost ensured that the batteries provide all of the load during the night and the backup generator is almost never used. However, in some days when the irradiation is lower (3rd blue peak in the Figure), the batteries cannot supply the entire load and the generator is turned on.

5.11.2 Simulation 2: System with no PV

Because the results of section 5.11.1 selected PV as the most important power source, an optimization with no PV allowed in the system is performed. The main goal is to see the flow distribution between the systems when no PV panels are installed. Because unlike in 5.11.1, in this simulation the system is likely to choose an ORC, the heating is chosen to be provided by the latter. The optimal system configuration and the corresponding tariff are presented in Table 5.10.

Figure 5.13 shows the power dispatch for a period of 4 days in July. The days with more diffuse irradiation (e.g. first peak in the Figure) present higher generator consumption than

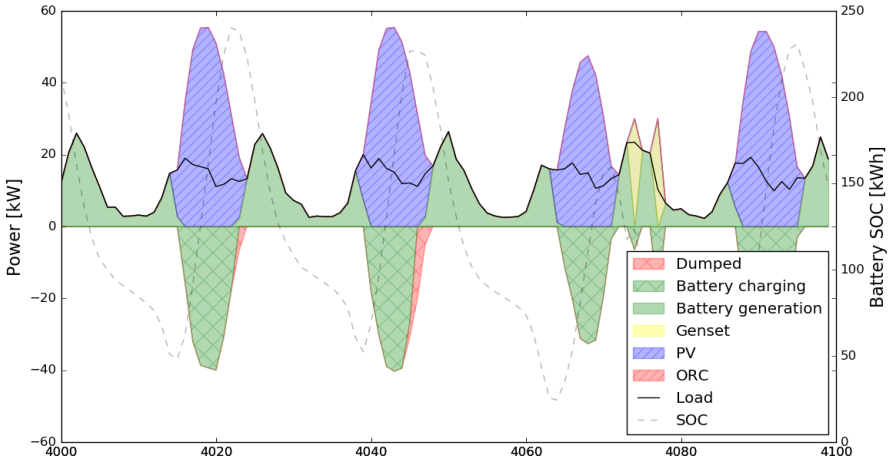

Figure 5.12: Power dispatch for Simulation 1

the others. Because of the load profile, the higher values of load experienced around noon induce the model to delay using the ORC. Instead, the control module saves the thermal energy stored in TES to be used later during the night. Although this approach does not create a high impact on this simulation, the main idea is to save the TES for the night (when the generator is usually needed) because PV should already be producing all the load during the day. However, the model also decides to run the ORC in some occasions during the day (e.g. for hour 58420, 58550, etc. in the Figure). This decision corresponds to rule 11 of the control strategy.

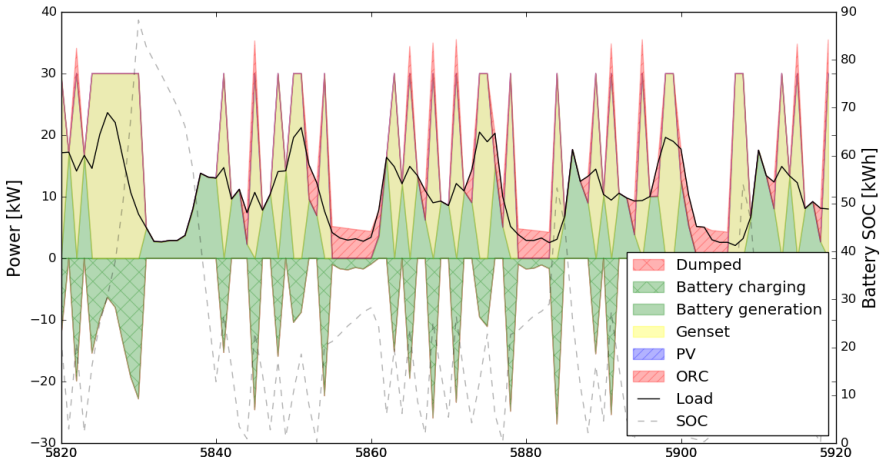

Figure 5.13: Power dispatch for simulation 2

The values shown in Table 5.10 show that installing PV is recommended for such a microgrid system. The LCOE and the fuel consumption values are much higher than the ones obtained in the first simulation. Moreover, the fact that the ORC is only running a few hours every day implies a higher burner generation. Another adverse effect is that

the ORC runs mostly during the night, while thermal demand from the clinic and load is important during the working hours of the building. It should be noted that if the control strategy was optimized for a microgrid with no PV, the ORC would run more often during the day, which could improve the results. However, it is not expected that overall performance would be significantly impacted.

5.11.3 Simulation 3: Modified investment costs

The model decision is highly influenced by the costs relative to each subcomponent, as already presented in Table 5.5. In the current economic inputs, PV and batteries are more cost-effective than the ORC. The main goal of this simulation is thus to see if the model would invest in ORC capacity with more favorable investment costs. The price of PV and batteries is increased, while the price of the ORC is decreased. The CSP and TES prices are kept unchanged. The new prices used in this simulation are presented in Table 5.11, together with the original ones for the sake of comparison.

The obtained results are shown in Table 5.10. Differently than in 5.11.1, the simulation chooses to install an ORC, CSP and TES. However, even with the proposed decrease in ORC cost, the optimum system still relies mostly on PV power generation and battery storage. The optimal ORC power is 3.5kW, and as it can be seen in Figure 5.14, it does not influence much the power dispatch.

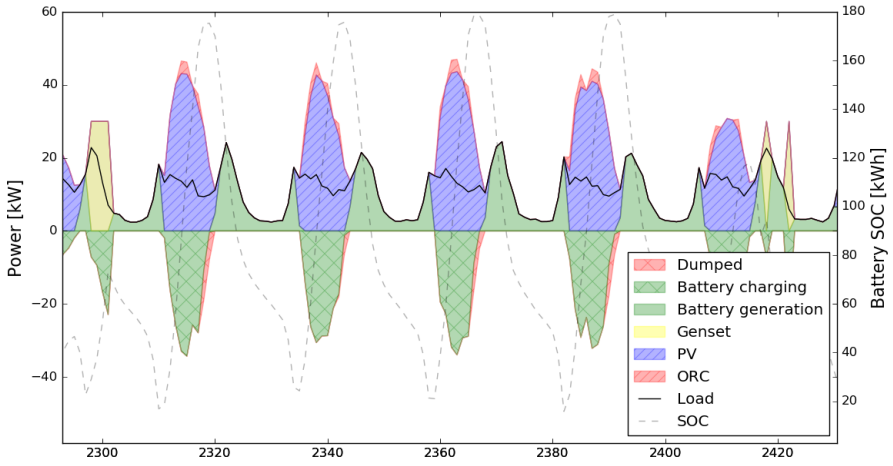

Figure 5.14: Power dispatch for simulation 3

Table 5.10: Optimization results of several simulations

	Sim 1	**Sim 2**	**Sim 3**
heating system	TES	TES	ORC
E_{batt} [kWh]	259	146	181
$P_{nom,PV}$ [kW]	65	0	58
A_{CSP} [m^2]	0	223	98
E_{TES} [kWh]	0	611	118
$P_{nom,ORC}$ [kW]	0	5	3.5
LCOE [USD/kWh]	**0.202**	**0.745**	**0.364**
LCOE$_{ThEl}$ [USD/kWh]	**0.164**	**0.470**	**0.258**
Total propane consumption [kg]	**5655**	**38860**	**7552**
Total load [kWh]	**97041**	**97041**	**97041**
Total PV generation [kWh]	123568	0	110261
Total ORC generation [kWh]	0	10817	4729
Total Genset generation [kWh]	2070	96630	9031
Total thermal load [kWh]	**58745**	**58745**	**58745**
Total heating system generation [kWh]	0	49029	17405
Total burner generation [kWh]	58745	9717	46657

Table 5.11: Simulation 3: New Investment costs

Parameter	**Previous Value**	**New Value**	**Units**
c_{batt}	130	300	USD/kWh
c_{panels}	1000	1500	USD/kW
c_{ORC}	2000	1000	USD/kW

Chapter 6

Conclusions and Future Works

This work has focused on multiple aspects of the ongoing development of solar hybrid microgrids for the rural electrification of remote areas in Lesotho. These aspects range from very specific improvements (the mechanical design of a high expansion ratio expander) to the more global evaluation of their impact once included into a complex micro-grid system. Special attention has also been paid to the links between thermal and electrical demands.

The mechanical design of the expander involved drawing, machining and assembling multiple mechanical pieces. The new design presents the advantage of being semi hermetic, maintaining the lubrication fluid in the shell with no leakages but also allowing for disassembly. The innovative lubrication system is designed to avoid installing a manifold inside the shell of the expander. Moreover, the drive and driven side are physically separated by a magnetic coupling, which allows e.g. replacing the motor without having to disassemble the expander. In order to avoid axial scroll unloading or excessive scroll frictions, the axially compliance mechanism and the floating seal are actively controlled by a valve that allows modifying the intermediate pressure within the back pressure chamber.

The manufacturing and assembly process took three weeks. While the former was performed at the MIT, the latter was performed in Florida, where the ORC prototype test rig developed by STG International is installed. However, because of the limited time period of this Master thesis, the expander could only be installed within the ORC. In order to validate the expected performance brought by the new geometric scroll design and the new expander mechanical-lubrication design, the expander will be tested in the coming months by STG.

In the meantime, the ORC model developed in Chapter 2 indicates that the ORC performs better when high expansion ratio expanders are used. Therefore, if the expected performance is validated in the future expander tests, the designed scroll expander will bring a significant improvement in small-scale ORC systems. Moreover, because of the nature of the ORC, the possibility of co-generation is allowed by a specific configuration of the condenser. Although the simulation results showed that the ORC performance are slightly lower when co-generation is used, this should be balanced by the value of heat production.

Concurrently, a building model to predict the thermal demand of a typical health clinic in Lesotho has been developed. In order to operate with limited information, the model is

based on a lumped-parameter approach. An optimization is therefore performed to determine the unknown characteristics of the building from historical data. The main objective is to reduce the discrepancy between the model prediction and the measurements. Optimization results presented a centered error distribution and an acceptable RMSE. Finally, a load profile is obtained according to those parameters that maintains the building temperature in the selected range of 20ºC and 15ºC. The simulated annual total consumption is 21734 kWh per year, and the specific total consumption is 95 kWh/m^2 per year.

The developed lumped-parameter model can be used for various building typologies and communities. The model, which has just one input characteristic of the building (its surface) and two inputs related to weather conditions (outside temperature and irradiation), contrasts with the data-intensive models generally proposed in the literature. Such model could readily be re-used by other users who need to predict the thermal load of health clinics or schools in remote rural areas, where information is currently sparse.

Finally, starting from the model of the improved ORC and the heating and electricity demand profiles, a microgrid model is built by interconnecting all of its subcomponents models. The PV and LPG generator models, the solar irradiation, and the dynamics of storage are sub-models also developed in this thesis and integrated in the microgrid model. The most relevant part of this chapter is the proposed rule-based control strategy, which accounts for interactions between thermal and electrical loads. The control dispatches heat and power flows of each component in order to cover the demand while minimizing the fuel consumption. This model allows simulating the improvement linked to the use of the higher expansion ratio expander, leading to a maximum decrease of 25% in fuel consumption throughout the year.

The developed microgrid model together with an economical model is finally wrapped into a non-linear optimization run by the PSO algorithm. For Ha Nkau, the studied community in Lesotho, the determined optimal system infrastructure is composed of only PV (65 kW) and batteries (259 kWh), and the optimum control strategy achieves a tariff (LCOE) value of 0.202 USD/kWh. Fuel consumption is mainly generated by the burner, which supplies all of the thermal load because no other heating system (ORC or TES) is installed. The project presents an investment cost of 153035 USD and a life-time of 15 years. Batteries are replaced every 8 years. The obtained tariff is considered to be an affordable cost for householders and institutions (health clinics and schools) of a community. Moreover, the low propane consumption of 5655 kg per year dramatically reduces CO_2 emissions compared to a genset-only configuration, which was also a goal of this work.

The model is designed to cover demand at all times. Although the optimal solution found by the proposed rule-based control strategy may be less optimal than if a perfect foresight control was used, the obtained power flows are more realistic since they account for the inefficiencies encountered in real systems. The same model can be used when only electricity is supplied to a community.

6.1 Future Works

As a remaining work, the expander designed and built in the scope of this thesis should be tested in an ORC prototype. This is a work in progress by STG International, in their developed micro-CSP test rig in Florida. Any mechanical problem encountered in the testing process should be used to improve the expander design. Since the expander

is semi-hermetic, it can be disassembled to replace some parts and re-assembled without having to manufacture the whole expander again.

Current values of the expander performance in the ORC model developed in Chapter 2 correspond to theoretical values computed in [13]. Therefore, the validated experimental performance obtained from the tests should be added to the model so that the latter gives more accurate results. The more realistic correlations of the ORC performances should be then added to the microgrid model.

The parametrization of the building model of Chapter 4 was based on the data provided by STG International. However, since the monitoring campaigns provided by the latter started in 2015, only 10 months of data were acquired. The optimization, which is based on October to December (i.e. the available warm months, where electricity data from the buildings do not contain electrical heaters load), could be improved by adding the January to March data. Additionally, the general use of the model could be further validated if weather stations were installed in more clinics and more data was available.

Although the climate of Lesotho entails important heating demand, the model could also be further adapted to compute the cooling loads in the warmest months. In addition, a comprehensive research of appropriate cooling systems should be performed, since classical air-conditioning technologies might not be appropriate for rural regions of Sub-Saharan Africa.

Finally, the microgrid simulation results show that although having assets such as cogeneration and dispatchability, the ORC is more expensive than PV and the batteries storage. This is partly explained by the fact that the heat load of a clinic and a school remain limited: heat production is more cost-effective with a burner than installing a micro-CSP plant with TES. Another possibility is to include the use of locally harvested biomass as a thermal source to supplement solar thermal collection, which could raise the capacity factor of the ORC and improve the value of investment. Because of the high solar potential of Lesotho, the possibility of installing flat solar thermal collectors together with the adequate TES tank could also be evaluated. This cost-effective technology could mitigate the use of the burner.

It should finally be noted that the presented rule-based control is the first thermal-electricity interactive control developed related to the microgrid project of STG International. The code can be used to evaluate a number of different simulations, the results of which could serve to improve the rule based control. Such improvements could lead to a better use of the ORC and of the thermal storage, which could increase their economic viability.

Bibliography

[1] W. Bank, The Welfare Impact of Rural Electrification: A Reassessment of the Costs and Benefits, Tech. rep., World Bank (2008).

[2] S. Quoilin, M. Orosz, Rural Electrification through Decentralized Concentrating Solar Power: Technological and Socio-Economic Aspects, Journal of Sustainable Development of Energy, Water and Environment Systems.

[3] M. Orosz, STG International (Aug. 2016).
URL `http://www.stginternational.org/`

[4] M. S. Orosz, S. Quoilin, H. Hemond, Technologies for heating, cooling and powering rural health facilities in sub-Saharan Africa, Proceedings of the Institution of Mechanical Engineers, Part A: Journal of Power and Energy.

[5] S. Mandelli, M. Merlo, E. Colombo, Novel procedure to formulate load profiles for off-grid rural areas, Energy for Sustainable Development 31 (2016) 130–142. doi:10.1016/j.esd.2016.01.005.

[6] H. Energy, HOMER Renewable Energy Microgrid Software | Distributed Power and Microgrid Design Support (Aug. 2016).
URL `http://www.homerenergy.com/software.html`

[7] S. Balderrama, W. Canedo, V. Lemort, S. Quoilin, Techno-economic optimization of isolate micro-grids including PV and Li-Ion Batteries in the Bolivian context, Proceedings of ECOS 2016 - the 29th International Conference on Efficiency, Cost, Optimization, Simulation and Environmental Impact of Energy Systems.

[8] V. François-Lavet, Q. Gemine, D. Ernst, R. Fonteneau, Towards the Minimization of the Levelized Energy Costs of Microgrids using both Long-term and Short-term Storage Devices.

[9] M. Orosz, R. Dickes, Chapter 17 - Solar Powered ORCs, in: Organic Rankine Cycle (ORC) Power Systems: Technologies and Applications.
URL `http://orbi.ulg.ac.be/handle/2268/191115`

[10] S. Quoilin, M. V. D. Broek, S. Declaye, P. Dewallef, V. Lemort, Techno-economic survey of Organic Rankine Cycle (ORC) systems, Renewable and Sustainable Energy Reviews 22 (2013) 168–186. doi:10.1016/j.rser.2013.01.028.

[11] V. Lemort, S. Declaye, S. Quoilin, Experimental characterization of a hermetic scroll expander for use in a micro-scale Rankine cycle, Proceedings of the Institution of Mechanical Engineers, Part A: Journal of Power and Energy 226 (1) (2012) 126–136. doi:10.1177/0957650911413840.

[12] S. Declaye, S. Quoilin, L. Guillaume, V. Lemort, Experimental study on an open-drive scroll expander integrated into an ORC (Organic Rankine Cycle) system with R245fa as working fluid, Energy 55 (2013) 173–183. doi:10.1016/j.energy.2013.04.003.

[13] R. Dickes, Design and fabrication of a variable wall thickness two-stage scroll expander to be integrated in a micro-solar power plant, Master thesis, University of Liege, Belgium (2013).

[14] S. Quoilin, M. Orosz, H. Hemond, V. Lemort, Performance and design optimization of a low-cost solar organic Rankine cycle for remote power generation, Solar Energy.

[15] M. Orosz, S. Quoilin, H. Hemond, SORCE: A design tool for solar organic Rankine cycle systems in distributed generation applications, International Scientific Conference on Solar Heating, Cooling and Buildings.

[16] E. Georges, S. Declaye, O. Dumont, S. Quoilin, V. Lemort, Design of a small-scale organic Rankine cycle engine used in a solar power plant, International Journal of Low-Carbon Technologies 8 (suppl 1) (2013) i34–i41. doi:10.1093/ijlct/ctt030.

[17] B. Thonon, R. Vidil, C. Marvillet, Recent Research and Developments in Plate Heat Exchangers, Journal of Enhanced Heat Transfer 2 (1-2) (1995) 149–155. doi:10.1615/JEnhHeatTransf.v2.i1-2.160.

[18] Y. Y. Hsieh, T. F. Lin, Evaporation Heat Transfer and Pressure Drop of Refrigerant R-410a Flow in a Vertical Plate Heat Exchanger, Journal of Heat Transfer 125 (5) (2003) 852–857. doi:10.1115/1.1518498.

[19] Q. Altés Buch, Dynamic modeling of a steam Rankine Cycle for concentrated solar power applications, Bachelor thesis, Polytechnic University of Catalonia, University of Liege, Belgium (2014).

[20] Q. Altés Buch, R. Dickes, A. Desideri, V. Lemort, S. Quoilin, Dynamic modeling of thermal systems using a semi-empirical approach and the ThermoCycle Modelica Library.

[21] T. Yamamoto, T. Furuhata, N. Arai, K. Mori, Design and testing of the Organic Rankine Cycle, Energy 26 (3) (2001) 239–251. doi:10.1016/S0360-5442(00)00063-3.

[22] M. Mitterhofer, Cogeneration in Off-Grid Areas with a micro-Concentrated Solar Power System - Simulation and Optimization, Master thesis, Technical University of Munich, Germany (2014).

[23] M. K. Ireland, Dynamic modeling and control strategies for a micro-CSP plant with thermal storage powered by the Organic Rankine cycle, Master thesis, Massachusetts Institute of Technology (2014).

[24] V. Lemort, S. Quoilin, C. Cuevas, J. Lebrun, Testing and modeling a scroll expander integrated into an Organic Rankine Cycle, Applied Thermal Engineering 29 (14–15) (2009) 3094–3102. doi:10.1016/j.applthermaleng.2009.04.013.

[25] C. Lin, Feasibility of using power steering pumps in small-scale solar thermal electric power systems, Thesis, Massachusetts Institute of Technology (2008).

[26] B. Dechesne, Designing a Scroll Expander for a Micro-Solar Power Plant, Master thesis, University of Liege, Belgium (2012).

[27] O. Dumont, S. Quoilin, V. Lemort, Experimental investigation of a reversible heat pump/organic Rankine cycle unit designed to be coupled with a passive house to get a Net Zero Energy Building, International Journal of Refrigeration.

[28] C. Pire, Etude experimentale d'un compresseur scroll hermetique en mode expanseur: Analyse et Modelisation du composant, Master thesis, University of Liege, Belgium (2009).

[29] R. Wallonne, Le Logiciel PEB (Version 7.5.0) (May 2016).
URL `http://energie.wallonie.be/fr/logiciel-peb.html?IDC=7303`

[30] G. Masy, Definition and validation of a simplified multizone dynamic building model connected to heating system and HVAC unit, Master thesis, University of Liege, Belgium (2008).

[31] ASHRAE, Standard 62, ventilation for acceptable indoor air quality, technical report. (2007).

[32] ASHRAE, Standard 55, thermal environmental conditions for human occupancy, technical report (2010).

[33] O. Seppänen, W. Fisk, D. Faulkner, Cost benefit analysis of the night-time ventilative cooling in office building, Singapore, 2003.

[34] P. Sumner, A contemporary winter ground thermal profile in the Lesotho highlands and implications for active and relict soil frost phenomena, Earth Surface Processes and Landforms 28 (13) (2003) 1451–1458. doi:10.1002/esp.1003.

[35] H. C. Fennell, J. Haehnel, Setting airtightness standards, ASHRAE journal 47 (9) (2005) 26.

[36] M. S. Orosz, A. V. Mueller, Dynamic Simulation of Performance and Cost of Hybrid PV-CSP-LPG Generator Micro Grids With Applications to Remote Communities in Developing Countries.

[37] S. Ghaem Sigarchian, M. S. Orosz, H. F. Hemond, A. Malmquist, Optimum design of a hybrid PV–CSP–LPG microgrid with Particle Swarm Optimization technique, Applied Thermal Engineeringdoi:10.1016/j.applthermaleng.2016.05.119.

[38] P. G. Loutzenhiser, H. Manz, C. Felsmann, P. A. Strachan, T. Frank, G. M. Maxwell, Empirical validation of models to compute solar irradiance on inclined surfaces for building energy simulation, Solar Energy 81 (2) (2007) 254–267. doi:10.1016/j.solener.2006.03.009.

[39] T. M. Klucher, Evaluation of models to predict insolation on tilted surfaces, Solar Energy 23 (2) (1979) 111–114. doi:10.1016/0038-092X(79)90110-5.

[40] E. Lorenzo, L. Narvarte, J. Muñoz, Tracking and back-tracking, Progress in Photovoltaics: Research and Applications 19 (6) (2011) 747–753. doi:10.1002/pip.1085.
URL `http://onlinelibrary.wiley.com/doi/10.1002/pip.1085/abstract`

[41] K. Emery, Measurement and Characterization of Solar Cells and Modules, in: A. Luque, S. Hegedus (Eds.), Handbook of Photovoltaic Science and Engineering, John Wiley & Sons, Ltd, 2010, pp. 797–840.

[42] O. Cummins, RV generator set Quiet Gasoline TM Series RV QG 4000 (Jun. 2016). URL `http://coloradostandby.com/media/custom/upload/document_technical_a-1399.pdf`

[43] S. Panda, N. P. Padhy, Comparison of particle swarm optimization and genetic algorithm for FACTS-based controller design, Applied Soft Computing 8 (4) (2008) 1418–1427. doi:10.1016/j.asoc.2007.10.009.

[44] B. Tudu, S. Majumder, K. K. Mandal, N. Chakraborty, Comparative Performance Study of Genetic Algorithm and Particle Swarm Optimization Applied on Off-grid Renewable Hybrid Energy System, in: B. K. Panigrahi, P. N. Suganthan, S. Das, S. C. Satapathy (Eds.), Swarm, Evolutionary, and Memetic Computing, Springer Berlin Heidelberg, 2011, pp. 151–158.

[45] H. Xiaohui, Particle Swarm Optimization (Jul. 2016). URL `http://swarmintelligence.org/`

[46] J. Kennedy, R. Eberhart, Particle swarm optimization, in: , IEEE International Conference on Neural Networks, 1995. Proceedings, Vol. 4, 1995, pp. 1942–1948 vol.4. doi:10.1109/ICNN.1995.488968.

[47] W. Edge, Water Jet Cutting Services Perth (Aug. 2016). URL `http://edgeworkshop.com.au/water-jet-cutting/`

Annex A: Machining Processes and Drawings

Water jet cutter Industrial tool used to cut a wide variety of materials by impacting on them a high-velocity water jet that can be mixed with an abrasive substance. The latter is required when cutting hard materials such as metal or granite. This method suites materials sensible to high-temperature. Also, being a CNC technology, water jet cutter ensures high accuracy.

– *Principle*: As shown in Figure 6.1, the process consists in focusing water into a beam by a nozzle. High pressure water travels through tubing to the water jet nozzle, where it is focused into a thin beam by a jewel orifice. After feeding the nozzle with abrasives, the high-speed water jet is ejected and sprays the material cutting it through. The material is placed on a grill contained in a water pool. The grill not only allows keeping the material fixed close to the water surface but also prevents the ejected liquid to splash out of the cutting zone. Water can be recycled using a closed-loop system.

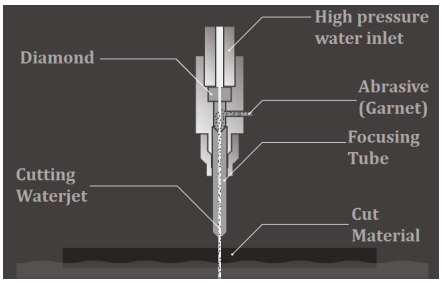

Figure 6.1: Diagram of a water jet cutter [47]

– *Process*: The designed part in CAD must be introduced with the appropriate file extension in the program used by the cutting machine. Material characteristics (e.g. hardness) and the desired type of cut (e.g. roughly or highly defined) can be added in the software. The latter will propose the optimum cutting path and show the starting point to the user. All variables selected, the following step is to adjust and fix the raw material in a strategic position that maximizes profitability by wasting the minimum material, as shown in Figure 6.2a. In order for the process to start, the origin coordinates and the vertical position of the tool in respect to the material must also be defined. The latter is set as shown in Figure 6.2b and depends on the material thickness. A simulation of the process (i.e. the tool goes through the path at some distance above the material) can be done to see if everything seems correct

(a) Water jet cutter: Placing work piece on pool's grill

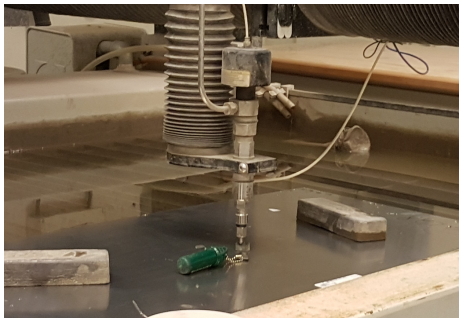

(b) Water jet cutter: Setting tool height

(c) Water jet cutter: Cutting operation in progress

(d) Lathe

(e) Vertical mill

(f) CNC machining center

Figure 6.2: Machines used at MIT

to the eye. If so, the pool can be filled up and the process can then start. The water jet cutter used in the scope of this thesis can be seen working on a piece in Figure 6.2c. The machine will do the work and stop at the end automatically. However,

problems can occur during the process. E.g. a common issue that reduces water jet velocity leading to a partial cut would be a nozzle blocked by some abrasive material. In any case, the user can pause the process and resume it when convenient.

Milling machine Milling is a machining process that consists on removing material from a work piece by using rotatory cutters. Cutting tools tend to have multiple cutting edges and move into a direction and angle with the tool's axis. Usually, cutters are moved perpendicular to its axis i.e. not along its axis of rotation. The cutting action depends on the milling process, being mainly *face milling*, used to cut flat surfaces or cavities, and *peripheral milling*, used to cut deep slots, threads and gear teeth.

Although a wide range of machine tools can be used for milling, the milling work in the scope of this thesis has mainly been done in CNC machining centers because of the ease of the process. Figures 6.2e and 6.2f show both used vertical and CNC mills.

Lathe A lathe is a machine tool that, based on a revolution movement, creates objects with symmetry about the rotation axis. Several types of operations (e.g. cutting, drilling, knurling, sanding) can be performed on a part. The working principle consists on rotate a piece on its axis while one or several cutting tools are moved forward to the piece surface and cut it. From more to less stability, the work piece can be *between centers* (i.e. fixed between the headstock and the tail-stock) or *face work* (i.e. only fixed at the headstock end). Work should be done essentially axially for the latter.

Nowadays, Computer Numeric Control (CNC) lathes allow high-production and high-accuracy pieces. Also, even producing objects with complex profiles is achievable for non-expert users.

Drawings In order of appearance:

- Casing top plate
- Lower stator
- Shaft adapter
- Stator support cylinders
- Casing
- Crank shaft
- Bottom journal bearing
- Bottom journal bearing support
- Casing bottom plate
- Case support
- Sleeve bearing

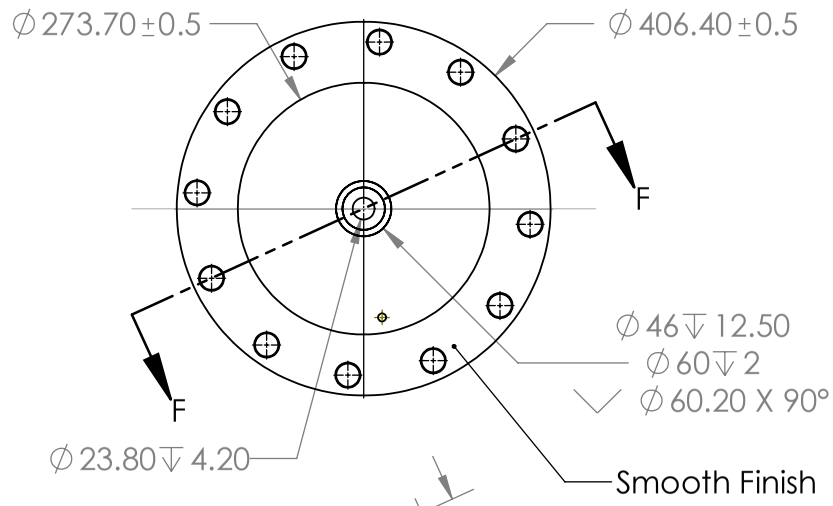

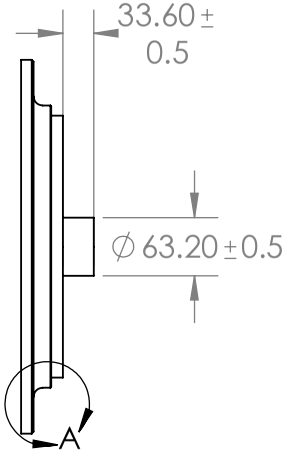

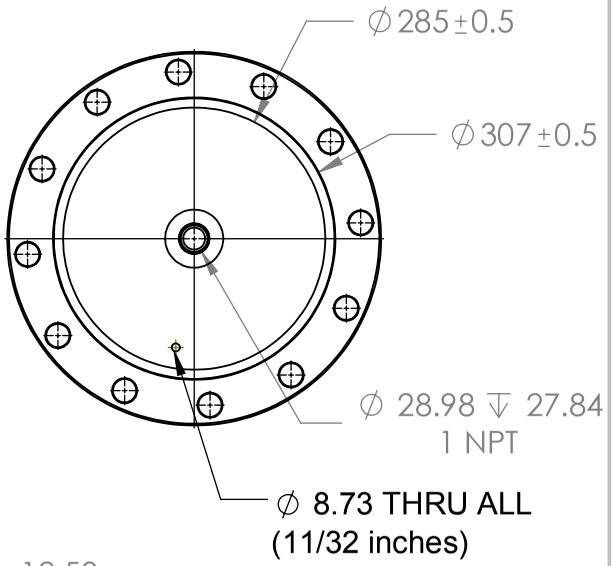

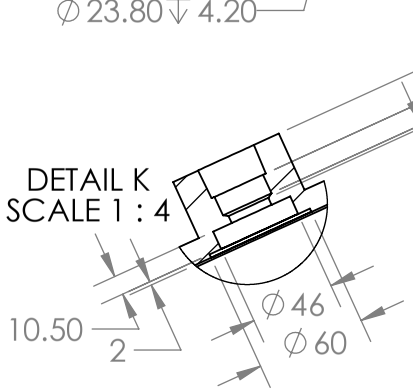

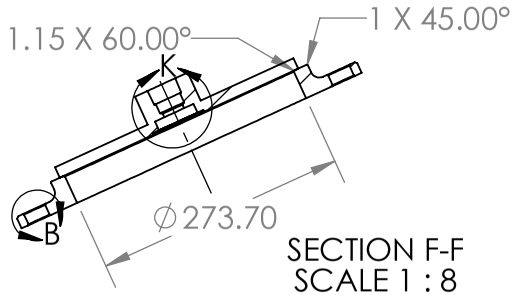

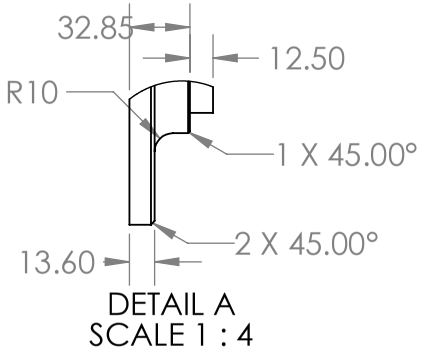

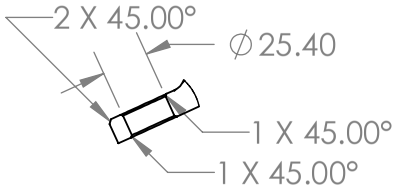

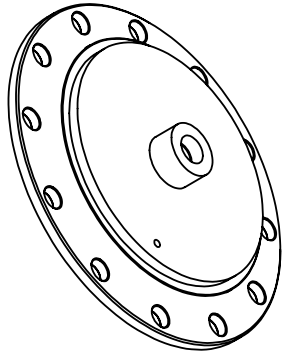

All inner surfaces of holes: Smooth finish

		UNLESS OTHERWISE SPECIFIED:		NAME	DATE
		DIMENSIONS ARE IN MILLIMETERS TOLERANCES: 0.015 FRACTIONAL ± ANGULAR: MACH ± BEND ± TWO PLACE DECIMAL ± THREE PLACE DECIMAL ±	DRAWN		
			CHECKED		
			ENG APPR.		
			MFG APPR.		
		INTERPRET GEOMETRIC TOLERANCING PER:	Q.A.		
		MATERIAL: MILD STEEL	COMMENTS: This piece can can be made from a standard 10-inch pipe - these are available from plumbing suppliers		
NEXT ASSY	USED ON	FINISH: STANDARD ROUGH			
APPLICATION		DO NOT SCALE DRAWING			

TITLE:

01_casing_top_plate

SIZE	DWG. NO.	REV
A		

SCALE: 1:8	WEIGHT:	SHEET 1 OF 1

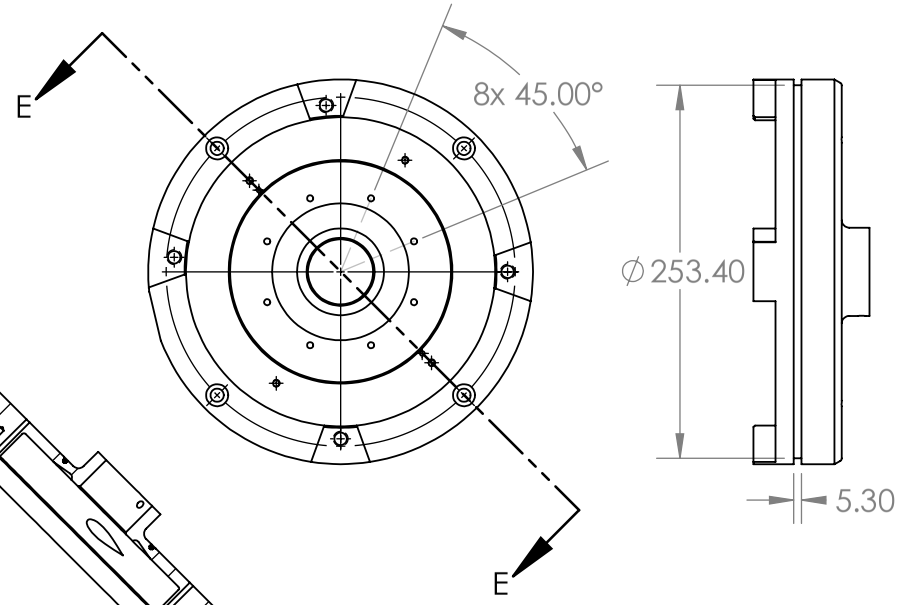

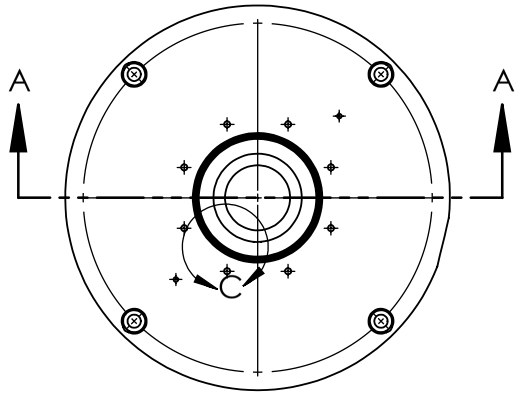

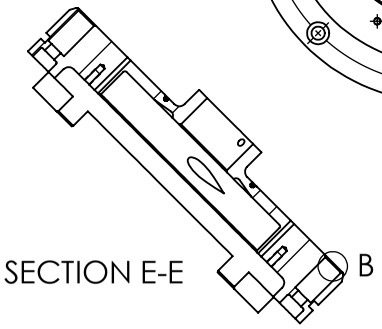

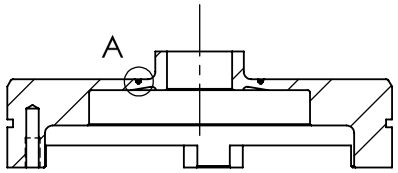

SECTION A-A

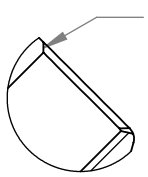

DETAIL B
SCALE 1 : 1

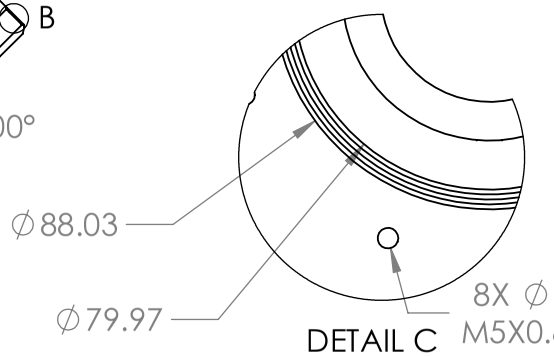

DETAIL C
SCALE 1 : 1.5

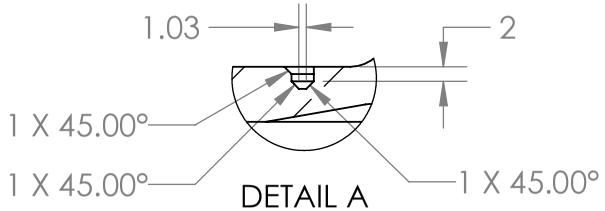

DETAIL A
SCALE 1 : 1

		UNLESS OTHERWISE SPECIFIED:		NAME	DATE
		DIMENSIONS ARE IN MILLIMETERS TOLERANCES: 0.015 FRACTIONAL ± ANGULAR: MACH ± BEND ± TWO PLACE DECIMAL ± THREE PLACE DECIMAL ±	DRAWN		
			CHECKED		
			ENG APPR.		
			MFG APPR.		
		INTERPRET GEOMETRIC TOLERANCING PER:	Q.A.		
		MATERIAL: MILD STEEL	COMMENTS: This piece has already been machined. Only the modifications indicated in this drawing need to be added to the already machined piece.		
NEXT ASSY	USED ON	FINISH: SMOOTH			
APPLICATION		DO NOT SCALE DRAWING			

TITLE:

14_lower_stator

SIZE	DWG. NO.	REV
A		

SCALE: 1:5	WEIGHT:	SHEET 1 OF 1

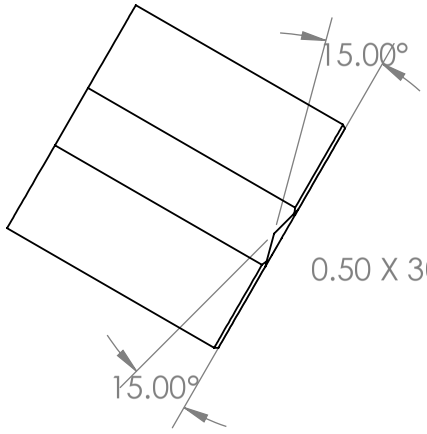

VIEW D-D

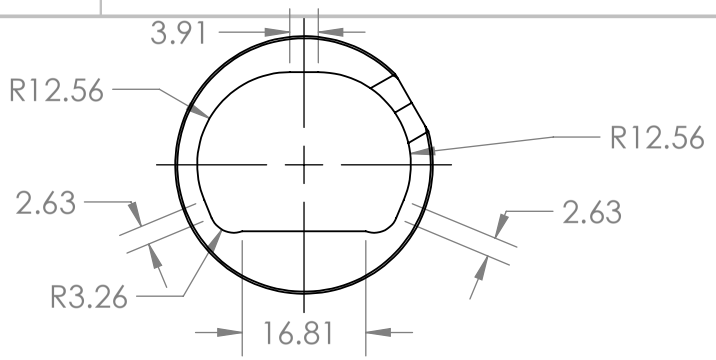

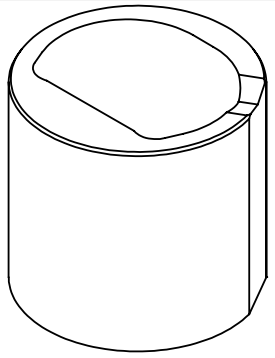

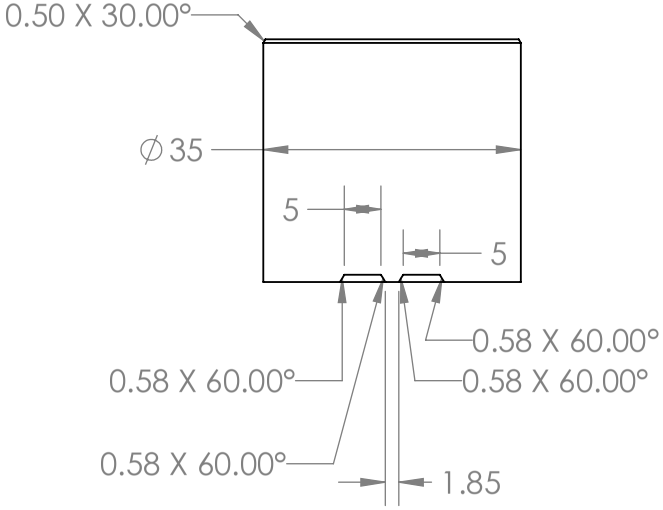

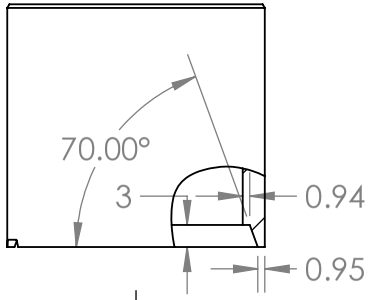

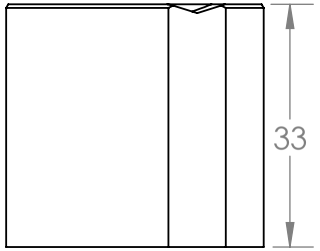

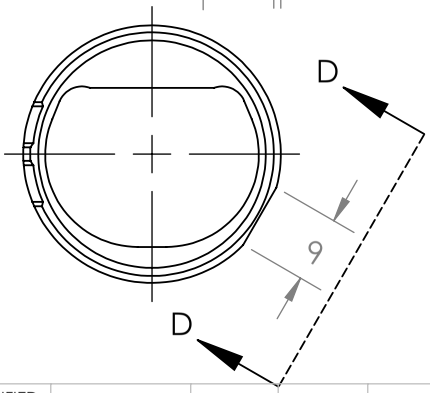

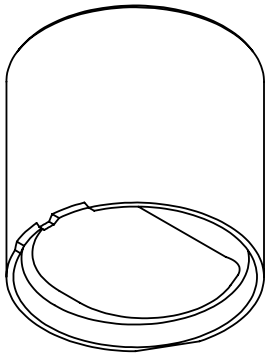

		UNLESS OTHERWISE SPECIFIED:		NAME	DATE
		DIMENSIONS ARE IN INCHES TOLERANCES: 0.015 FRACTIONAL ± ANGULAR: MACH ± BEND ± TWO PLACE DECIMAL ± THREE PLACE DECIMAL ±	DRAWN		
			CHECKED		
			ENG APPR.		
			MFG APPR.		
		INTERPRET GEOMETRIC TOLERANCING PER:	Q.A.		
		MATERIAL: MILD STEEL	COMMENTS:		
NEXT ASSY	USED ON	FINISH: SMOOTH			
APPLICATION		DO NOT SCALE DRAWING			

TITLE:

12_shaft_adapter

SIZE	DWG. NO.	REV
A		

SCALE: 1:1	WEIGHT:	SHEET 1 OF 1

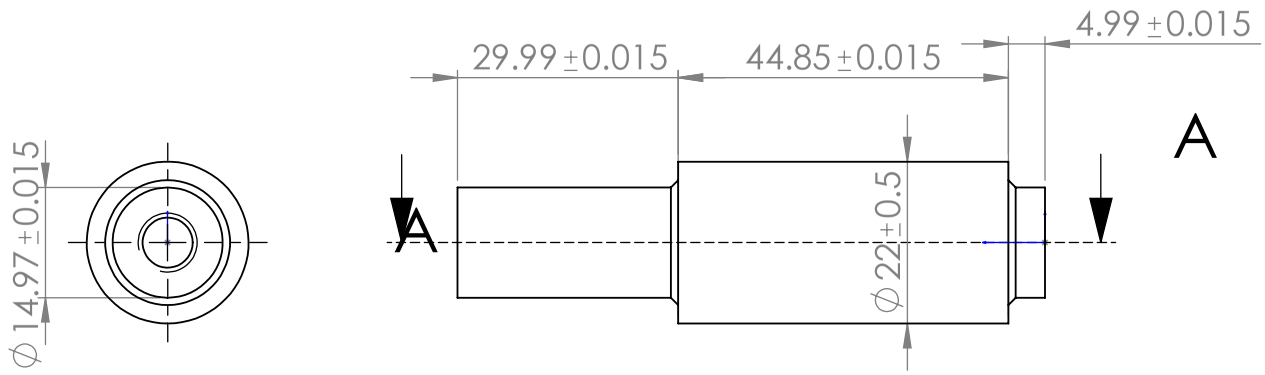

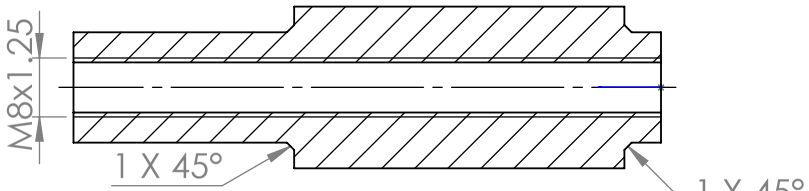

SECTION A-A

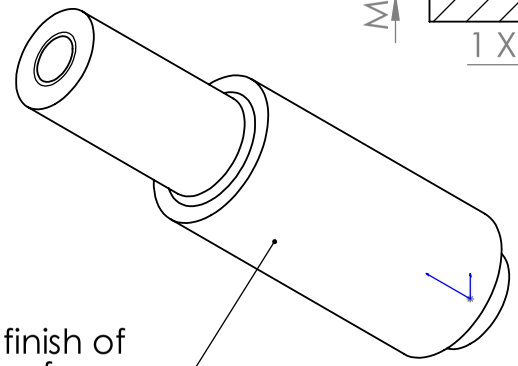

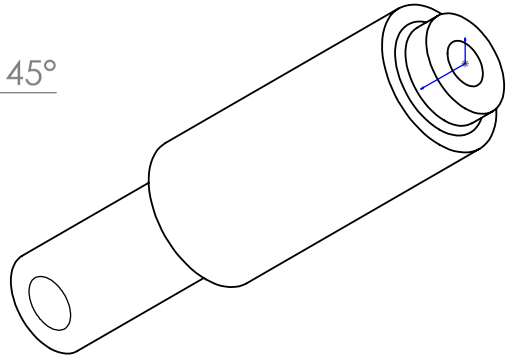

The finish of this surface can be standard rough

		UNLESS OTHERWISE SPECIFIED:		NAME	DATE
		DIMENSIONS ARE IN MILLIMETERS TOLERANCES: 0.015 FRACTIONAL ± ANGULAR: MACH ± BEND ± TWO PLACE DECIMAL ± THREE PLACE DECIMAL ±	DRAWN		
			CHECKED		
			ENG APPR.		
			MFG APPR.		
		INTERPRET GEOMETRIC TOLERANCING PER:	Q.A.		
		MATERIAL: MILD STEEL	COMMENTS:		
NEXT ASSY	USED ON	FINISH: SMOOTH			
APPLICATION		DO NOT SCALE DRAWING			

<COMPANY NAME>

TITLE:

16_TUBES_STATOR_SUPPORT

SIZE	DWG. NO.	REV
A		

SCALE: 1:1		SHEET 1 OF 1

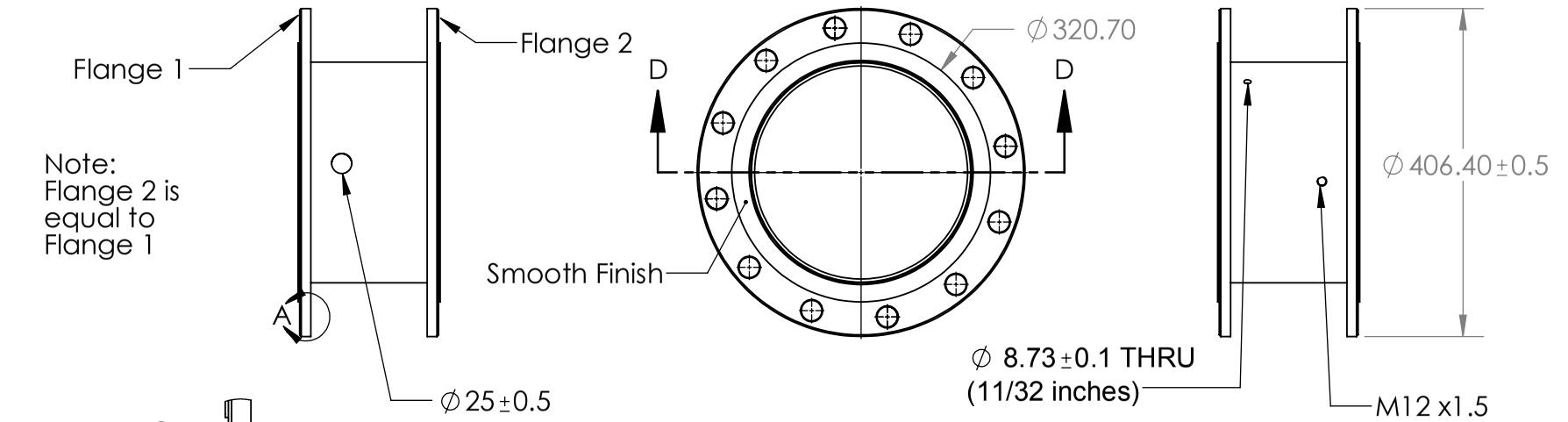

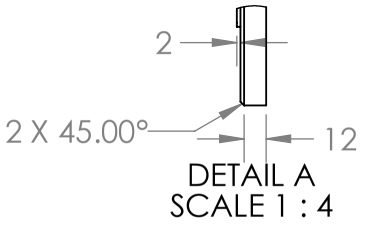

DETAIL A
SCALE 1 : 4

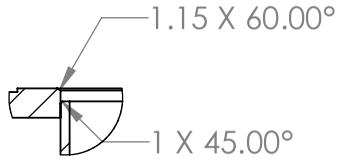

DETAIL B
SCALE 1 : 4

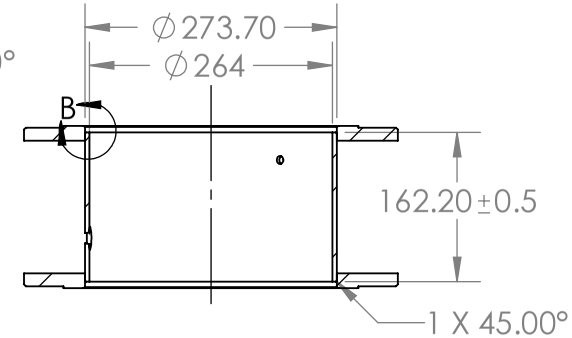

SECTION D-D
SCALE 1 : 8

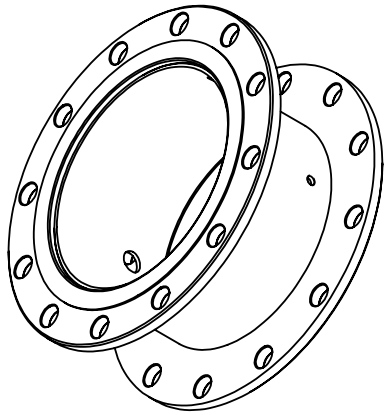

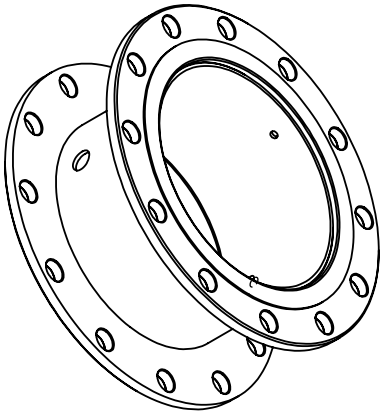

All inner surfaces of holes: Smooth finish

		UNLESS OTHERWISE SPECIFIED:
		DIMENSIONS ARE IN MILLIMETERS TOLERANCES: 0.015 FRACTIONAL ± ANGULAR: MACH ± BEND ± TWO PLACE DECIMAL ± THREE PLACE DECIMAL ±
		INTERPRET GEOMETRIC TOLERANCING PER:
		MATERIAL: MILD STEEL
NEXT ASSY	USED ON	FINISH: STANDARD ROUGH
APPLICATION		DO NOT SCALE DRAWING

	NAME	DATE
DRAWN		
CHECKED		
ENG APPR.		
MFG APPR.		
Q.A.		

COMMENTS:
This piece can can be made from a standard 10-inch pipe - these are available from plumbing suppliers

TITLE:

17_casing_main

SIZE	DWG. NO.	REV
A		

SCALE: 1:8	WEIGHT:	SHEET 1 OF 1

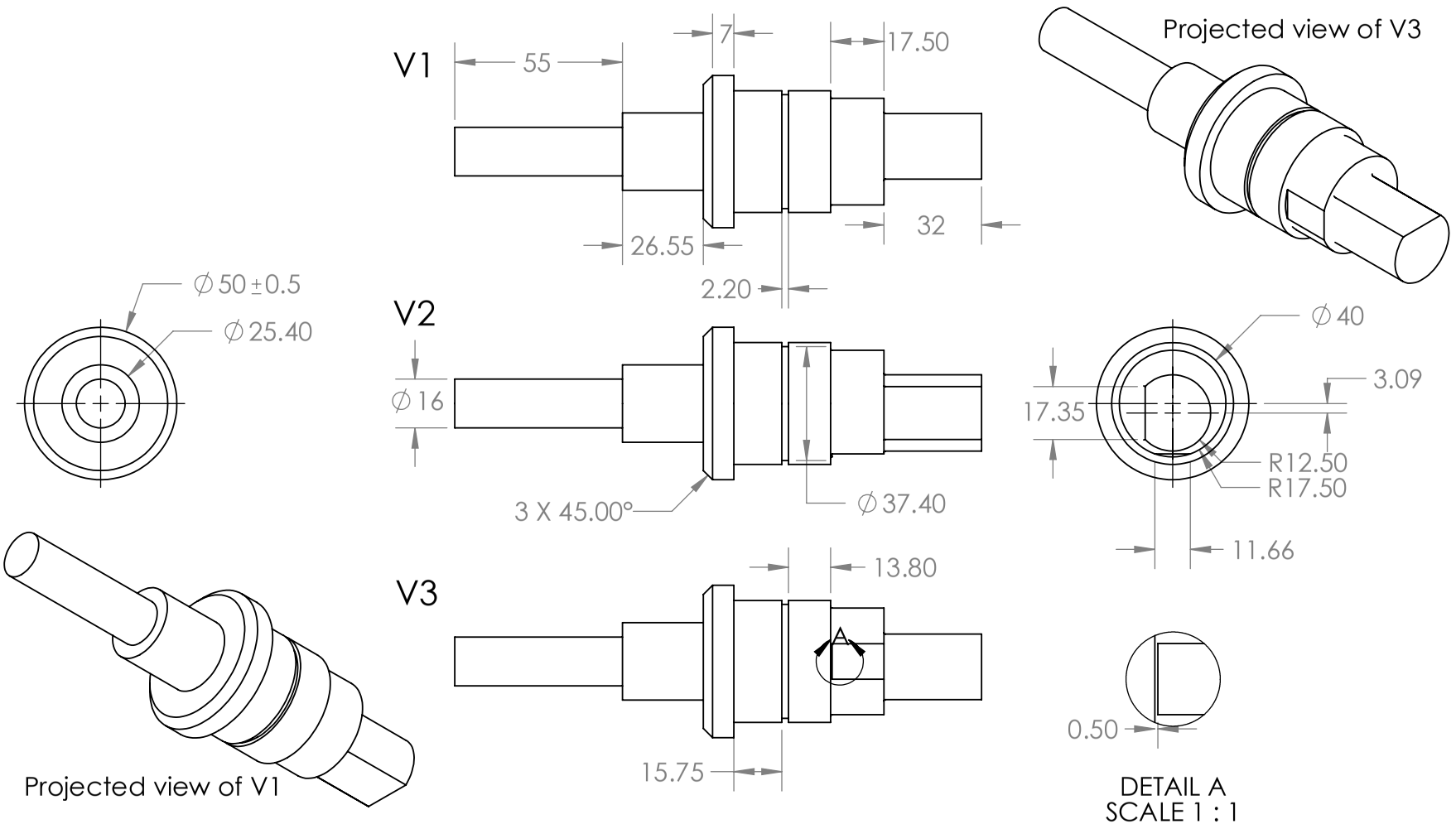

		UNLESS OTHERWISE SPECIFIED:		NAME	DATE
		DIMENSIONS ARE IN MILLIMETERS TOLERANCES: 0.015 FRACTIONAL ± ANGULAR: MACH ± BEND ± TWO PLACE DECIMAL ± THREE PLACE DECIMAL ±	DRAWN		
			CHECKED		
			ENG APPR.		
			MFG APPR.		
		INTERPRET GEOMETRIC TOLERANCING PER:	Q.A.		
		MATERIAL: SHAFT STEEL	COMMENTS:		
NEXT ASSY	USED ON	FINISH: GROUND SMOOTH			
APPLICATION		DO NOT SCALE DRAWING			

TITLE:

18_crank_shaft

SIZE	DWG. NO.	REV
A		

SCALE: 1:2	WEIGHT:	SHEET 1 OF 1

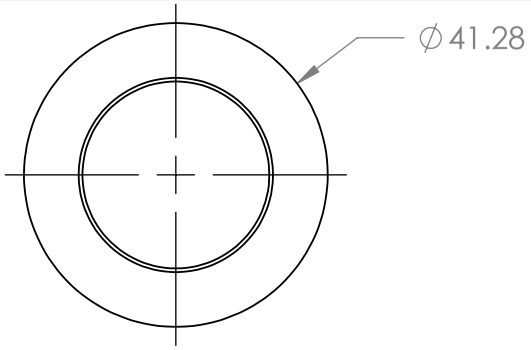

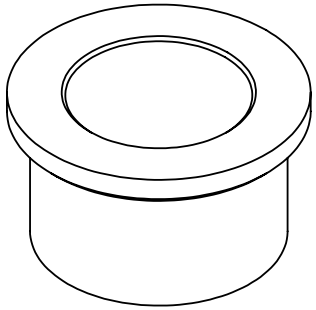

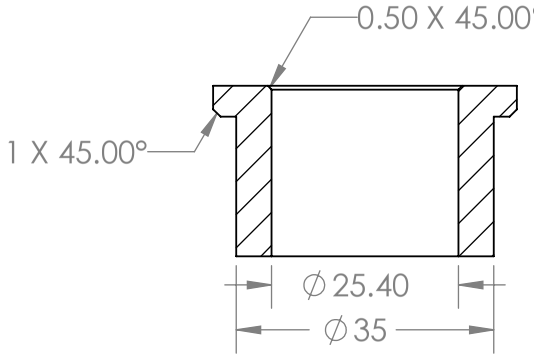

SECTION A-A

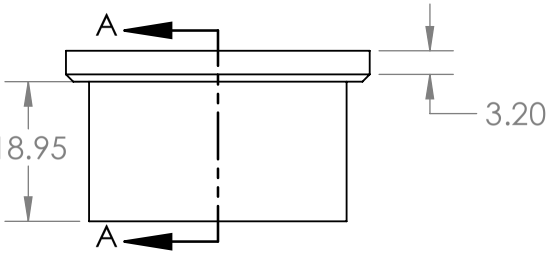

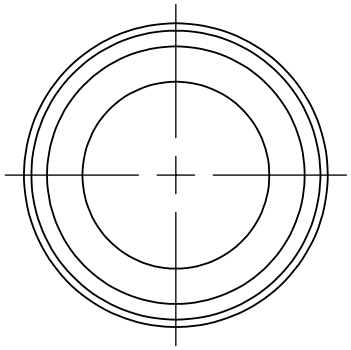

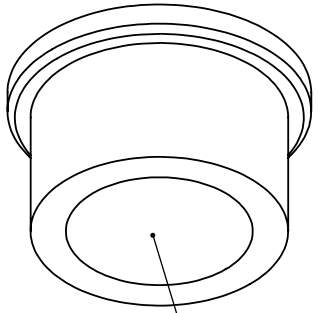

Ground Smooth

		UNLESS OTHERWISE SPECIFIED:		NAME	DATE
		DIMENSIONS ARE IN MILLIMETERS TOLERANCES: 0.015 FRACTIONAL ± ANGULAR: MACH ± BEND ± TWO PLACE DECIMAL ± THREE PLACE DECIMAL ±	DRAWN		
			CHECKED		
			ENG APPR.		
			MFG APPR.		
		INTERPRET GEOMETRIC TOLERANCING PER:	Q.A.		
		MATERIAL:OIL IMPREGNED BRONZE	COMMENTS:		
NEXT ASSY	USED ON	FINISH: SMOOTH			
APPLICATION		DO NOT SCALE DRAWING			

TITLE:

19_bearing_journal_bottom

SIZE	DWG. NO.	REV
A		

SCALE: 1:1	WEIGHT:	SHEET 1 OF 1

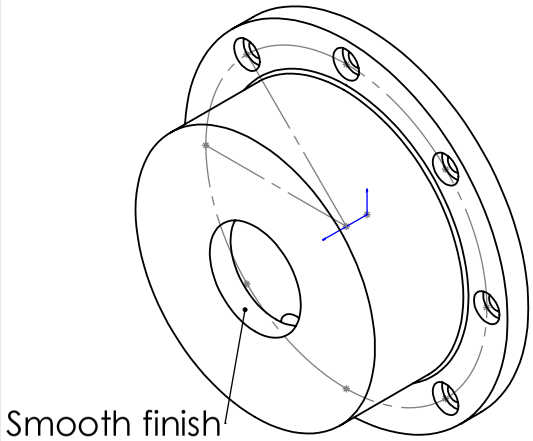

SECTION H-H

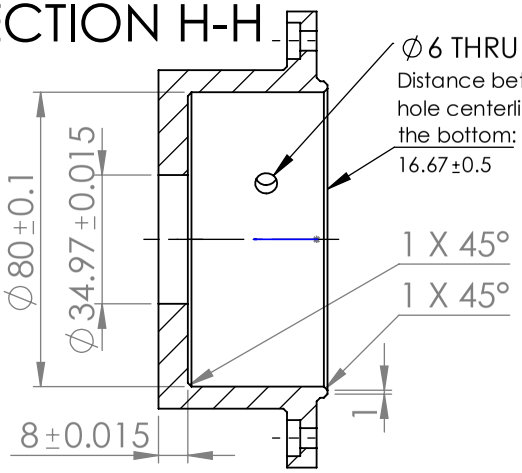

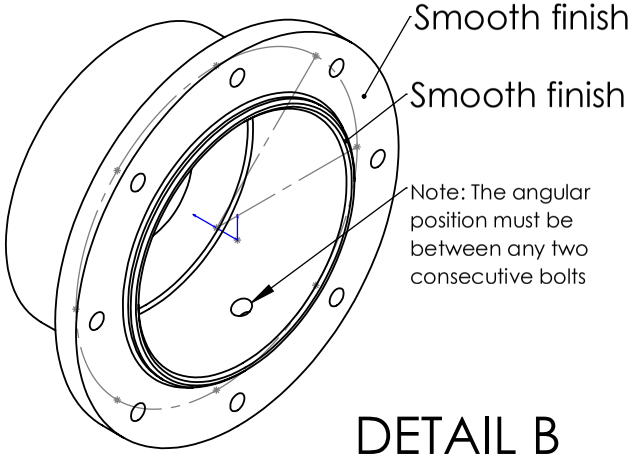

DETAIL B
SCALE 1 : 1

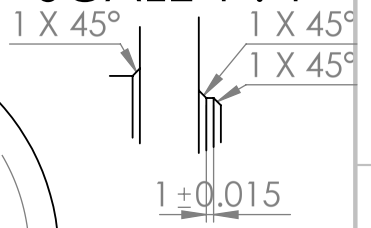

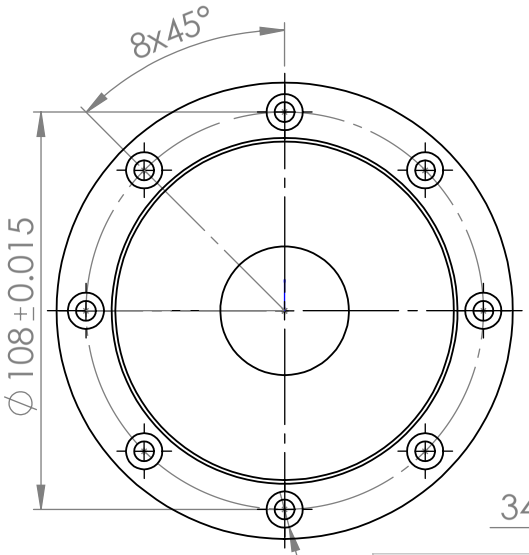

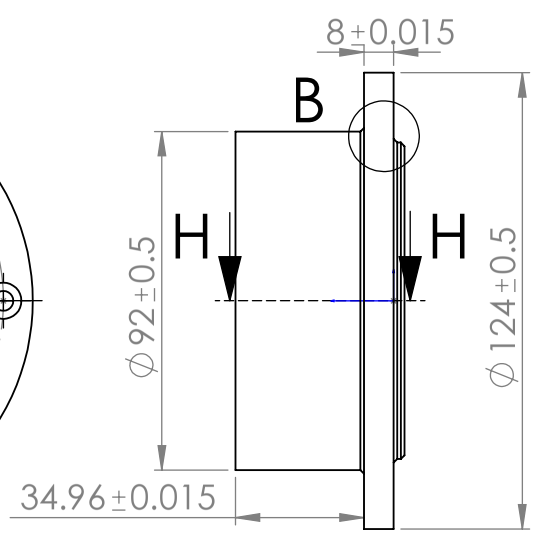

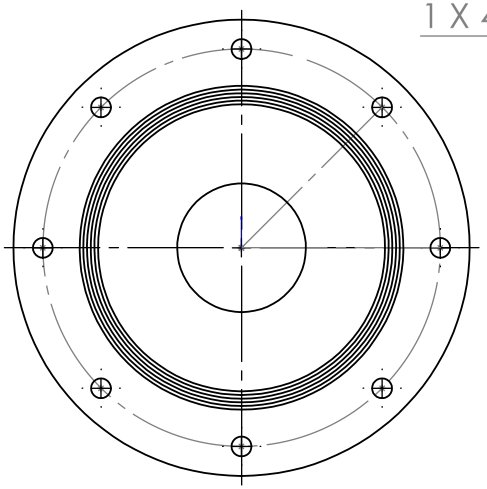

		UNLESS OTHERWISE SPECIFIED:		NAME	DATE
		DIMENSIONS ARE IN MILLIMETERS TOLERANCES: FRACTIONAL ± ANGULAR: MACH ± BEND ± TWO PLACE DECIMAL ± THREE PLACE DECIMAL ±	DRAWN		
			CHECKED		
			ENG APPR.		
			MFG APPR.		
		INTERPRET GEOMETRIC TOLERANCING PER:	Q.A.		
		MATERIAL: MILD STEEL	COMMENTS:		
NEXT ASSY	USED ON	FINISH: STANDARD ROUGH			
APPLICATION		DO NOT SCALE DRAWING			

<COMPANY NAME>

TITLE:

20_BEARING_JOURNAL_BOTTOM_SUPPORT

SIZE	DWG. NO.	REV
A		

SCALE: 1:2 | SHEET 1 OF 1

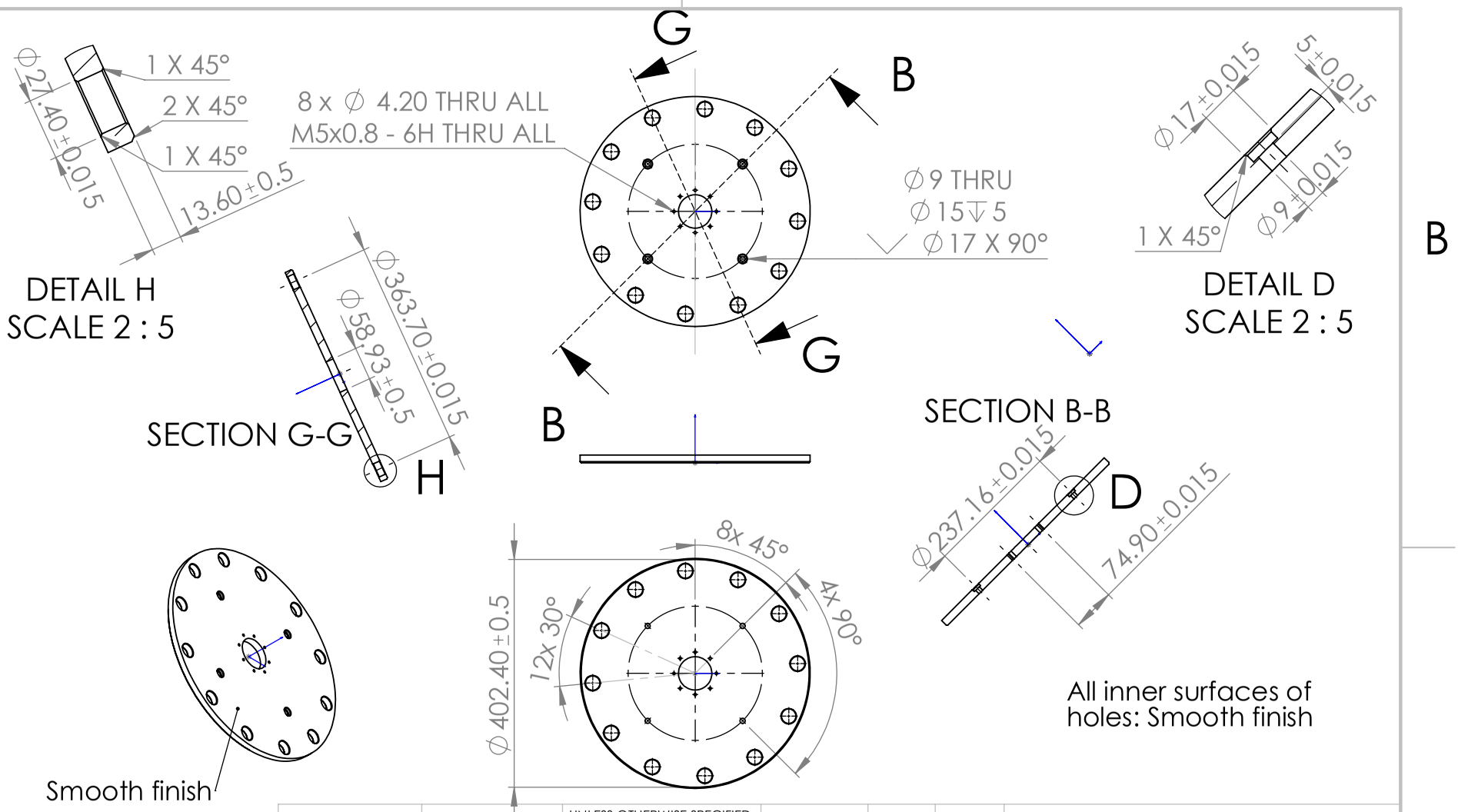

		UNLESS OTHERWISE SPECIFIED:		NAME	DATE
		DIMENSIONS ARE IN MILLIMETERS TOLERANCES: FRACTIONAL ± ANGULAR: MACH ± BEND ± TWO PLACE DECIMAL ± THREE PLACE DECIMAL ±	DRAWN		
			CHECKED		
			ENG APPR.		
			MFG APPR.		
		INTERPRET GEOMETRIC TOLERANCING PER:	Q.A.		
		MATERIAL: MILD STEEL	COMMENTS:		
NEXT ASSY	USED ON	FINISH: STANDARD ROUGH			
APPLICATION		DO NOT SCALE DRAWING			

<COMPANY NAME>

TITLE:

22_CASING_BOTTOM_PLATE

SIZE	DWG. NO.	REV
A		

SCALE: 1:10 SHEET 1 OF 1

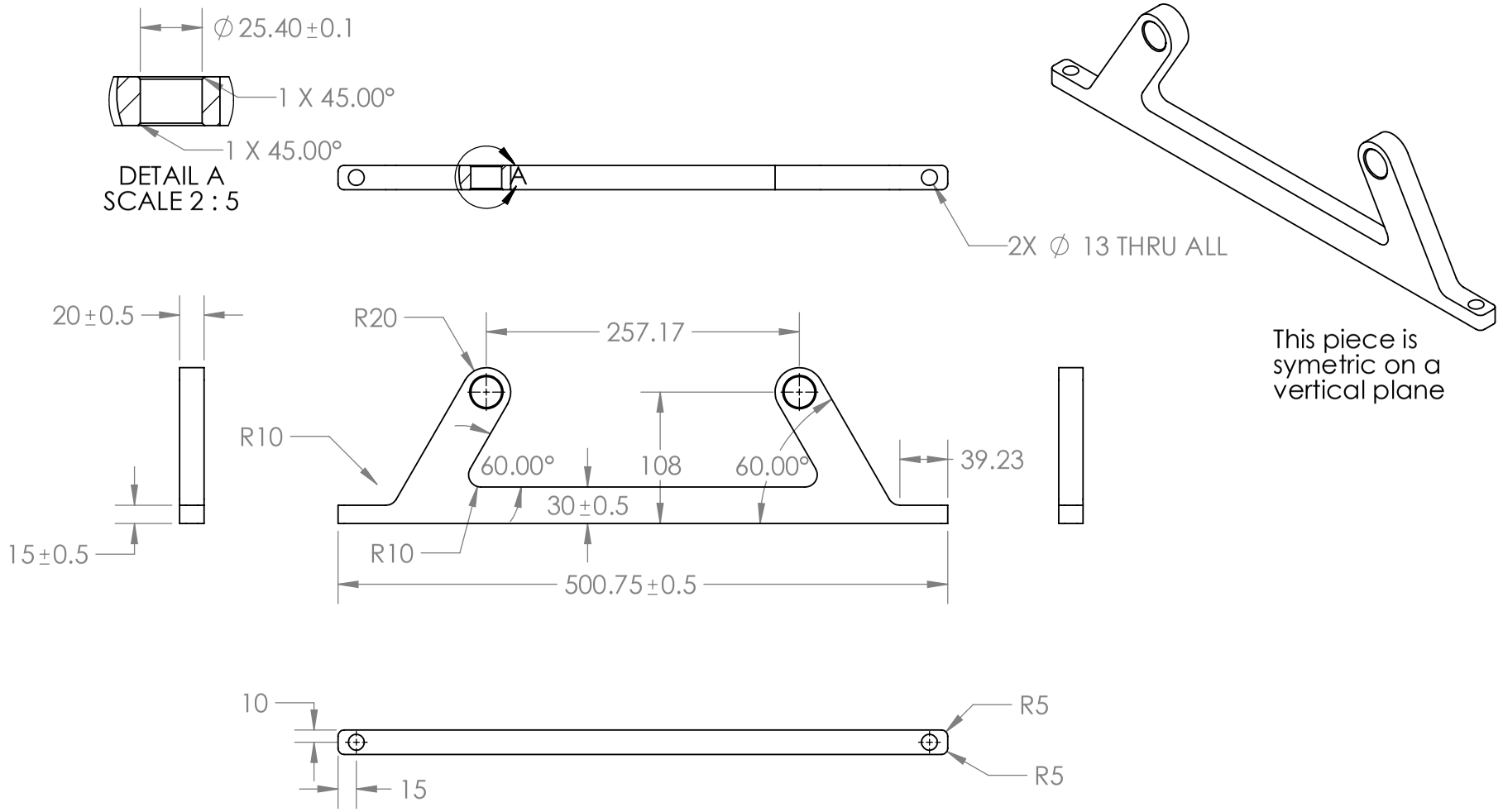

		UNLESS OTHERWISE SPECIFIED:		NAME	DATE	
		DIMENSIONS ARE IN MILLIMETERS TOLERANCES: 0.015 FRACTIONAL ± ANGULAR: MACH ± BEND ± TWO PLACE DECIMAL ± THREE PLACE DECIMAL ±	DRAWN			TITLE: 24_case_support
			CHECKED			
			ENG APPR.			
			MFG APPR.			
		INTERPRET GEOMETRIC TOLERANCING PER:	Q.A.			
		MATERIAL: MILD STEEL	COMMENTS:			SIZE A / DWG. NO. / REV
NEXT ASSY	USED ON	FINISH: STANDARD ROUGH				
APPLICATION		DO NOT SCALE DRAWING				SCALE: 1:5 / WEIGHT: / SHEET 1 OF 1

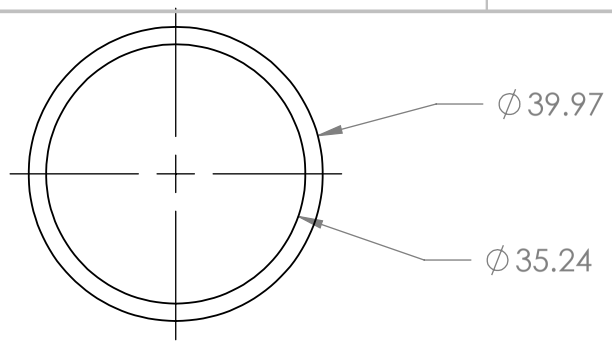

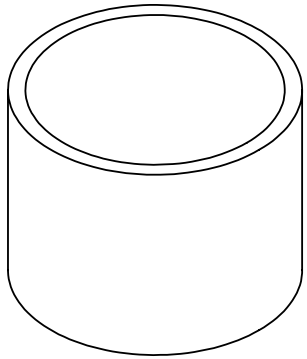

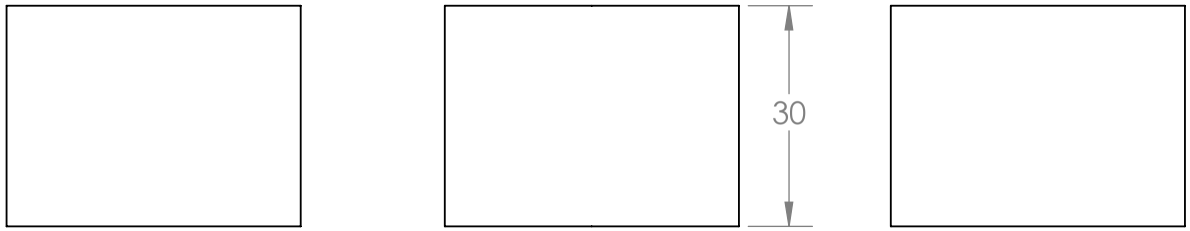

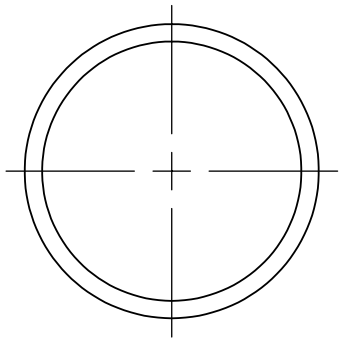

		UNLESS OTHERWISE SPECIFIED:		NAME	DATE
		DIMENSIONS ARE IN INCHES TOLERANCES: 0.015 FRACTIONAL ± ANGULAR: MACH ± BEND ± TWO PLACE DECIMAL ± THREE PLACE DECIMAL ±	DRAWN		
			CHECKED		
			ENG APPR.		
			MFG APPR.		
		INTERPRET GEOMETRIC TOLERANCING PER:	Q.A.		
		MATERIAL: IMPREGNED BRONZE	COMMENTS:		
NEXT ASSY	USED ON	FINISH: SMOOTH			
APPLICATION		DO NOT SCALE DRAWING			

TITLE:

11_BEARING_SLEEVE

SIZE	DWG. NO.	REV
A		

SCALE: 1:1	WEIGHT:	SHEET 1 OF 1

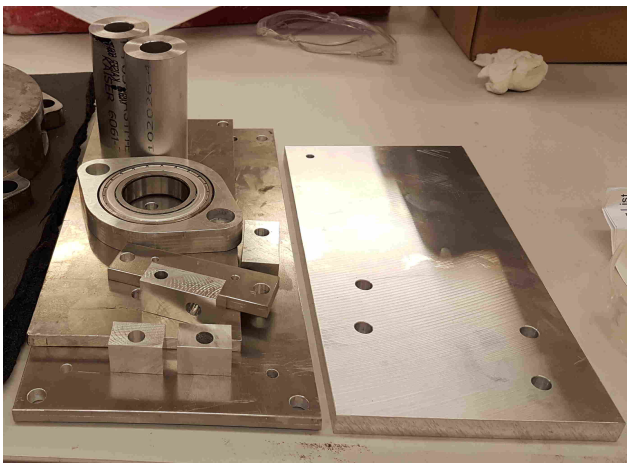

(a) Expander driven side and oil pump assembly parts

(b) Support tubes and motor feet bridge

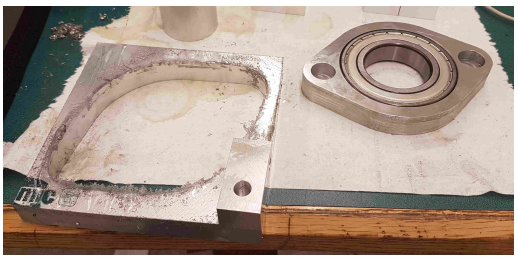

(c) Mount bearing

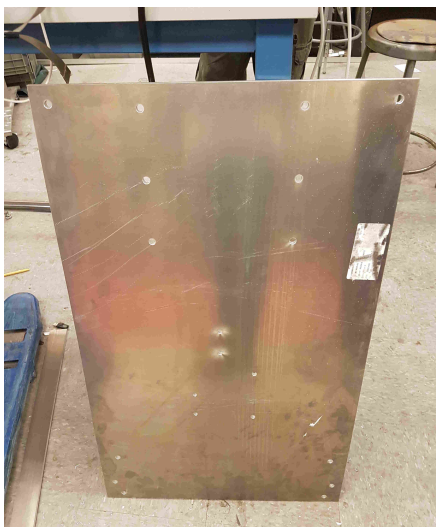

(d) Assembly's base plate

(e) Expander foot

Figure 6.3: Parts machined at MIT